# Thèse en cotutelle

Entre

**L'Université Djillali Liabes de Sidi Bel-Abbes, Algérie**

Et

**L'INSA de Rennes, France**

En vue d'obtenir le titre de

**Docteur en sciences**
*Spécialité : Traitement du signal et de l'image*

**Docteur de l'INSA**
*Spécialité : Traitement du signal et de l'image*
*sous le sceau de l'Université européenne de Bretagne*
**ECOLE DOCTORALE : *MATISSE***

Présentée par

**Miloud CHIKR ELMEZOUAR**

---

# Fusion d'images en télédétection Satellitaire

# (Image fusion in satellite remote sensing)

---

Thèse soutenue le 10 décembre 2012, devant le jury compose de :

| | | |
|---|---|---|
| **Mimoun MALKI** | | |
| Professeur, Université Djillali Liabes, Sidi-Bel-Abbes, | Algérie | Président |
| **Abdelmalik TALEB-AHMED** | | |
| Professeur, Université de Valenciennes, | France | Examinateur / Rapporteur* |
| **Abdelhafid BESSAID** | | |
| Professeur, Université Abou Bekr Belkaid, Tlemcen, | Algérie | Examinateur / Rapporteur* |
| **Kidiyo KPALMA** | | |
| Maître de conférences (HDR), INSA de Rennes, | France | Examinateur |
| **Nasreddine TALEB** | | |
| Professeur, Université Djillali Liabes, Sidi-Bel-Abbes, | Algérie | Directeur de thèse |
| **Joseph RONSIN** | | |
| Professeur des universités, INSA de Rennes, | France | Directeur de thèse |

* selon les règles et dispositifs de l'établissement partenaire

To my wife Khadidja,

To my daughters: Israa, Kiba and Ikram,

To the memory of my mother,

To my father,

To all the members of my family.

Miloud.

# Acknowledgments

I want to express my gratitude to the review committee of the thesis
Mimoun MALKI, Professor at Djillali Liabes University of Sidi-Bel-Abbes (Algeria),
Abdelmalik TALEB-AHMED, Professor at University of Valenciennes (France),
Abdelhafid BESSAID, Professor at Abou Bekr Belkaid Université of Tlemcen (Algeria),
for their time and for their constructive remarks.

I am deeply grateful to Kidiyo KPALMA, Maître de conférences (HDR) at INSA of Rennes (France) not only because he accepted to be in the review committee but also because he devoted his time to me whenever I needed him. His qualities both as a person and as a researcher will always serve to me as an example of the perfect supervisor.

Above all, I am deeply indebted to my supervisors
Nasreddine Taleb, Professor at Djillali Liabes University of Sidi-Bel-Abbes (Algeria)
Joseph Ronsin, Professor at INSA of Rennes (France)
for their guidance which made this thesis a reality. I really appreciate their patience, scientific and human encouragements. I have learned from them lots of things ranging from doing research to writing a scientific paper.

I would like to thank all people who, in one way or another, have supported me in my research and during my staying in Rennes, France.

Many thanks to all my colleagues in Djillali Liabes University of sidi Bel-Abbes for creating such a supportive and helpful environment.

Special thanks to all my colleagues in MainSy Automation, for their patience, help, constant support and encouragement. Their happiness and warm friendship have given me a lot of positive energy.

I would like to thank all my friends, because even though I cannot write a word for everyone, I remember all of them.

I am mostly grateful to all my family for helping me to overcome the little and great problems and for their love during all these years.

# List of contents

# Introduction

Space systems play an important role in the field of earth observation and knowledge of our environment. On these systems, are carried different types of sensors: passive and active (radars). Passive sensors can only detect the energy provided by the environment. In contrast, active sensors transmit energy, and then collect the reflected energy. In this thesis, our interest will focus on passive sensors covering the visible and infrared bands. The images produced by these sensors allow the distinction of the geometric structures according to the spatial resolution. When the sensor is able to integrate the incident radiation energy over a wide range of wavelength band, it offers little information on the spectral level, but at the same time, it offers a high spatial resolution. In general, such images are called panchromatic (Pan). In contrast, some sensors capture energy over a set of much narrower bands of spectra to produce multispectral images (MS). Then their spectral resolution is much higher, but at the cost of a low spatial resolution. Note that the terms of resolution 'high' or 'low' are relative terms to describe the different resolutions between images acquired by a single observation system for Pan and MS images.

The advantage of using MS images with a high spatial resolution has already been demonstrated in many remote sensing applications. The color information helps in the distinction of different regions of the image compared to the grayscale Pan image. Therefore, if we can use these spectral contents while taking advantage of a better spatial resolution, the identification of objects in a scene will be enriched and more accurate.

The question is why manufacturers have not directly built sensors able to provide images with high spatial and high spectral resolutions?

In fact, these notions are contradictory from a technical point of view when a given technology is given; when the acquisition spectrum of a sensor is large the incident light flux on a pixel of the image is great. The pixel size is then lower and therefore the image has better spatial resolution. At the opposite, a narrow acquisition spectrum, including a restricted incident light flux on a pixel, produces a low spatial resolution.

To overcome this problem, it is possible to combine these data, Pan and MS, and produce MS imagery with a higher spatial resolution by using suitable algorithms. This concept is known as multispectral or multisensor merging, fusion or pansharpening [1]. Pansharpening can be defined as a pixel level fusion technique used to synthesise the MS images to a higher resolution using spatial information from the Pan image.

Pansharpening techniques increase the spatial resolution while simultaneously preserving the spectral information in the final produced MS image, giving the best of the two worlds: high spectral resolution and high spatial resolution. Wald in [2] defines image fusion as: "a formal framework in which are expressed means and tools for the alliance of data originating from different sources. It aims at obtaining information of greater quality; the exact definition of 'greater quality' will depend upon the application".

This thesis aims at presenting the work carried out for fusing MS and Pan images and for quality assessment of the produced pansharpened images. Our contributions include:

1). Two pansharpening methods based on the IHS transform.
2). A Non Sub-sampled Contourlet Transform (NSCT)-based pansharpening method.
3). A protocol for evaluating and ranking pansharpening method.
4). A vegetation index derived from Pan images for high resolution satellites.
5). A method for vegetation extraction from the Ikonos satellite

To present the context of this work and our contributions, this thesis is organized into the following five chapters.

Chapter 1 introduces remote sensing imagery, satellite characteristics and vegetation indices. Remote sensing images are presented based on their spectral and spatial characteristics. Hence, Pan and MS images are presented in the optical images section and SAR and Lidar are presented as the rest of the spectral classification of optical images. In the spatial classification, discussion is about low, medium and high resolution. The chapter also presents satellite characteristics, mainly Ikonos, QuickBird and Worldview. The vegetation indices extracted from multispectral remote sensing images are also explained. These indices are conventionally in diverse applications in remote sensing of the environment.

Chapter 2 presents a critical state of the art about pansharpening methods and particularly the latest ones. The qualitative and quantitative evaluation of their performance has opened up many

opportunities for the development of remote sensing applications. Image fusion methods have been classified in several ways. Although it is not possible to find a universal classification, we choose that of [3] organized into five categories: component substitution, relative spectral contribution, high frequency injection, methods based on statistics of the image and finally multiresolution family. This Chapter introduces also some pre-processing techniques needed in pansharpening, such as image registration, interpolation and histogram matching.

Chapter 3 presents a critical review of quality assessment indices found in the literature for evaluation of pansharpened products. This review consists to understand the limitations of the quality assessment indices in order to develop a protocol for quality assessment for fused images. For assessing the quality of a pansharpened image, the fused images must be compared to a reference, which does not exist in the case of the fusion of the MS image and the high spatial resolution Pan image. The assumption of extrapolation is to apply the fusion process at a scale where the reference is available and to suggest that the quality at this low resolution is close to or even better than could have been drawn to a scale of higher spatial resolutions. More concretely, suppose that the spatial resolution of the original Pan and MS images are hi and lo, respectively. The Pan and MS images will be downsampled to their lower resolutions lo and vl, respectively. Then, Pan at resolution lo and MS at resolution vl are fused to obtain a fused MS at resolution lo that can be then compared with the original MS image. The quality assessed at resolution lo is assumed to be close to the quality at resolution hi.

Chapter 4 presents the main contributions of the author. Two developed methods based on the IHS transform are discussed. Pansharpening and color enhancement cases are studied. A detailed section is dedicated to the presentation of the proposed vegetation index, called High Resolution NDVI (HRNDVI). Moreover, the developed NSCT-based pansharpening method is presented. Finally, extraction of vegetation from Ikonos images, using the proposed HRNDVI index is presented to demonstrate the efficiency of this index. All the algorithms are illustrated with high resolution images and quantitative analyses are given.

Finally, Chapter 5 is dedicated to the proposed protocol for the evaluation of the pansharpening techniques. Most of the indices discussed in chapter 3 are used in this protocol. The problem of the contradiction of visual and quantitative evaluations of some pansharpened images was observed when conducting some experiments on pansharpening algorithms presented in the previous chapter. It can be found that the quantitative quality is high but visually not. The proposed protocol allows having two separate indications, the first one for spectral quality and the second one for the spatial quality. Moreover, these two measures can be combined in one global measure with the possibility to promote one measure relatively to the second one. This protocol leads to a better tuning between visual and quantitative evaluations. Appendix A presents the interpolation impact on the quality of pansharpened images.

# Part A

## *State of the art in*

## *Remote sensing,*

## *Pansharpening and*

## *Quality assessment*

# 1

# Remote Sensing

## 1.1 Introduction

Remote sensing is defined as group of techniques for collecting useful information about objects, area or phenomenon through the measurements and analysis of data collected by devices that are not in physical contact with the objects, area, or phenomenon under investigation. In the context of this thesis, remote sensing is defined as the science and technology of collecting information about the earth surfaces, sea surfaces, clouds, and the atmosphere of earth, etc., by aircraft and satellites without being in contact with the earth. This is relying on sensing and recording reflected signals of some sort, for example optical, acoustical, or microwave, then processing and applying information. This concept is illustrated in figure 1.1. Airplanes and artificial satellites collect large scale, but precise, data regarding the physical conditions at the surface as well as the atmosphere of earth. Later, scientists around the world interpret these data to extract information useful for specific applications discussed in the succeeding sections. While remote-sensing data can consist of discrete, point measurements or a profile along a flight path, we are most interested here in measurements over a two-dimensional spatial grid, i.e., images. Remote-sensing systems, particularly those deployed on satellites, provide a repetitive and consistent view of the earth that is invaluable to monitoring short-term and long-term changes and the impact of human activities [1].

Remote sensing was founded after photography invention in the $18^{th}$ century. Aerial photography was first practiced by the French photographer and balloonist Gaspard-Félix Tournachon, known as "Nadar", in 1858 over Paris, France. It was used for military purposes in the First World War. Since the launch of Sputnik I in 1957, several satellites have been sent into space on missions to collect data about the earth.

The remote sensing satellites further divide into two broad categories of meteorological satellites and the earth observation satellites. The launch of the first meteorological satellite (TIROS-1) was in 1960, moreover with the 4 spectral bands of the first Earth-observing satellite (Landsat-1) launched in late July 1972 began the modern era of land remote sensing from space. The multispectral bands led to an improved understanding of crops, minerals, soils, urban growth, and many other Earth features and processes. A meteorological satellite can be defined as an Earth observation satellite used for the specific task of monitoring wind, cloud formations and other variables that permit predicting weather.

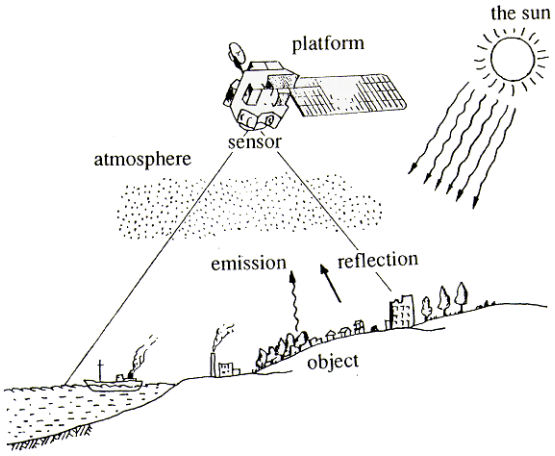


Figure 1.1 Data collection by remote sensing[1]

There are two main modes of operation of remote sensing: passive remote sensing and active remote sensing. Passive sensors depend on an external source of energy, usually the sun. They capture energy emitted by sun and reflected by the object or surrounding area being observed, in visible, near infrared and thermal infrared bands. This energy is relative to physical and chemical properties of the objects under observation. On the other hand, active sensors have their own source of energy. Active remote sensing satellites emit energy, in order to scan objects and areas, and then recapture it as it bounces back from objects on Earth's surface. RADAR and LiDAR are examples of active remote sensing. Active sensors are more controllable because they do not depend upon varying illumination conditions.

In this chapter, the remote sensing imagery with a spectral and spatial classification is presented. For the spectral classification case details on optical, SAR and Lidar images are given. Remote sensing images are categorized in low, medium and high spatial resolution for the spatial classification case. In section 1.3, the satellites characteristics, namely Ikonos, QuickBird and Worldview are discussed. As the vegetation extraction represents a widely used application in remote sensing, some vegetation indices are introduced in section 1.4.

[1] Source: http://stlab.iis.u-tokyo.ac.jp/~wataru/lecture/rsgis/rsnote/cp1/1-1-1.gif

## 1.2 The remote sensing imagery

The recent progresses in electronics field have enabled remote sensing system to reach images with ground resolutions finer than ever before. The acquired images from the remote sensing depend on the sensor spatial resolution, the imaged area on the surface, the revisit time and the wavelength bands employed in image acquisition. In the following sections only spatial and spectral resolutions are detailed, in contrast of temporal resolution specified by the revisiting frequency of a satellite sensor for a specific location.

### 1.2.1 Spectral classification:

In terms of spectral regions used in data acquisition, three types of images are produced by a remote sensing system: optical images, Synthetic Aperture Radar (SAR) images and Light Detection And Ranging (LiDAR) images.

#### 1.2.1.1 Optical images:

Optical sensors capture optical images of the earth's surface in visible, near infrared and short-wave infrared bands. Wavelengths of bands in a optical remote sensing system ranges from 0.30mm to 15.0.Radiometric, spectral, textural, geometric and contextual information, contained in an optical image, usually serve in image interpretation. Depending on the number of spectral bands used, optical images are classified into four broad categories, Panchromatic (Pan), Multi-Spectral (MS), Super-Spectral (SS) and Hyper-Spectral (HS).

##### 1.2.1.1.1 Panchromatic image

A panchromatic sensor consists of a single band detector sensitive to radiation within a wide spectral range covering visible as well as IR wavelengths. If the wavelength range coincides with the visible range, then the imagery will appear as a black and white photograph taken from space. The physical quantity being measured is the apparent brightness of the targets. The color of the targets is not available. It is usually displayed as a grey scale image as in figure 1.2 that shows Pan image of Yokohama, Japan acquired October 5, 2007 by WorldView-1. Though it is also different in a way that unlike black and white photograph, Pan sensors of some satellites also cover the infrared wavelengths and in some satellites, these do not cover the blue wavelengths. The Pan images always have greater resolutions than the MS images from the same satellite. It is due to the much more energy per unit area gathered by a Pan sensor due to its wider bandwidth. Refer to figure 1.3 that shows the frequency response of the Pan sensor of WorldView-1. Examples of panchromatic imaging system are Ikonos Pan, QuickBird Pan and WorldView Pan.

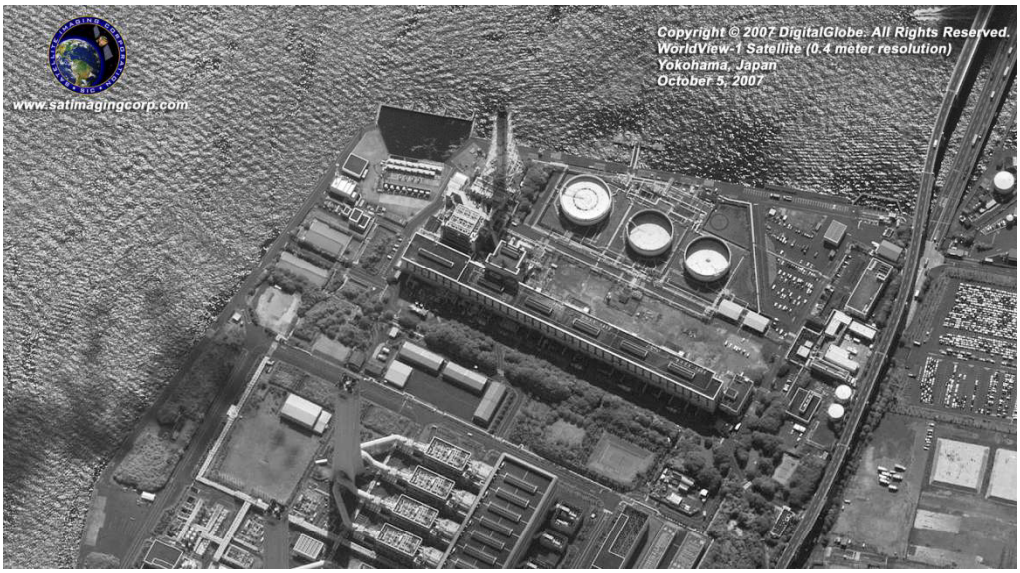


Figure 1.2 A WorldView-1 Panchromatic image of Yokohama, Japan acquired October 5, 2007 [2]

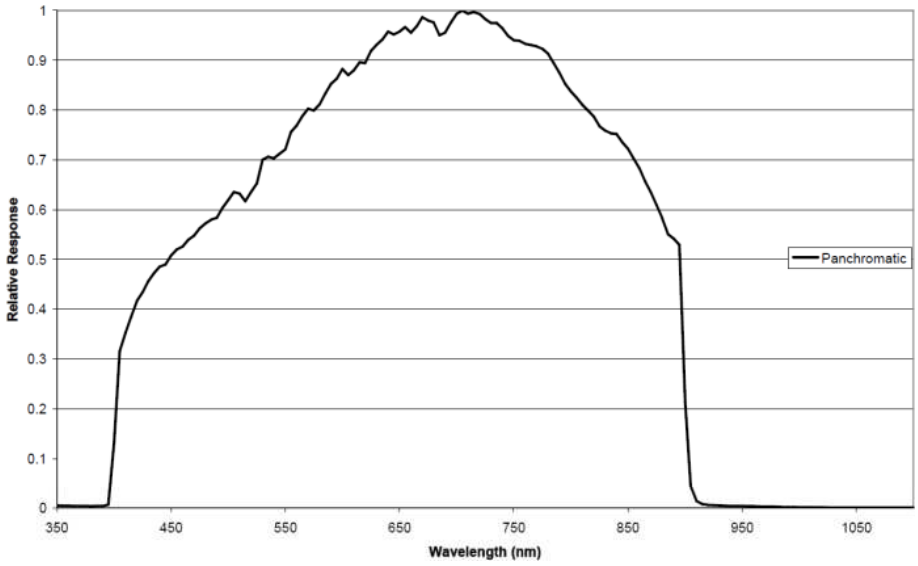


Figure 1.3 WorldView-1 imager relative spectral radiance response [4]

#### 1.2.1.1.2 Multi-spectral image

The sensor of a multi-spectral imaging system is obtained from a set of multi-band sensors (less than 10 bands). Compared to panchromatic imaging system, the recorded radiation of a multispectral imaging system is within a narrow range of wavelength for each band. Both brightness and spectral (color) information of the targets being observed are available on the resulting image. Whatever, multispectral images have a low resolution they can cover the visible as well as infrared range of wavelengths. In figure 1.4 the responses of the Pan as well as the 8 multispectral sensors of WorldView-2 satellite are shown to illustrate the used range of the electromagnetic spectrum from the visible to the infrared part. The three

[2] Source : http://www.satimagingcorp.com/galleryimages/worldview-1-satellite-image-yokohama-japan.jpg

visual primary color bands (red, green, blue) of MS image may be combined to produce a "true color" image. However, the display color assignment for any band of a MS image can be done in an entirely arbitrary manner. In this case, the color of a target in the displayed image differs from its actual color. The resulting product is known as a false "color image". Figure 1.5 illustrates a scene from the Hajj pilgrimage area in Mecca at Saudi Arabia acquired November 2, 2011, with a true color image having 0.5 m resolution captured by WorldView-2.

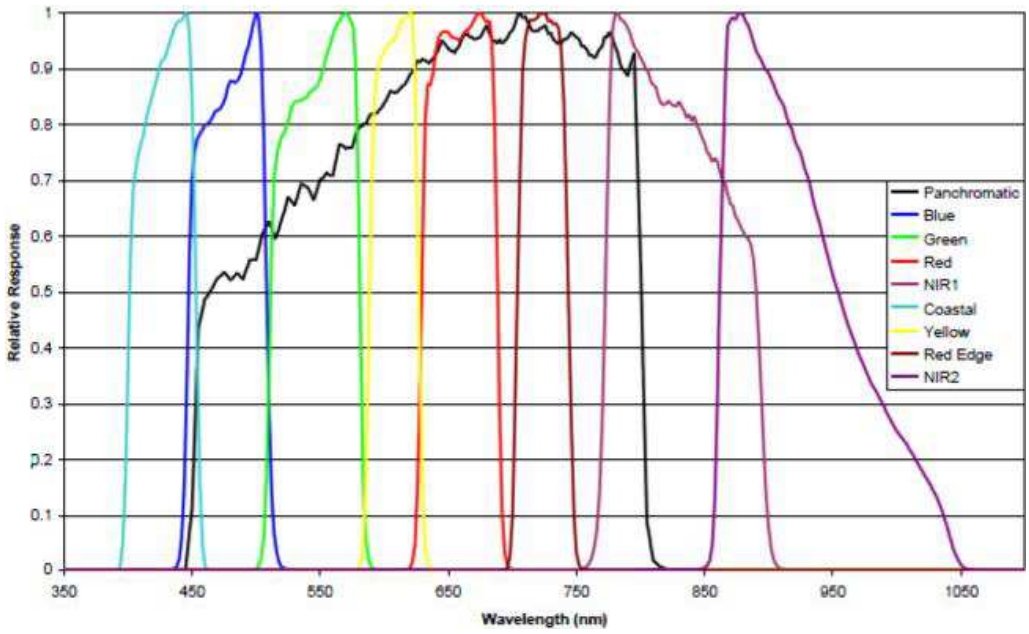


Figure 1.4 Spectral Response of the WorldView-2 panchromatic and multispectral imager [4]

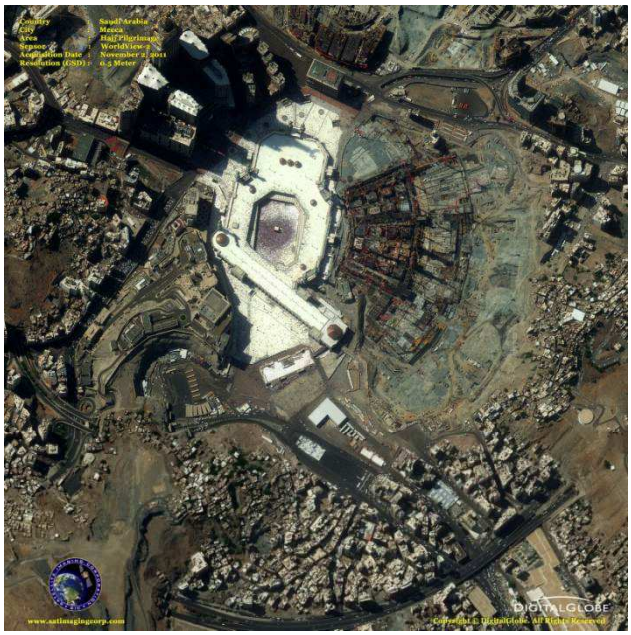

Figure 1.5 half-meter satellite photo of the Hajj pilgrimage captured by WorldView-2[3]

[3] http://www.satimagingcorp.com/galleryimages/worldview-2-mecca-hajj.jpg (visited May 2012)

This is a pansharpening result of the original multispectral bands (2 m resolution) with the corresponding panchromatic image having 0.5 m resolution. Pansharpening is a process of fusing Pan and MS images to create a single high spectral and spatial resolution image.

In case of satellite that does not have the three true color bands: Red, Green and Blue, it is recommended to use a false color representation. SPOT-5 is an example, where blue band is not acquired. This missing band can be replaced by NIR band and then displayed as red channel. The red and green bands are displayed as green and blue channels, respectively, generating a false color image representation (see figure 1.6 left picture). Moreover, by combining of multispetral bands, it is possible to get a natural colour appearance of the image, as it is shown at the right of figure 1.6.

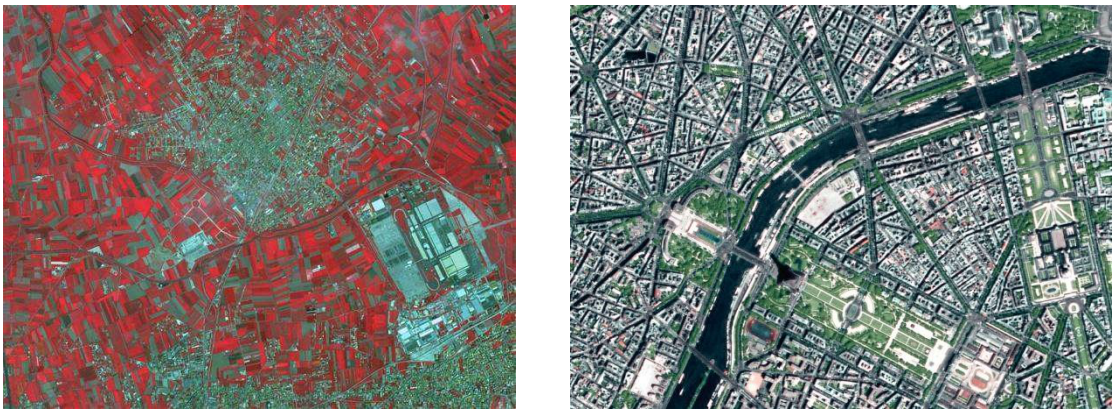

Figure 1.6 SPOT 5: left image: Naples[4] at 5 m resolution and right image: Paris[5] at 2.5 m resolution

**1.2.1.1.3 Super-spectral and Hyper-spectral images**

An imaging system is considered super-spectral if it acquires more than ten spectral bands. It will be hypersepctral if the number of the captured spectral bands is more than one hundred. Bandwidths are narrower when the number of spectral bands increases. Thus, sensors will be able to capture the finer spectral characteristics of the features of the targets. These types of systems will improve understanding of global dynamics and processes occurring on the land, in the oceans, and in the lower atmosphere. It find a potential applications in such fields as precision agriculture (e.g. monitoring the types, health, moisture level and maturity of crops), coastal management (e.g. monitoring of phytoplankton, pollution, bathymetry changes) etc. Examples of superspectral optical remote sensing system are MODIS (36 spectral bands) and MERIS (15 programmable spectral bands), and of a hypespectral is Hyperion (242 spectral bands).

Example of MODIS image is illustrated in left of figure 1.7. This natural color image acquired on April 2012 and issued from the combination of bands 1, 4 and 3, shows a dust storm over Egypt. The middle and right images of figure 1.7, captured on October 23, 2007 using Hyperion spectrometer, show wildfire

[4] http://spot5.cnes.fr/images/naples/naples_no_01.html (visited May 2012)

[5] http://spot5.cnes.fr/images/paris/paris_so_01.htm (visited May 2012)

areas in Southern California. The middle data visualization represents the scene, as the human eye would see it. Using three of shortwave infrared bands gives a better view of the burning fire, as illustrated in the right side of figure 1.7.

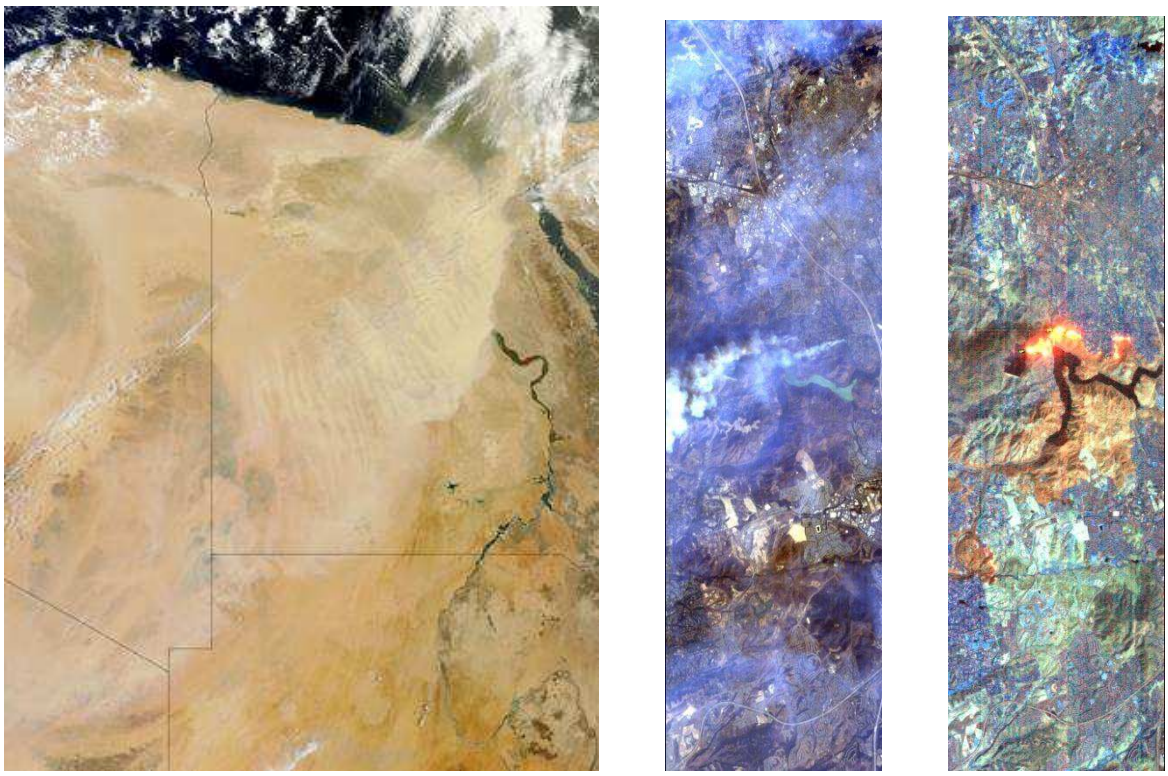

Figure 1.7 Left: MODIS image [6], middle: Hyperion image 1[7] and right Hyperion image 2[8]

### 1.2.1.2 SAR images:

Radio Detection and Ranging (Radar) is an object-detection system developed in the 1950s that uses radio waves to determine the range, altitude, direction, or speed of objects. Synthetic Aperture Radar (SAR) is a technique for obtaining high-resolution images of the earth's surface. In SAR imaging, microwave pulses are transmitted by an antenna towards the earth surface. The SAR system detects the reflected microwave energy and forms an image using the time delay of the backscattered signals. Over the area of the surface being observed, these images represent the backscattered microwave energy, the characteristics of which depend on the properties of the surface, such as its slope, roughness, humidity, textural inhomogeneities and dielectric constant. Figure 1.8 shows a high-resolution airborne SAR image. High resolutions images are required in such applications as environmental monitoring, earth-resource mapping, and military systems.

[6] http://modis.gsfc.nasa.gov/gallery/individual.php?db_date=2012-04-22 (visited April 2012)

[7] http://www.nasa.gov/images/content/194419main_eo-1_RGB.jpg (visited April 2012)

[8] http://www.nasa.gov/images/content/194420main_eo-1_SWIR.jpg (visited April 2012)

Figure 1.8 miniSAR 4-inch resolution $K_u$ Band image, Kirtland Air Force Base Gated Entrance[9]

SAR is capable of operating under inclement weather conditions, day or night. For this reason and due to the unique responses of terrain and cultural targets to radar frequencies, SAR images help to differentiate the cover types that are otherwise indistinguishable in the optical images due to their similar spectral characteristics. For example, the SAR data may be used in areas of no information on the optical data, as areas covered by clouds and their shadows. [5] and [6] use the SAR imagery in combination with very high resolution optical images for natural disaster assessment, [7] describes the use of SAR images for monitoring and detection ships and oil spills, [8] classifies SAR images for military application like the detection of manmade objects (metal objects). However, the SAR images usually suffer from severe levels of a non-Gaussian multiplicative speckle noise. Table 1.1 shows the microwave bands and their corresponding range of frequencies.

| | | | | | |
|---|---|---|---|---|---|
| L band | 1 to 2 GHz | S band | 2 to 4 GHz | C band | 4 to 8 GHz |
| X band | 8 to 12 GHz | $K_u$ band | 12 to 18 GHz | K band | 18 to 26.5 GHz |
| $K_a$ band | 26.5 to 40 GHz | Q band | 33 to 50 GHz | U band | 40 to 60 GHz |
| V band | 50 to 75 GHz | E band | 60 to 90 GHz | W band | 75 to 110 GHz |
| F band | 90 to 140 GHz | D band | 110 to 170 GHz | | |

Table 1.1: Microwave bands with corresponding range frequency[10]

Some satellites have multiple operating frequencies, providing observations of the same scene at different operating bands. This provides better discrimination among different vegetation types or the same vegetation type in different states of health or growth.

[9] http://www.sandia.gov/RADAR/images/SAND2005-3706P-miniSAR-flight-SAR-images.pdf (visited April 2012)

[10] http://en.wikipedia.org/wiki/Microwave

SAR applications increase almost daily as new technologies and innovative ideas are developed. SAR has become a valuable remote sensing tool for both military and civilian users. Recognition, surveillance, targeting information, intelligence gathering, battlefield reconnaissance and weapons guidance are some military applications. Climate, environment and land use monitoring, change detection, agricultural classification and assessment, topographic mapping, geology and mining, navigation and guidance, sea ice monitoring, oil spills detection and oceanography are some civilian applications. The following is a list of some of the spaceborne SAR remote sensing platforms and sensors:

- Tropical rainfall measuring mission (TRMM),
- European Remote Sensing Satellite 1 and 2 (ERS-1/2),
- Japanese Earth Resources Satellite-1(JERS-1),
- Mediterranean basin observation (COSMO-SkyMed),
- RADARSAT, very similar to ERS,
- Solid Earth Interferometric Spaceborne (SEISM),
- advanced land observing satellite (ALOS),
- Shuttleborne Imaging Radar. SIR-C/X-SAR,
- Shuttle Radar Topography Mission SRTM.

ERS-2 and ALOS satellites also provide optical images besides SAR images.

SAR provides the structural information in 2D. A more recent technology called Lidar provides the same in 3D.

### 1.2.1.3 Light detection and ranging (Lidar) images:

Recently, there has been a rapprochement between the optical and radar fields, manifested not only in the spectral point of view but especially in design and operation mode of the systems. These systems, referred to Lidar, grow due to the progress of lasers, which exploit the spatial, spectral and temporal properties. Lidar, which stands for Light detection and ranging (sometimes referred to as Ladar or Laser detection and Ranging), has received wide acceptance in airborne surveying as a leading tool for obtaining high-quality surface data in an unprecedentedly short turnaround time. Lidar is laser scanning technology that uses a laser light emitter and sensors to measure the distance between the aircraft and the ground, including objects such as buildings and vegetation. Lidar systems nowadays do range measurement with an increasing number of points per surface, count multiple returns per single shot, deliver reflectance values of the illuminated surface and capture the height of both the terrain and objects such as buildings, in amazing resolution details. Airborne Lidar is now the most widely used method of rapid and accurate terrain mapping.

As SAR, the Lidar emits a laser light onto a target at the ground and receives back a fraction of the radiation reflected from the target. The received signal carries the information of time taken in the round trip, the intensity, and the phase of the echo. The frequency of the laser light used in Lidar is usually in the ultra-violet, visible or near infrared range [9]. Lidar system can also detect more than one echoes of the same pulse so that it can view through water, canopies and trees onto the ground to map surface terrain and to estimate the depth of the water body or plantation.

It is an ideal tool when very high accuracy height measurements are required for large areas and it is very cost effective. Example of this high accuracy is given by figure 1.9, which shows an image obtained using Lidar technology, acquired in October, 2001 over the World Trade Center.

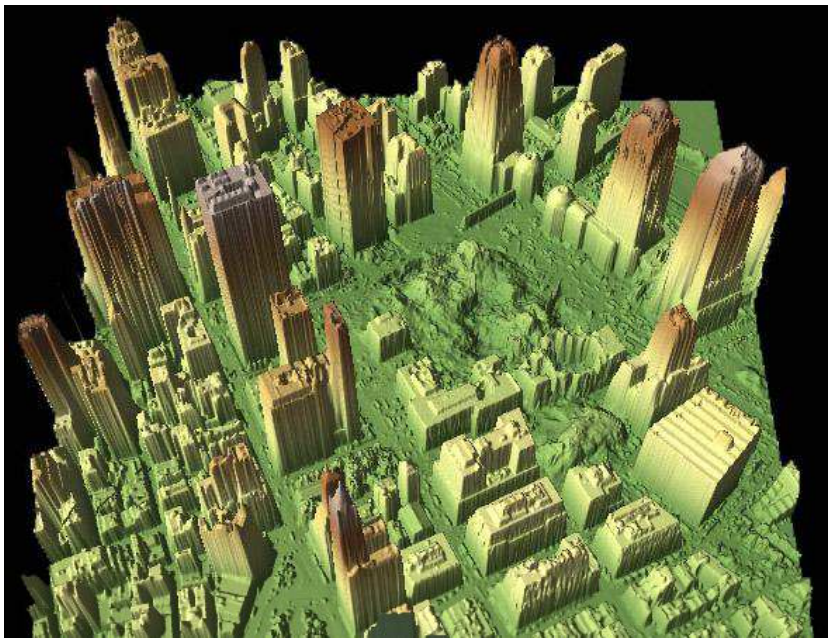

Figure 1.9 Lidar data of the World Trade Center, acquired in October, 2001[11]

### 1.2.2 Spatial classification:

In the literature, it is said that "The spatial resolution (also known as ground resolution) is the ground area imaged for the instantaneous field of view (IFOV) of the sensing device. Spatial resolution may also be described as the ground surface area that forms one pixel in the satellite image". In terms of the spatial resolution, the satellite imaging systems can be classified into: low resolution systems (approx. 1 km or more), medium resolution systems (approx. 100 m to 1 km), high resolution systems (approx. 5 m to 100 m) and very high resolution systems (approx. 5 m or less). The spatial resolution of the panchromatic Ikonos sensor, for example, is 1 m. The ground area represented by pixels at surface directly below the satellite, called the nadir point, has a larger scale than those pixels which are off-nadir, while the IFOV for all pixels of a scanner stays constant.

[11] http://www.noaanews.noaa.gov/stories/s798b.htm

To show the importance of the details obtained in high resolution, for example let us compare a simulated set of images corresponding to different resolutions. The image at left of figure 1.10 is an area extracted from GeoEye-1 image with 0.5 m resolution obtained on August 3, 2011 and representing London's 2012 Olympic Stadium, United Kingdom. The rest of the images are simulated images of 1m, 2m and 4m spatial resolution. Visually, it is clear that very high spatial resolution is more accurate and pleasant.

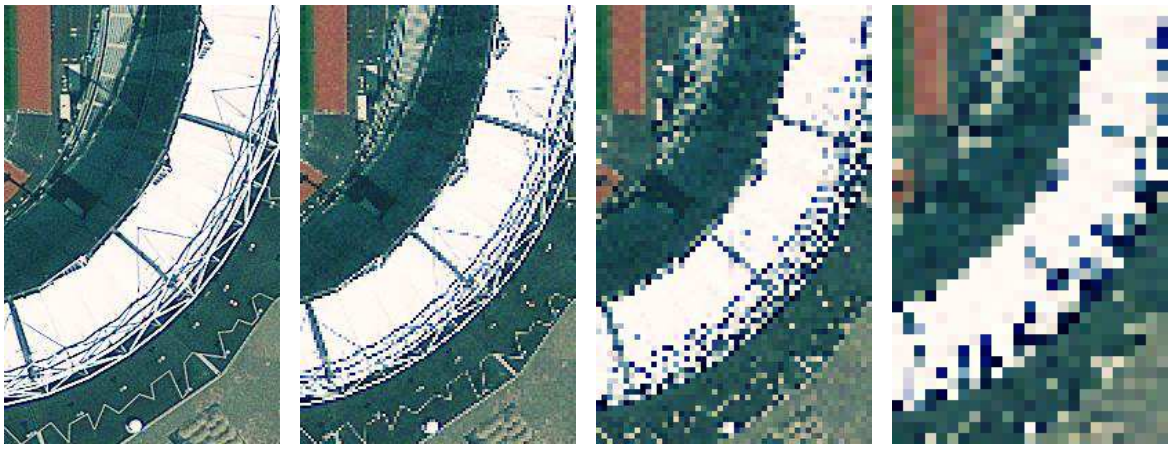

Figure 1.10 A scene with different spatial resolution: from left to right 0.5m, 1m, 2m and 4m.[12]

### 1.2.2.1 Low resolution

Low-resolution satellites are characterized by spatial resolution at about 1 km giving regular daily coverage. These data are obtained only in multispectral mode including visible and infrared part of the optical spectrum. These data are useful for large-area, global and continental mapping, regular coverage needs, including sea surface temperature monitoring, atmosphere and ocean's monitoring, vegetation conditions monitoring, regional vegetation vigour and drought studies, large disasters monitoring, snow cover and glaciers monitoring. Low resolution satellite examples are:

- Meteosat MSG: capturing 7 bands of 40 km resolution using GERB sensor,
- SPOT 5: capturing 4 bands of 1km resolution using VEGETATION 2sensor, and
- OrbView-2: capturing 8 bands of 1.13km resolution using SeaWiFS sensor.

Figure 1.11 shows an example of low spatial resolution image acquired over Louisiana/Mississippi/Florida coast (in 2001), using the SeaWiFS sensor.

12 http://www.satimagingcorp.com/galleryimages/geoeye-1-olympic-stadium.jpg

Figure 1.11 Gulf Coast Sediments, along the Louisiana, Mississippi, Florida coast[13]

### 1.2.2.2 Medium resolution

Medium-resolution satellites typically give weekly to monthly coverage. These data have spatial resolutions from 100m to 1km and spectral bands ranging from light blue through to short-wave infrared (SWIR). Relatively large areas are covered by each satellite overpass. These data are suitable for a variety of information uses involving mapping, monitoring, and detection of land cover and land use features.

Remote sensing data with medium spatial resolution can provide useful information about Gross Primary Production (GPP), especially on the scale of urban areas. However, the work presented in [10] to compare the impact of spatial resolution on the detection of various ecosystems shows that high spatial resolution images provided more accurate estimates of maximum Gross Primary Production (GPP) than estimates derived from the medium spatial resolution. The main objective, presented in [11], is to examine and compare the effectiveness of two advanced algorithms for estimating impervious surfaces from medium spatial resolution satellite images, namely, linear spectral mixture analysis (LSMA) and artificial neural network (ANN).

Medium spatial resolution satellite examples are:

- Envisat: capturing 15 bands of 300 m resolution using MERIS sensor,
- RESURS-01-1: capturing 2 bands of 240 m resolution using MSU-S sensor, and
- IRS-1C: capturing 2 bands of 188 m resolution using WiFS sensor.

Figure 1.12 shows an example of medium spatial resolution image acquired using Envisat - MERIS on September 2008, over Iraq.

[13] http://eoimages.gsfc.nasa.gov/images/imagerecords/55000/55598/S2001072181646.L1A_HNAV.GulfCoastSediments.tif

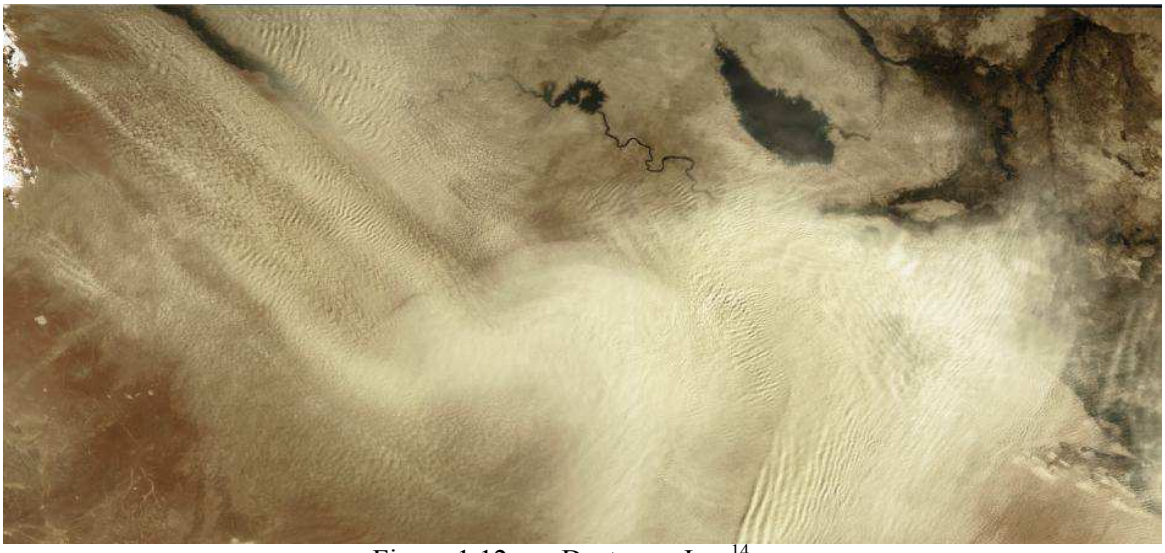

Figure 1.12 Dust over Iraq[14]

### 1.2.2.3 High and very high resolution

High spatial resolution satellites are characterized by pixel resolution higher than 1 m; in contrast of very high spatial resolution where the resolution is lower than 1 m. These data are obtained only in panchromatic mode, more often in combination of panchromatic and mulitspectral mode. Images can be collected over a particular area every 1-3 days but at very variable look angles. Majority of the satellites carry the most modern systems with great flexibility and capability to get data according to the very concrete requests.

High spatial resolution images find more and more applications in all domains. In [12], Petri et al. proposed a complete extraction method of the urban street network from very high spatial resolution images. [13] used data resources, from high spatial resolution satellite sensors, to study identification and planning of urban areas (size, infrastructure, location, etc). Additional typical applications include: 3D city models, urban studies, mapping of scattered vegetation, precision agriculture, control of agricultural activities, forests inventory, monitoring of a glacier lake, monitoring of open mines, soil erosion mapping, planning and design of linear infrastructures, mapping of transport infrastructure, insurance industry, the mapping of buildings destroyed by an earthquake, and planning and organization of humanitarian aid …

SPOT-5, Ikonos, QuickBird, WorldView-1, WorldView-2 and GeoEye-1 are some of the well-known high spatial resolution satellites. Example of Ikonos image with 0.8 m resolution is shown in figure 1.13 and of GeoEye-1 image with 0.5 m resolution is shown in figure 1.14.

[14] http://eoimages.gsfc.nasa.gov/images/imagerecords/35000/35412/Iraq_mer_2008258_lrg.jpg

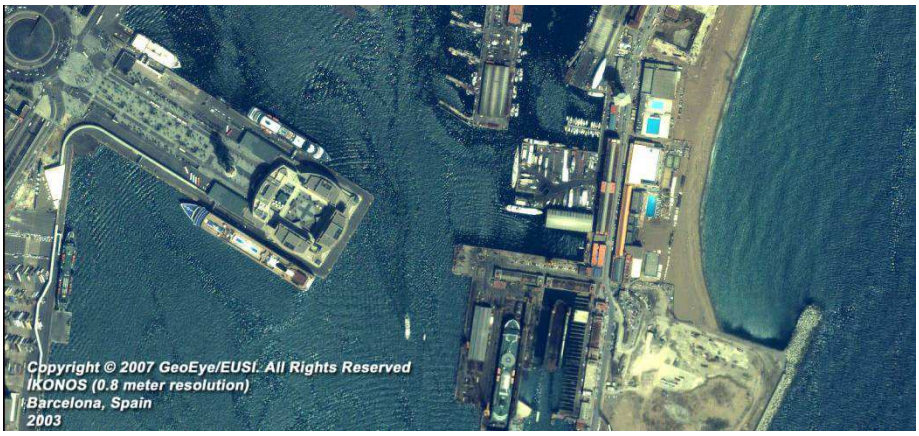


Figure 1.13 Image acquired by Ikonos over Barcelona, Spain, 2003, at 0.8 m spatial resolution[15]

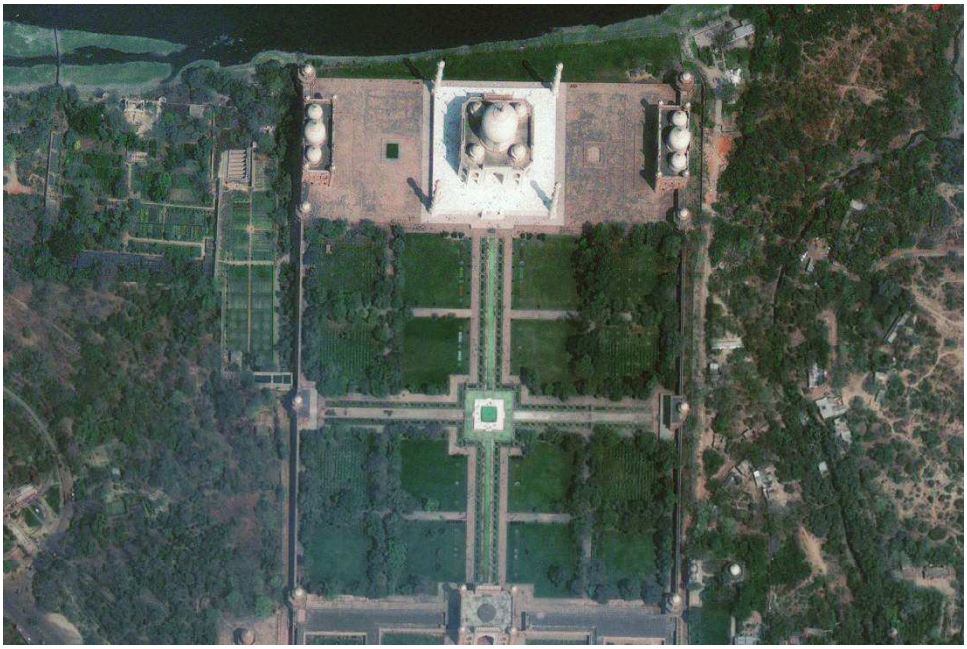

Figure 1.14 GeoEye-1 Taj Mahal, Agra, India, 2009, at 0.5m spatial resolution[16]

The spatial resolution required for detection, location, identification, and differentiation of objects on Earth surface are indicated below.

**1-meter spatial resolution**

- **Identify and map**: manhole covers, automobiles, bus shelters, highway lanes, sidewalks, utility equipment, fence line, and free-standing trees and bushes.
- **Identify**: characteristics features of many of above mentioned objects.
- **Detects**: small areas of stress in farm fields or tree stands.

[15] http://www.satimagingcorp.com/galleryimages/ikonos-barcelona-spain.jpg

[16] http://www.satimagingcorp.com/galleryimages/geoeye-1-taj-mahal.jpg

- **Locate and map**: houses, roads, building, courtyards, and small farm fields.
- **Differentiate**: among types of building and houses.

**10-meter spatial resolution**

- **Locate and map**: building, yards, roads, property boundaries, athletic fields, farm fields, and side streets.
- **Differentiate**: farm fields, tree stands and relatives vegetation health.
- **Make**: small-area land-cover classifications.

**20/30-meter spatial resolution**

- **Locate**: airports, city centers, suburbs, shopping malls, sport complexes, large factories, forest stands, and large farm fields.
- **Make**: generalized land-cover classifications.

**80-meter spatial resolution**

- **Map**: regional geological structure.
- **Assess**: vegetation health in a large region.

**1-Kilometer spatial resolution**

- **Assess**: vegetation indices for states and entire countries.
- **Track**: events like-insect infestation, drought and desertification.

In this thesis, we are interested in the application of high spatial images, three satellites images were used: Ikonos, QuickBird and WorldView-2. Hence, in the next section the primary characteristics of theses satellite will be considered.

## 1.3 Satellites characteristics

Remote sensing imagery is finding increasingly more acceptability and use. Remote sensing satellites are usually placed in sun-synchronous polar orbits, where the satellite passes all latitudes at the same local solar time each day. Orbits lie within 20 degrees of a 90 degree inclination from the equator. To introduce remote sensing applications, the properties of satellite images should be known in advance. Therefore, this section puts some light on some of high spatial resolution remote sensing satellites. A comparison of the main characteristics of existent high-resolution satellites are given in Table 1.1. Many others satellites are programmed to be launched in future, as:

- GeoEye-2 expected Early 2013 with a resolution of 0.25 m,
- WorldView-3 expected Mid 2014 with a resolution of 0.31 m

The area of the earth which is imaged during a satellite orbit is referred as swath. It can range in width from ten to hundreds of kilometers. As the satellite orbits the earth a different area is covered due to the earth's rotation. The elevation of the satellite orbit is designed so that the same location will be retraced in a period of several weeks. The remote sensing satellites we consider are Ikonos, Quickbird and Worldview-2.

### 1.3.1 Ikonos satellite:

Ikonos comes from the Greek word for "image". Ikonos satellite is a high-resolution satellite operated by GeoEye Inc.[17]. It was the first satellite to collect publicly available high-resolution imagery at 1 and 4 meter resolution. It was originated in 1991 under Lockheed Martin Corporation as the Commercial Remote Sensing Satellite project (CRSS).

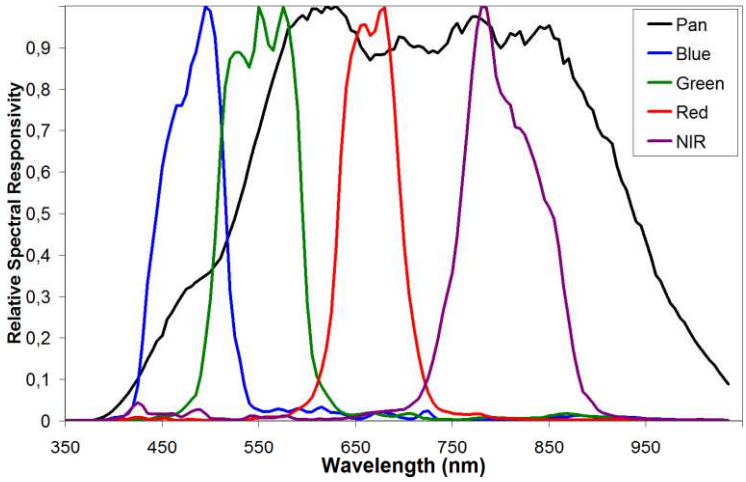


Figure 1.15 Ikonos Relative Spectral Response[18]

The launch of Ikonos-1 by Space Imaging Incorporation failed in September 24, 1999. On September 24, 1999, Ikonos -2, renamed Ikonos, was successfully launched. The Ikonos sensors produce four MS bands and one Pan band of 4- and 1-m resolutions respectively as shown in Fig 1.15. Detailed characteristics of this satellite are given in table 1.2.

### 1.3.2 QuickBird satellite:

QuickBird is a high-resolution commercial satellite, owned by DigitalGlobe[19] and launched in October 2001. The satellite collects panchromatic imagery at 0.6-meter resolution and multispectral imagery at 2.4-meter resolutions. The relative spectral response of QuickBird is shown in Fig 1.16. Table 1.3 details the main characteristics of this satellite. At this resolution, detail such as buildings and other infrastructure are easily visible. However, this resolution is insufficient for working with smaller objects.

[17] GeoEye, formerly Orbital Imaging Corporation or ORBIMAGE, is a commercial satellite imagery company.

[18] http://www.geoeye.com/CorpSite/assets/docs/technical-papers/2008/IKONOS_Relative_Spectral_Response.xls

[19] DigitalGlobe is a commercial vendor of space imagery and geospatial content, and operator of civilian remote sensing spacecraft.

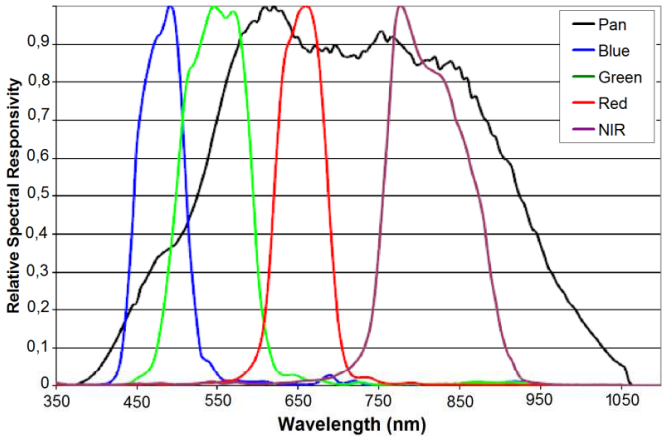


Figure 1.16 QuickBird Relative Spectral Response[20]

| | |
|---|---|
| Launch Date | 24 September 1999 |
| Launch Vehicle | Athena-2 |
| Launch Location | Vandenberg Air Force Base, California, USA |
| Orbit Altitude | 681 kilometers |
| Orbit Inclination | 98.1 degree, sun synchronous |
| Speed on Orbit | 7.5 kilometers per second |
| Equator Crossing Time | Nominally 10:30 AM solar time |
| Orbit Time | 98 minutes |
| Revisit Time | Approximately 3 days at 40° latitude |
| Swath width | 11.3 kilometers at nadir; 13.8 kilometers at 26° off-nadir |
| Geolocation Accuracy | 15 m (CE90%) |
| Dynamic Range | 11-bits per pixel |
| Resolution at Nadir | 0.82 meters panchromatic; 3.2 meters multispectral |
| Resolution 26° Off-Nadir | 1.0 meter panchromatic; 4.0 meters multispectral |
| Image Bands | Panchromatic, blue, green, red, near IR |

Table 1.2: Ikonos Satellite System: Sensor Characteristics

| | |
|---|---|
| Launch Date | October 18, 2001 |
| Launch Vehicle | Boeing Delta II |
| Launch Location | Vandenberg Air Force Base, California, USA |
| Orbit Altitude | 450 Km |
| Orbit Inclination | 97.2°, sun-synchronous |
| Speed on Orbit | 7.1 Km/sec |
| Equator Crossing Time | 10:30 AM (descending node) |
| Orbit Time | 93.5 minutes |
| Revisit Time | 1-3.5 days, depending on latitude (30° off-nadir) |
| Swath width | 16.5 Km x 16.5 Km at nadir |
| Metric Accuracy | 23 meter horizontal (CE90%) |
| Dynamic Range | 11 bits |
| Resolution at Nadir | 0.61 m panchromatic ; 2.44 m multispectral |
| Resolution 26° Off-Nadir | 0.72 m panchromatic ; 2.88 m multispectral |
| Image Bands | Panchromatic, blue, green, red, near IR |

Table 1.3: QuickBird Satellite System: Sensor Characteristics

[20] http://www.digitalglobe.com/downloads/DigitalGlobe_Spectral_Response.pdf

This satellite is an excellent source of environmental data useful for changes analysis in land usage, agricultural and forest climates. QuickBird's imaging capabilities can be applied to a host of industries, including oil and gas exploration & production, engineering and construction and environmental studies. The data contributes to mapping, agricultural and urban planning, weather research and military surveillance. QuickBird launched on a Boeing Delta II rocket from Vandenberg Air Force Base, California.

### 1.3.3 WorldView-2 satellite:

DigitalGlobe's WorldView-2 Satellite, launched on October 8, 2009, provides 0.5m Panchromatic mono and stereo satellite image data. With its improved agility, WorldView-2 is able to act like a paintbrush, sweeping back and forth to collect very large areas of multispectral imagery in a single pass. The combination of WorldView-2's increased agility and high altitude enables it to typically revisit any place on earth in 1.1 days.

The WorldView-2 sensor provides high-resolution panchromatic band and eight (8) multispectral bands; four (4) standard colors (red, green, blue, and near-infrared 1) and four (4) new bands (coastal, yellow, red edge, and near-infrared 2), full-color images for enhanced spectral analysis, mapping and monitoring applications, land-use planning, disaster relief, exploration, defence and intelligence, and visualization and simulation environments. The arrangement of these bands is given in figure 1.17.

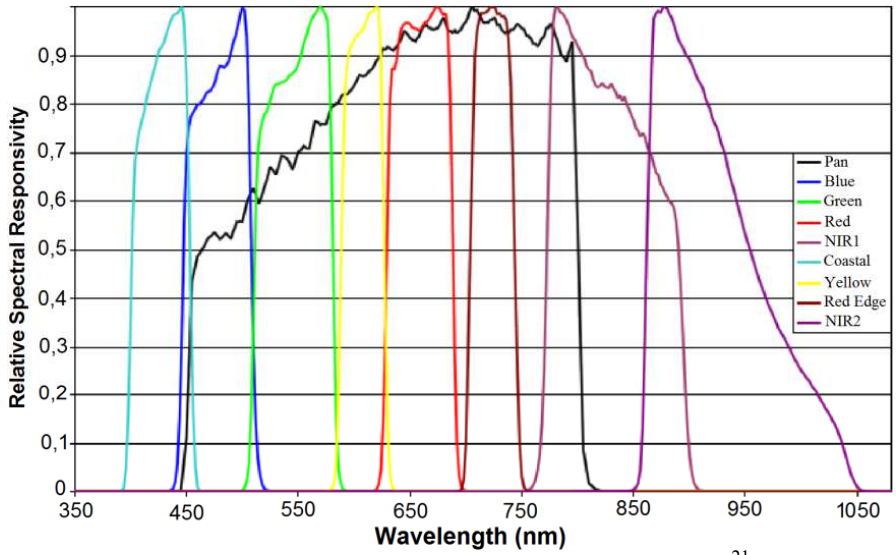


Figure 1.17 Worldview-2 Relative Spectral Response[21]

The four 4 new bands are described as:

- Coastal Band (400 - 450 nm): this band supports vegetation identification and analysis, and bathymetric studies based upon its chlorophyll and water penetration characteristics. Also, this

[21] Source http://www.digitalglobe.com/downloads/DigitalGlobe_Spectral_Response.pdf

band is subject to atmospheric scattering and will be used to investigate atmospheric correction techniques.

- Yellow Band (585 - 625 nm): used to identify "yellow-ness" characteristics of targets, important for vegetation applications. Also, this band assists in the development of "true-color" hue correction for human vision representation.
- Red Edge Band (705 - 745 nm): aids in the analysis of vegetative condition. Directly related to plant health revealed through chlorophyll production.
- Near Infrared 2 Band (860 - 1040 nm): this band overlaps the NIR 1 band but is less affected by atmospheric influence than Near Infrared 1 band. It supports vegetation analysis and biomass studies.

Some of the most important characteristics of WorldView-2 are provided in Table 1.4.

| | |
|---|---|
| Launch Date | October 8, 2009 |
| Launch Vehicle | Delta 7920 (9 strap-ons) |
| Launch Location | Vandenberg Air Force Base, California, USA |
| Orbit Altitude | 770 kilometers |
| Orbit Inclination | sun synchronous |
| Speed on Orbit | 7.5 kilometers per second |
| Equator Crossing Time | 10:30 am (LT) descending Node |
| Orbit Time | 100 minutes |
| Revisit Time | 1 day |
| Swath width | 16.4 kilometers at nadir; off-nadir |
| Geolocation Accuracy | Specification of 12.2m CE90 |
| Dynamic Range | 11-bits per pixel |
| Resolution at Nadir | 0.46 meters panchromatic; 1.8 meters multispectral |
| Resolution 20° Off-Nadir | 0.52 meter panchromatic; 1.4 meters multispectral |
| Image Bands | panchromatic, coastal, blue, green, yellow, red, red edge, NIR1, NIR2 |

Table 1.4: WorldView-2 Satellite System: Sensor Characteristics

The WorldView-2 imaging payload is the second such system engineered and manufactured by ITT Space Systems Division for DigitalGlobe. Once deployed, it operate at an altitude of 770 kilometers, and the advanced on-board imaging system will capture pansharpened, multispectral images (with better than 0.5-meter resolution) from almost 800 kms above the Earth. These images supply unprecedented detail and geospatial accuracy, further expanding the applications for satellite imagery in both commercial and government markets. Added spectral diversity provides the ability to perform precise change detection and mapping.

In addition to numerous other technical improvements, WorldView-2 also has the ability to accommodate direct tasking, which will allow select customers around the world to load imaging profiles directly up to the spacecraft and execute delivery of the data directly down to their own ground stations.

| Satellite | Altitude (km) | Revisit time (day) | Orbit inclination | Image swath | Launch Date | Multispectral bands range (μm) | | | | Pan | Max Resolution |
|---|---|---|---|---|---|---|---|---|---|---|---|
| | | | | | | B | G | R | NIR | | |
| **Ikonos** | 681 | 2-3 | 98.1° | 13.8 km | September 24, 1999 | 0.45 – 0.52 | 0.52 – 0.60 | 0.63 – 0.69 | 0.76 – 0.90 | 0.45-0.90 | 4.00 m<br>0.82 m |
| **QuickBird** | 482, 450 | 2-3 | 98° | 18 km | October 18, 2001 | 0.45 – 0.52 | 0.52 – 0.60 | 0.63 – 0.69 | 0.76 – 0.90 | 0.45-0.90 | 2.44 m<br>0.61 m |
| **Orbview-3** | 470 | 2-3 | 98.2° | 8 km | June 26, 2003 | 0.45 – 0.52 | 0.52 – 0.60 | 0.625 – 0.695 | 0.76 – 0.90 | 0.45 – 0.90 | 4.00 m<br>1.00 m |
| **Resurs-DK1** | 330, 500 | 6 | 64.8° – 70.4° | 4.7 – 28.3 km | June 15, 2006 | - | 0.50 – 0.60 | 0.60 – 0.70 | 0.70 – 0.8 | 0.58 – 0.80 | 1.50 m<br>0.90 m |
| **KompSat-2** | 685 | 3 | 98° | 15km | July 28, 2006 | 0.45 – 0.52 | 0.52 – 0.60 | 0.63 – 0.69 | 0.76 – 0.90 | 0.50 – 0.90 | 4.00 m<br>1.00 m |
| **WorldView-1** | 496 | 1.7 | 98° | 17.6 km | September 18, 2007 | - | - | - | - | 0.40 – 0.90 | -<br>0.50 m |
| **GeoEye-1** | 684 | 2 | 98° | 15.2 km | September 6, 2008 | 0.45 – 0.51 | 0.51 – 0.58 | 0.655 – 0.69 | 0.78 – 0.92 | 0.45 – 0.80 | 1.65 m<br>0.41 m |
| **WorldView-2*** | 770 | 1 | 98° | 17.25 km | October 8, 2009 | 0.45 – 0.51 | 0.51 – 0.58 | 0.63 – 0.69 | 0.77 – 0.895 | 0.45 – 0.80 | 1.85 m<br>0.46 m |
| **Pleiades-1** | 694 | 1 | 98° | 20 km | December 16, 2011 | 0.43 – 0.55 | 0.49 – 0.61 | 0.60 – 0.72 | 0.75 – 0.95 | 0.48 – 0.83 | 2.00 m<br>0.50 m |

Table 1.5: Sources of high spatial resolution satellite-borne optical images

* In addition to the four primary multispectral bands, WorldView2 offers the following multispectral bands:

Coastal band (0.400 μm – 0.450 μm),

Yellow band (0.585 μm – 0.625 μm),

Red Edge band (0.705 μm – 0.745 μm), and

Near-IR2 band (0.860 μm – 0.104 μm).

Satellite images find use in large number of applications as weather forecasting, disaster assessment, agricultural research, natural resources exploration, vegetation cover mapping, rural and urban land use, cartography, extraction of road network and urban planning.

Usually, the natural land-covers are classified into three categories: water, soil and vegetation. Each class, distinguished via its spectral signature, is subdivides into several other subclasses. Mapping the vegetation-covers is useful in wide number of applications. In this thesis, we are interested into extracting vegetation from satellite image without considering its subclasses. Generally, a combination of MS bands is used to delineate the vegetation. This combination is called a vegetation index. In the next section, some of the most used indexes are presented.

## 1.4 Vegetation indices

Need for a resumed characterization of data issued from different bands and able to characterize vegetation, the vegetation index (VI) combines the bands that best characterize vegetation into a single measure. Many vegetation indices have been developed. Some are the basic indices, which are simple combinations of red (R) and infrared (NIR) bands like NDVI, RVI, DVI and TDVI as shown in table 1.6.

| Vegetation index (VI) | Equation | Reference |
|---|---|---|
| Difference VI | DVI=NIR-R | [14] |
| Ratio VI | RVI=NIR/R | [15] |
| Normalised difference VI | NDVI=(NIR-R)/(NIR+R) | [16] |
| TDVI | $TDVI = 1.5 \times \frac{(NIR - R)}{\sqrt{NIR^2 + R + 0.5}}$ | [17] |
| Perpendicular VI | PVI=aNIR-bR+c | [18] |
| Soil adjusted VI | $SAVI = \frac{(1+L)(NIR - R)}{NIR + R + L}$, typically L = 0.5. | [19] |
| Weighted difference VI | WDVI=NIR-aR; a is the slope of the soil line | [20] |
| Modified SAVI | $MSAVI2 = NIR + 0.5 - 0.5\sqrt{(2NIR+1)^2 - 8(NIR - R)}$ | [21] |
| Infrared Percentage VI | IPVI=NIR/(NIR+R) | [22] |
| Transformed SAVI | TSAVI= s(NIR-s*R-a)/ (a*NIR+R-a*s+X*(1+s*s)), where a is the soil line intercept, s is the soil line slope, and X is an adjustment factor which is set to minimize soil noise (0.08 in original papers). | [23] |
| Atmospherically resistant VI | ARVI = (NIR-rb)/ (NIR+rb),with rb defined as: rb = R - gamma*(R - B) and gamma usually equal to 1.0 | [24] |
| EVI Enhanced Vegetation Index | EVI=Gain*(NIR-R)/(NIR+$C_1$R-$C_2$B+L), where L is the canopy background adjustment and $C_1$, $C_2$ are the coefficients of the aerosol resistance term, which uses the blue band to correct for aerosol influences in the red band. The coefficients adopted in the MODIS-EVI algorithm are; L=1, $C_1$ = 6, $C_2$ = 7.5, and G = 2.5. | [25] |
| Global Environment Monitoring Index | GEMI = eta*(1-0.25*eta)- (R - 0.125)/( 1 – R), where eta = (2*($NIR^2$-$R^2$)+1.5*NIR+0.5*R)/( NIR + R + 0.5) | [26] |

Table 1.6: Vegetation indices

There is a strong correlation between linear combinations of R and NIR bands and green leaf area and biomass. It can estimate gross primary productivity. The normalised difference vegetation index (NDVI) is one of the most successful and well-known indices used to detect live green plant canopies in multi-spectral remote sensing data. It varies between -1 and 1, where vegetated areas typically have values greater than zero, whereas values near or below zero show non-vegetated surfaces such as water, barren land, ice, snow, or clouds. Table 1.7 shows the typical NDVI values for various subclasses of land-covers and its capacity to distinguish vegetated areas broadly from other surface types.

| Land-cover type | Reflectance | | NDVI value |
|---|---|---|---|
| | near-infrared | Red | |
| free standing water | very low | Low | negative ~-0.3 |
| soils or rocks | somewhat larger than the red | somewhat smaller than the infrared | small positive from 0.1 to 0.2 |
| live green vegetation | high | low | from 0.5 to ~1 |
| snow and ice | low ~0.4 | slightly lower than infrared | very slightly negative value |

Table 1.7: Typical NDVI values for various land-covers

NDVI can be used to estimate the photosynthetic capacity of plant canopies, the green leaf area index, the evapo-transpiration taking place in the vegetation, the biomass, the chlorophyll concentration, the plant productivity, the accumulated rainfall. Figure 1.18 shows the non-linear response of NDVI to the vegetation cover density.

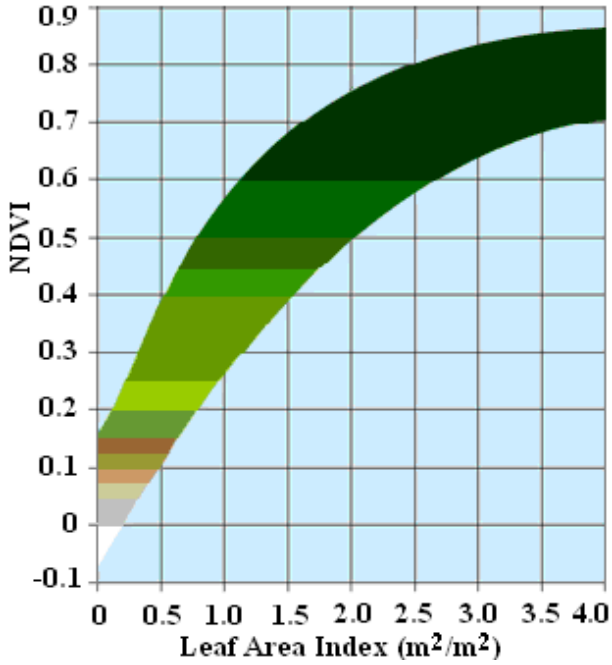


Figure 1.18 NDVI vs. LAI[22]

[22] Source: http://rangeview.arizona.edu/Tutorials/intro.asp

Some indices are able to minimise soil influences as PVI, WDVI, SAVI, MSAVI. In the other hand, some ones are developed to minimise atmospheric noise.

The author in [22] found that, in NDVI formula, the subtraction of the red in the numerator was irrelevant, and proposed the IPVI index as a way of improving calculation speed. It also is restricted to values between 0 and 1, which eliminates the need for storing a sign for the vegetation index values.

TSAVI is the Transformed SAVI which assumes that the soil line has arbitrary slope and intercept, and it makes use of these values to adjust the vegetation index. ARVI is the first of the atmospherically resistant indices. The red reflectance in NDVI formula is replaced with the term: rb = R - gamma (B - R).

GEMI is the Global Environmental Monitoring Index which was developed by Pinty and Verstraete. It meets the author's requirements of insensitivity to the atmosphere empirically. Finally, the enhanced vegetation index (EVI) is an optimized index designed to enhance the vegetation signal with improved sensitivity in high biomass regions and improved vegetation monitoring through a decoupling of the canopy background signal and a reduction in atmosphere influences.

## 1.5 Conclusion

The remote sensing satellites such as Ikonos, QuickBird and WorldView-2 provide MS and Pan images with very high spatial resolution. These images are increasingly used in several domains, such as: vegetation identification, vegetation analysis, biomass studies, bathymetric, extraction of urban street network, identification and planning of urban areas, the mapping of buildings destroyed by an earthquake …

Moreover, the MS images can be used to derive vegetation indices. However, the remote sensing experts often consider that MS data on a pixel is insufficient so they emphasise on using the spatial context (Pan image). This leads to use Pan images or fused MS and Pan images. The image fusion techniques, called also pansharpening, have been used to bring the resolution of the multispectral imagery at par with that of the panchromatic images. This is detailed in the next chapter.

# 2

# Pansharpening categories

## 2.1 Introduction

Earth observation is currently developing more rapidly than ever before. Currently, a large number of satellites have been growing progressively, such as SPOT [27], Landsat 7 [28], Ikonos [29], OrbView [30], QuickBird and WorldView [31]. The coverage of the Earth in space and in the electromagnetic spectrum, as well as the acquisition frequency are also quickly increasing. Typically a satellite provides a combination of multi-spectral (MS) images, and a panchromatic (Pan) image of a higher spatial resolution than that of MS. It is possible to merge the Pan and MS images in order to produce MS images with higher spatial resolutions by using suitable algorithms. This concept is known as pansharpening or MS and Pan image fusion [1]. Pansharpening is shorthand for panchromatic sharpening, where the Pan image is used to "sharpen" the MS image. In this case, to "sharpen" signifies to increase the spatial resolution of an MS image [3]. Consequently, an ideal pansharpening method, besides preserving the spectral details of the MS image, brings the total spatial information of the Pan image to produce an image with both high spectral and high spatial resolutions.

Wald in [2] defines image fusion as: "a formal framework in which are expressed means and tools for the alliance of data originating from different sources. It aims at obtaining information of greater quality; the exact definition of 'greater quality' will depend upon the application. Recently, pansharpening algorithms have received increasingly attention which has led to the development of a vast number of techniques. Pansharpening is used in many real-world applications such as change monitoring, objects detection and classification (e.g., buildings, roads, vegetation, rivers, mountains and towns) [32]. The need of images with low or high spatial resolution depends on the considered

application. Images with low spatial resolution and repetitive coverage are preferred in some cases like meteorology applications. In other applications like mapping, just the propriety of high spatial resolution is required. In contrast, military applications may need both high resolution and frequent coverage [1].

In this chapter, we present the state of the art of pansharpening methods described in the literature based on the recent categorization given in [3]. Moreover, some of the most useful algorithms used before applying pansharpening will be first presented in the pre-processing section. Examples are interpolation and histogram matching.

## 2.2 Pre-processing

Generally, many pre-processing operations are used in remote sensing imagery. Some of them try to decrease distortions issued from sensors and platforms. Such radiometric and geometrical distortions are due to: variations in scene illumination, viewing geometry, atmospheric conditions, sensor response and sensor noise [33]. Corrections for these distortions are needed for comparing multimodal and multi-date images, or in mosaicing applications. Although applying methods to correct distortions, algorithms for image enhancement are required for visual interpretation and understanding of imagery. In this section, we are mostly interested in algorithms including mainly registration, interpolation and histogram matching techniques.

### 2.2.1 Image registration

Image registration is one of the most widely used image processing operations in remote sensing. It is a process by which the most accurate match is determined between two images which have been taken at the same or different viewpoints and/or by different sensors [34]. Typically, this process is required in remote sensing, medicine, cartography, computer vision, etc. Many applications of remote sensing require two or more scenes of the same geographical region, acquired at different dates or from different sensors, in order to be processed together. In this case, the role of image registration is to make the pixels in different images coincide precisely [1]. If a map coordinate base exists, then each image is separately registered to this map, otherwise one image can be chosen as a reference to which the other is registered [3]. The process of registration has to handle problems like contrast reversal, multiple intensity and features present in one image that may not appear in the other image.

Several algorithms for image registration have been proposed in the literature [35], [36], [37], [38], [39], [40], [34], [41]… Usually, registration techniques are based on one of two approaches. The feature matching approach, which aims to extract and match features across the image as two independent steps; and the area matching approach, which uses a metric to match regions of the image without explicitly extracting features. Area-based methods are not well adapted to the

multisensor image registration problem [40] due to the possible dissimilarity of gray-level values of the images to be matched. In contrast, feature-based techniques have been shown to be more suitable for this task. In next section, the interpolation process is briefly introduced.

### 2.2.2 Image upsampling and interpolation

The acquired MS images have low spatial resolution compared to the Pan images. In order to apply pansharpening algorithms, MS images must be upsampled to the same resolution as Pan images. The upsampling process may involve interpolation, usually performed via convolution of the image with an interpolation kernel [42]. The commonly employed linear interpolation methods, such as nearest neighbour, bilinear interpolation, and cubic convolution, have advantages in simplicity and fast implementation. In the literature, several interpolation methods for various applications have been proposed. Nearest neighbour resampling uses the pixel value in the original image which is nearest to the new pixel location in the resampled image. This is the simplest technique which preserves the original values; nevertheless it may duplicate some pixels. In addition, distortions as blocky image appearance may be observed. Bilinear interpolation resampling considers the closest 2x2 neighborhood, then takes a weighted average of these four pixels in the original image nearest to arrive at its final interpolated value. The averaging process affects the original pixel values. This results in much smoother looking images than nearest neighbor. This may be undesirable if further processing and analysis, such as classification based on spectral response, is to be done. Cubic convolution resampling goes even further by considering the closest 4x4 neighborhood of known pixels to calculate a distance weighted average. Generally, cubic convolution generates sharper images compared to nearest and bilinear interpolation. On the other hand, this method alters pixel values [33]. More than 40 spatial interpolation methods are briefly described in [43]. Among them, some have been proposed specifically to remote sensing [44]. Figure 2.1 shows examples of spatial interpolation of an image.

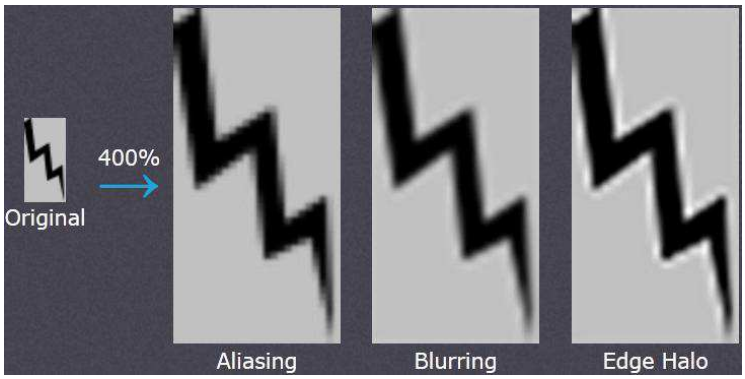


Figure 2.1 Interpolation artifacts[1]

[1] Source: http://www.cambridgeincolour.com/tutorials/image-interpolation.htm

Most of the interpolation methods attempt to reduce the artifacts: edge halos, blurring and aliasing, shown in figure 2.1. In [45], the authors apply five interpolation methods to remote sensing images in order to find the most suitable method for remote sensing images. At first, the authors used the standard methods of interpolation: nearest neighbour, bilinear and cubic. Then, they considered the interpolation with: smoothing filter, sharpening filter, and unsharp masking. Unlike the smoothing filter, sharpening filter enhances blurred fine details but introduces aliasing in the resulting image. Interpolation with unsharp filter may reduce the aliasing artefact by subtracting the blurred version of an image from the image itself. The obtained results in [45] show that all the five interpolation methods can produce good quality for high resolution image; but only bilinear, smoothing and unsharp filters interpolations are suitable for low resolution image. These conclusions were conducted based only on the mean square error (MSE) measure. We think that more evaluation indices must be considered before concluding, indices measuring spatial and spectral qualities are needed in this case see [46]. In the next section, histogram stretching is considered. This pre-processing technique is very used for displaying images.

### 2.2.3 Histogram stretching and matching

The histogram of an image represents the statistical distribution of the luminance values comprised in an image. It is a useful tool for contrast enhancement. For example, a common contrast enhancement technique “stretches” the range of luminance values and “clips” it at both ends, resulting in a certain percentage of saturated pixels. Example is shown in figure 2.2; here a Pan image and its corresponding histogram are shown before and after histogram stretching in the upper and lower parts of the figure, respectively.

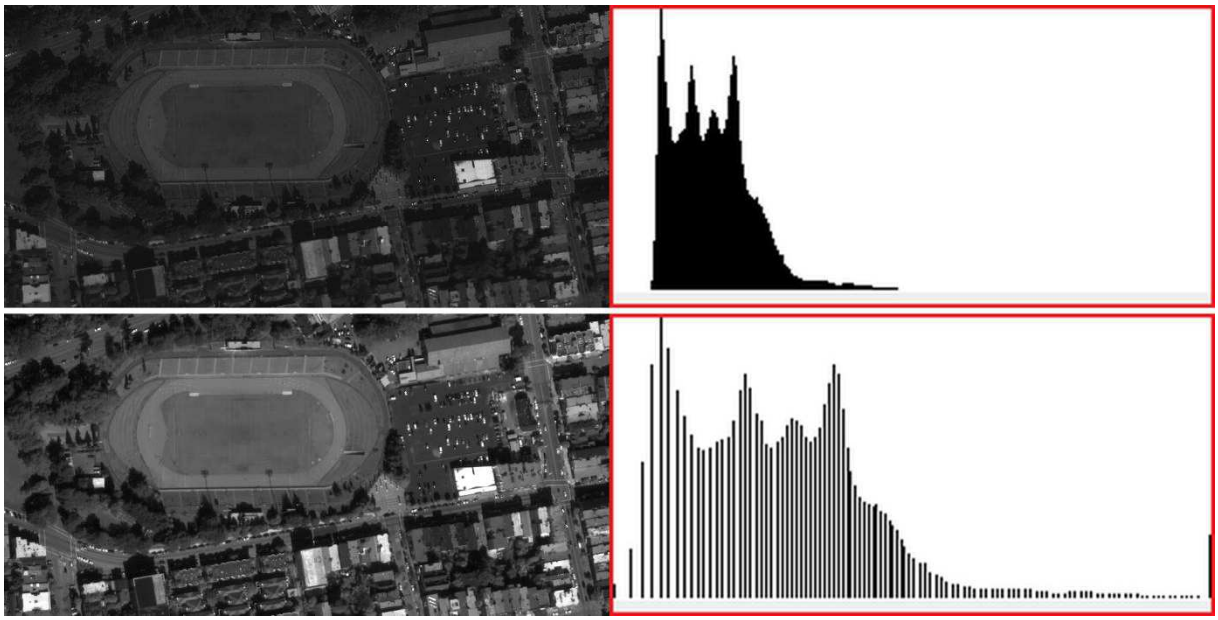

Figure 2.2 Histogram stretching example.

Pansharpening algorithms like those based on intensity-hue-saturation (IHS), suppose that the spectral characteristics of the Pan image match those of a transformed image based on the MS image. However, this is not generally the case [47]. This dissimilarity of the spectral characteristics of the Pan and MS images produces spectral distortions. To reduce brightness mismatching during pansharpening process and hence minimizing spectral distortion of the results, a histogram matching of the Pan and MS bands is conducted before fusion. The authors in [47] and [42] provide general purpose histogram matching techniques that could be used in remote sensing. However, the author in [48] presents a technique which is more appropriate for pansharpening. This method adjusts the value of the Pan image at each pixel (i, j) as

$$Matched_{Pan}(i,j) = (Pan(i,j) - \mu_{Pan})\frac{\sigma_b}{\sigma_{Pan}} + \mu_b \tag{2.1}$$

where $\mu_{Pan}$ and $\mu_b$ are the mean values of the Pan and MS image band b, respectively, and $\sigma_{Pan}$ and $\sigma_b$ are the standard deviation of the Pan and MS image band b, respectively. Equation (2.1) assures the range similarity of the mean and standard deviation of the Pan image and MS bands. By doing this, the mean value and standard deviation of the matched Pan image is approximated to those of the bands

## 2.3 Pansharpening categories

A large collection of pansharpening techniques have been proposed in the literature. Among the huge number of these techniques, the widely used methods include intensity-hue-saturation (IHS), high-pass filtering (HPF), principal component analysis (PCA), Brovey and wavelet transforms [49]. In [50], a review of these classical methods is provided. The launch of the SPOT satellite in 1986 has allowed civilian community of remote sensing to use high resolution MS images. The IHS transform was used in [51] to merge MS and Pan images of the SPOT satellite. Chavez et al. [52] used the high-pass filtering (HPF) method of minimizing the spectral distortion in the resulting images. This algorithm was applied to sharpen Landsat Thematic Mapper (TM) images with SPOT Pan images. The high-frequency information of the Pan image, related to spatial information, is extracted using a high-pass filter, then injected into the MS image. The HPF principally were used in several pansharpening methods, using different tools for extracting spatial information and injecting it in MS images as: the discrete wavelet transform [53], [54], [55], [56], the generalized Laplacian pyramid algorithms [57], [58], or “à trous” wavelet transforms [59], [60]. Recently, authors in [61] introduced the Contourlet transform and showed that it is better than the Wavelet transform. Hence Contourlet was used in the pansharpening process like in [62] and [63].

Image fusion methods have been classified in several ways. The authors in [50] proposed to classify pansharpening in three categories corresponding to three different processing levels, i.e., pixel level, feature level, and the decision level. Many other authors shared this idea, however

author in [64] emphases that the boundaries between the three levels are unclear. So in some situations, it becomes controversial to decide the level of the fusion to perform. Moreover, the author in [2] declared that this categorization may be misleading and it may falsely imply that fusion processes do not deal simultaneously with these different levels. Hence, he proposed another categorisation, where three types of methods have been identified: projection and substitution methods, relative spectral contribution methods and those relevant to the ARSIS concept (from its French acronym "Amélioration de la Résolution Spatiale par Injection de Structures" which means "Enhancement of the spatial resolution by structure injections").

The authors in [65] sort the methods into groups with respect to their main design idea. The following groups were defined.

- Transformation based fusion: like IHS and PCA.
- Addition and multiplication fusion: like method (P+XS).
- Filter fusion: like HPF method.
- Fusion based on inter-band relations.
- Wavelet decomposition fusion
- And finally further fusion methods: like fusion methods based on statistical properties.

The HPF and wavelet methods can be classified in the ARSIS group [66]; however the authors in [67] claim that these methods could belong to an IHS-like image fusion method group.

Another classification given in [1] defines three categories: spectral domain, spatial domain and scale-space techniques.

The authors in [68], [69] proposed two generalized frameworks for methods such as IHS, PCA, HPF or AWT and provided detailed relationships between them.

Recently, the authors in [3] provide a review of many pansharpening methods with a categorization of them. We chose to adopt this classification in order to establish a state of the art of existing fusion methods. Based on the used technique, five categories are defined and presented in respective paragraphs:

1- Component Substitution (CS) category: after a linear transform, it is based on the substitution of some bands. Examples are methods using IHS and PCA.
2- Relative Spectral Contribution category: the fused results are obtained by a linear combination of the spectral bands. Examples are methods using the Brovey Transform and P+XS.
3- High-Frequency Injection category: spatial details extracted from the Pan image, using a high pass filter, are injected in the MS images. An example is HPF.
4- Methods based on the statistics of the image, as Bayesian-based and super-resolution methods.

5- Multiresolution category: it is based on a multiresolution analysis like generalized Laplacian pyramid, wavelet and contourlet methods. Moreover, techniques combining multiresolution analysis with methods from other categories, like a combination of wavelet and IHS, belong to this group.

It should be noted that some methods can be classified into more than one category. In this thesis, our main contributions are in the CS and multiresolution categories, hence they will be more considered than the rest of the categories in the following sections.

### 2.3.1 Component substitution category

The basic idea used in this category is to separate for MS images the spatial information from the spectral information, using a linear transform, then to replace the spatial information by that from Pan image. The spatial component, generated by the linear transform, and the Pan image, which replaces this component, must have the same spectral information in order to minimise the spectral distortion in the resulting images.

The CS category includes various well-known image fusion methods, such as IHS and PCA algorithms [70]. In [67], the authors studied fast IHS fusion techniques and proposed a general algorithm for CS sharpening. Merging Pan and MS data using CS technique involves five steps [3]:

1. Upsampling the MS image to the size of the Pan image.
2. Linear transforming of the MS image to the desired components.
3. Matching the histogram of the Pan image with the component to be substituted.
4. Replacing the component with the higher spatial resolution data derived from the histogram-matched Pan image.
5. Transforming back the components to obtain the pansharpened image.

Based on this algorithm, Wang et al. [68] and Aiazzi et al. [69] proposed a general image fusion and extended the GIF (EGIF) protocol, respectively.

In general, the characteristics of the histogram-matched Pan and intensity (*I*) component are different, leading to a noticeable color distortion, when the obtained fused results are displayed in color composition [71]. This is due to the difference in the spectral response of the Pan image and the *I* component resulting from combinations of MS images.

In the CS group, the IHS-based pansharpening methods are applied to MS images composed by three bands, and the PCA-based pansharpening techniques are used when the number of bands is larger. However, the fast IHS pansharpening method proposed in [72] can extend traditional three-order transformations to an arbitrary order. In summary, methods of CS category are fast and easy to implement; however, they suffer from spectral distortions due to dissimilarities between

characteristics of Pan and MS images [73], [74]. To overcome this weakness, some solutions were proposed in [75], [76], [77], [78] and [79].

### The Intensity-Hue-Saturation (IHS) pansharpening method:

IHS is a color space transform, where hue (H) is defined as the predominant wavelength of a color, saturation (S) is defined as the purity or total amount of white light of a color and intensity (I) relates to the total amount of light that reaches the eye [80]. The IHS-based fusion technique is one of the most commonly used methods for pansharpening [81]. However, through literature, many formulas are proposed. A detailed list of formulas can be found in [82], where ten IHS based method for pansharpening were tested to verify the most appropriate formulas for fusion applications. The IHS transform separates the spatial information as I component from the spectral information represented by the H and S components. The main steps of the standard IHS fusion scheme are shown in figure 2.3.

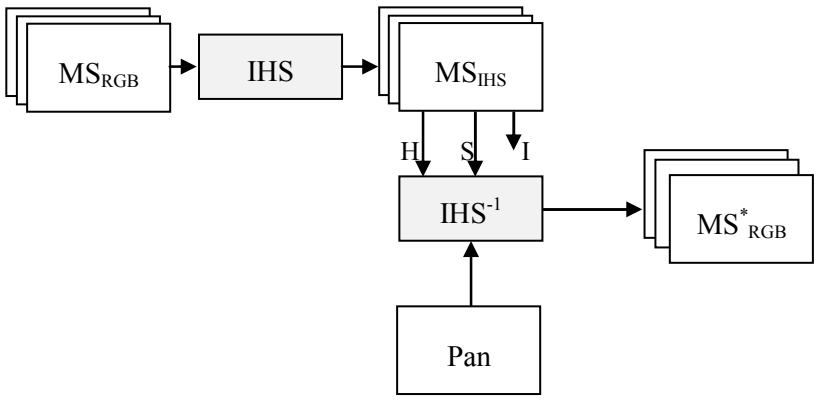


Figure 2.3 Standard IHS fusion scheme.

This scheme can include more steps to improve the pansharpening, as: MS and Pan registration, MS upsampling to the same size as the Pan image, and histogram matching of Pan image to MS images. Basically, the upsampled MS image is transformed from the RGB color space into IHS space to produce three components I, H and S. The Pan image is histogram-matched to the intensity component I. The combination of the obtained Pan image, the H and S components, is transformed back into the RGB space to produce the pansharpened image.

In figure 2.4, an example of pansharpening Worldview 2 MS and Pan images, using an IHS method is illustrated. The example was chosen with large vegetated areas to show spectral distortions introduced by IHS method, especially in the vegetation zones.

IHS transform was used in fusing Radar and Landsat TM [80], merging information contents of the Landsat TM and SPOT [83] and for geological mapping [84]. In addition, IHS was used with multiresolution transforms such as wavelet [59] and [60] for fusion purpose.

Several IHS-based pansharpening techniques have been proposed. Fast and generalized IHS pansharpening methods, which can be used even when the number of MS bands is greater than three, were proposed in [67] and [72]. The authors tried to minimise the color distortions too by adapting the IHS to the Ikonos spectral response. The same idea was used in [79] for any satellite images. Moreover, for vegetation visualization applications, recent methods make use of vegetation enhancement to improve color quality [85], [86], [78]. This enhancement is applied in the vegetation areas, which are delimited using a vegetation index (VI).

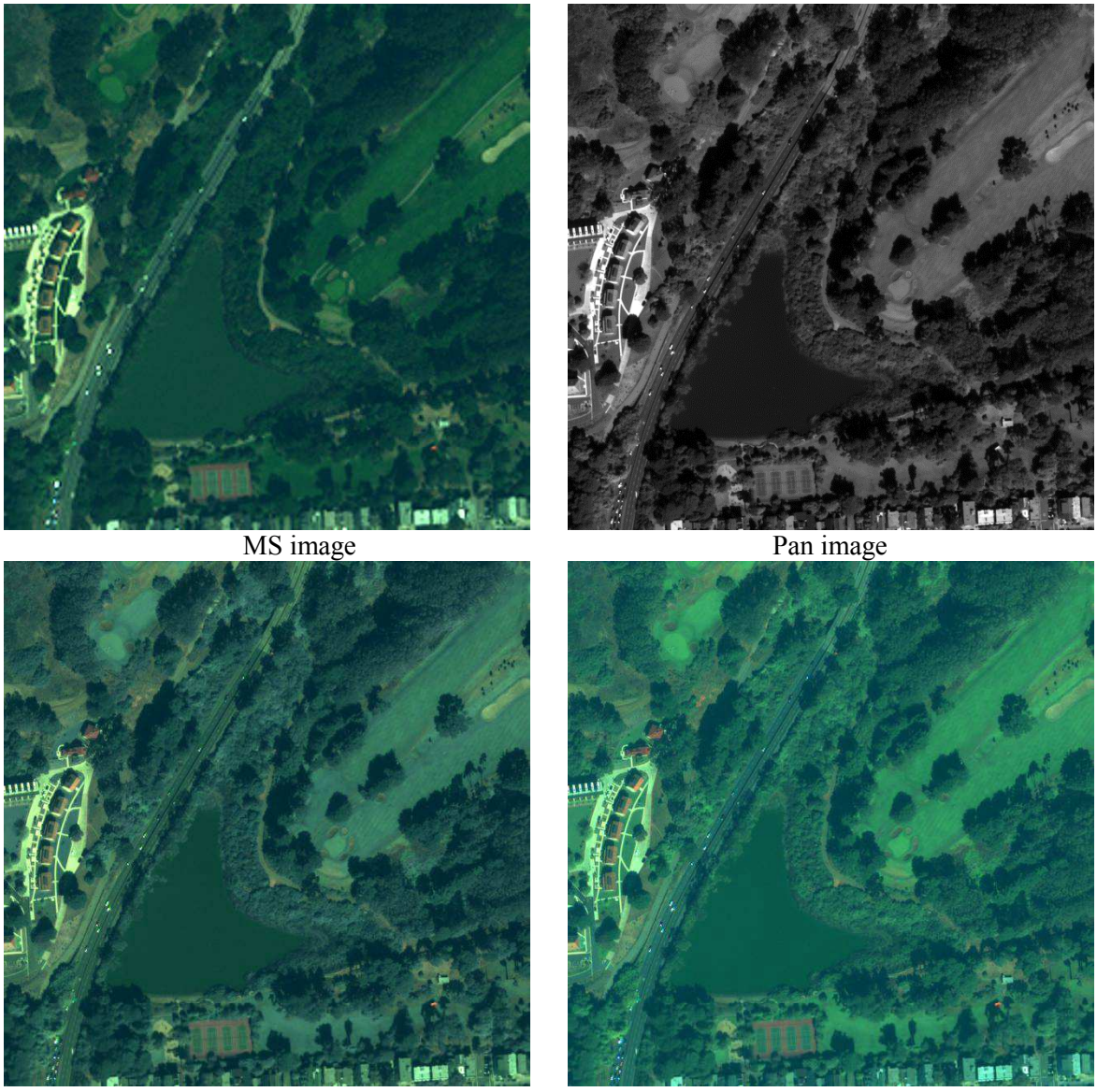

MS image Pan image

IHS fused result PCA fused result

Figure 2.4 IHS and PCA pansharpening Examples using WorldView 2.

### The principal component substitution pansharpening method:

This is another method in the CS family relying on the principal component analysis (PCA) transform. Depending on the field of application, it is also named the discrete Karhunen–Loève transform (KLT), the Hotelling transform or proper orthogonal decomposition (POD). PCA is

widely used in signal processing, statistics, and many other applications. PCA transforms a set of observations of possibly correlated variables into a dataset of new uncorrelated linear combinations of the original variables called principal components [50]. Theoretically, the largest possible variance is mapped to the first principal component (PC1); this means that common information such as spatial one is concentrated in PC1 [87]. In contrast, specific information, with decreasing variance, such as spectral information, is contained to the following components. In PCA, the variance is preserved, i.e. the total variance of input variables is equal to the sum of the variances in all the components. This characteristic of separating spatial and spectral information of a set of input images is the motivation of using PCA for pansharpening. Moreover, the number of input variables is not limited, making PCS adequate to pansharpening MS images with a large number of bands. As shown in figure 2.4, the PCA fused image presents less spectral distortion than the IHS fused image, since, in theory, PC1 is more similar to the Pan image than the I component [83]. Nevertheless, the PCS is sensitive to the choice of the area to be analyzed. The correlation coefficient reflects the tightness of a relation for a homogeneous sample, while shifts in the band values due to obviously different cover types will influence the correlations and particularly the variances [50]. PCS was used to fuse Landsat TM and SPOT data in [83]. In some cases, as shown in [77], instead of having PC1 as the most similar to Pan image, other principal components may contain better spatial information. Hence, the authors in [77] proposed to replace the Pan image with the most similar component based on a correlation measure. PCA was also combined with multiresolution transform to improve the pansharpening process, where the wavelet transform was used in [88] and [89]; and the Contourlet transform was used in [77].

### 2.3.2 Relative Spectral Contribution category

This category uses the concept that the Pan image, at low resolution, is supposed to be equivalent to a linear combination of MS bands. This combination is related to the similarity between the spectral range spanned by the Pan and the MS bands. The spatial details of the Pan image are modulated into the MS images by multiplying each resampled MS band by the ratio of the corresponding Pan image to the sum of all the MS bands. Brovey [90], intensity modulation (IM) [35], and P + XS (CNES) [65] are pansharpening methods included in this category.

#### Brovey transform (BT)

The BT is named after its author. It is a simple image fusion method, based on the chromaticity transform that aims to keep the relative spectral contributions of each pixel [90] [91]. The BT can be used for only three bands [68]. Figure 2.5 (a) shows the pansharpened result obtained using the BT method when applied to the example of figure 2.4. The Brovey transform allows increasing the visual contrast in the image domain [92]. Authors in [54] used Landsat TM and SPOT Pan images to test some pansharpening methods. It was found that with the Brovey transform, much more emphasis is placed on the spatial information from SPOT Pan than on the spectral information from

TM. However, the spectral characteristics are seriously distorted. A solution, to better preserving spectral information, consists of subtracting the intensity of the MS image from the Pan image before applying the BT.

Brovey fused result P+XS fused result

Figure 2.5 Brovey and P+XS pansharpening examples using WorldView 2.

### Intensity modulation (IM)

Wong et al. [35] were the first to propose the intensity modulation model to merge Landsat MSS and Seasat SAR images. This concept has been adopted by Cliche et al. [93] for SPOT images to enhance each multispectral band separately with the panchromatic band. The analysis was based only on visual assessment of the results and is without any real physical context. Carper et al. [94] proposed a modified version with IHS combination to pansharpen the near infrared band. A combination of IM and IHS transform was also used in [95], where the intensity component of the IHS transformation is used instead of the sum of all the MS bands. The intensity component was obtained based on only three bands. Thus, a color distortion may occur, due to the difference between the spectral ranges of the Pan and MS images [96]. Moreover, in practical situation, there is no entire spectral overlap between Pan and MS bands, causing difficulties to approaches based on this concept.

### P+XS method (P+XS)

This special fusion method was proposed by the provider of the SPOT satellite imagery [65], under the assumption that the used Pan and MS images are acquired by the same instrument. The two identical instruments of SPOT allow simultaneous acquisition of images in both MS and Pan mode, which will guaranty the application of the method. The P+XS method is based on the correlation between MS and Pan images [97].

Authors, as in [68] and [67] studied the relationship between the relative spectral contribution and the component substitution categories; and found that they are closely related.

### 2.3.3 High-frequency injection category

In [98], the proposed method allowed transferring the high-frequency content of the higher-resolution image to the lower resolution image. Landsat MSS images were used, where lower resolution bands 1 and 4 (240m) were simulated then resampled to the original 80m spatial resolution and fused with the 80m band 2. The reconstructed image in each band was obtained by adding a high-pass version of the higher-resolution image (in this case band 2) to the lower-resolution multispectral image of that band. Even if the author worked on spatially compressed Landsat MSS data, he was the first to introduce the high-frequency injection idea in the pansharpening process. This idea was used in [99] to merge spectral information extracted from Landsat TM with spatial information extracted from panchromatic images having much higher spatial resolution. The author used a panchromatic photograph collected by the National High-Altitude Photography (NHAP) Program [99]. In another application, the author in [52] combined Landsat TM images with higher resolution SPOT panchromatic data for analyzing agricultural, urban, and geological sites in the Phoenix, Arizona region. In this case, the spatial information detail was extracted using a high-pass filter in order to "enhance the high-frequency/spatial information but, more important, suppress the low frequency/spectral information in the higher-resolution image" [52].

High-pass spatial details of an image can be obtained by subtracting a low-pass version from the original image. As the filter bandwidth increases, the low-pass version hides successively larger and larger structures, while the high-pass version picks up the smaller structures [1].

In general, this category is based on the fact of applying spatial filtering techniques to transfer the high-frequency content of the Pan image to the MS images [100]. The quality of the obtained results depends on the filter bandwidth. A good choice of this size, as recommended in [83], is approximately twice the size of the ratio of the spatial resolutions of the sensors. However, the ripple in the frequency response will have some negative impact [68]. Several variations of the spatial domain fusion have been proposed [100]. The pansharpened image can be obtained by directly summing each band of the MS images with the high-pass version of the Pan image, or applying a low-pass filtering to the MS images before doing the sum. Moreover, the tradeoff between the spatial and spectral information can be controlled using a gain factor [1]. Gaussian and Laplacian filters are some of the used filters. An example of a fused image using this kind of pansharpening technique is given in figure 2.6.

Recently, the authors in [101] proposed to utilize filters matching the modulation transfer function (MTF) of the different channels of the imaging instruments to extract the spectral and spatial information.

Extracted spatial information from Pan fused result

Figure 2.6 Pansharpening based on high-pass filtering.

Fusion methods based on high-pass filtering techniques are the basic principle of the ARSIS concept [55]. In such case, the spatial detail information is injected in a multiresolution framework. Moreover, this pansharpening family is widely considered as a very efficient solution to the fusion task and has demonstrated superior performance compared with many other pansharpening methods such as the methods in the Component substitution category, as stated in [102].

A global algorithm for the high-pass filtering based fusion methods can be accomplished according to the following steps [3]:

1. Upsample the MS image to the same size as the Pan image.

2. Calculate the high-frequency image by subtracting the low-pass filtered Pan from the original Pan.

3. Obtain the pansharpened image by adding the high-frequency image to each band of the MS image.

It should be noted that this pansharpening family is closely related to the multiresolution category, which will be discussed after introducing in next section the pansharpening methods using image statistics.

### 2.3.4 Methods based on the statistics of the image

The main feature of this category is that the statistical characteristics of the MS and Pan images are used in the pansharpening process. In [103], Price has proposed for the first time a pansharpening method based on the statistics of the image. This pansharpening technique is developed for combining dual resolution digital data, as from SPOT and the planned Thematic Mappers. It is essentially equivalent to the method discussed in [93], except that the analysis is based on statistical properties in the data, rather than on ad hoc approach which seeks an optimum image display. The main statistical properties used are the substantial redundancy of Landsat and SPOT data and the local correlation between the Pan and MS images. In this procedure, statistics were developed for an entire image, soon after, in [104] an improvement was made by developing the statistics locally, that is, for 3×3 arrays centered on each low-resolution pixel being analyzed. Price's method [104] relies on the statistical relationships between the radiances in the low and high spatial resolution bands. The relationship between the pixels of each pansharpened band y, the Pan image and the corresponding MS band was linearly modelled as:

$$y_{kl} - Y_{ij} = a_{ij} \cdot (x_{kl} - X_{ij}) \tag{2.2}$$

$Y_{ij}$ is the (i,j) pixel value for the low spatial resolution MS band, $x_{kl}$ is the (k,l) pixel value for the high spatial resolution Pan image, where k=m(i-1)+1, l=m(j-1)+1 and m is the ratio of the spatial resolution of Pan to MS images. $X_{ij}$ is the m by m average of the Pan image corresponding to the MS band at location (i,j).

Each value for $a_{ij}$ is obtained from the statistical relationship between low-resolution data values for a 3×3 array centered on the low-resolution pixel [104]. The main drawback of this algorithm is due to the use of blocks, where blocking artifacts can occur especially if the correlation between the Pan and MS images is small. Besides that, low-resolution radiometry is well preserved.

The work presented in [105] was inspired from the Price's method [104]. It is characterized by an adaptive insertion of information in accordance with the local correlation between the two images, allowing sharpening the MS images and reducing spectral distortion, simultaneously. Moreover, the number of the high-resolution images is not limited to one. In addition to those algorithms, the most of the developed works in this category are based on the Bayesian approach, such as [106], [107] and [108]. In this approach, the original high resolution MS image (z), resulting from pansharpening, is linked to the observed low resolution MS image (y) and the Pan image (x) the conditional probability distribution as:

$$p(z|y,x) = \frac{p((y,x)|z)p(z)}{p(y,x)} \tag{2.2}$$

Bayesian methods determine the posterior probability distribution p(z|y, x) by using Bayes law, based on the available prior knowledge p(z) about the expected characteristics of the fused image. p(y, x) is the joint probability distribution between x and y. Bayesian-based pansharpening methods differ mainly in the suitable assigning of prior and conditional distributions and the selection of an inference method.

In [106], p(z) is obtained from an interpolation operator and its covariance matrix. ]. In contrast, in [108] and [109], a non-informative prior distribution (i.e. constant distribution over the domain) is assumed, due to the nonexistence of a clear information on the high resolution MS image, no solution is preferred. Moreover, in [110], the prior knowledge about the smoothness of the object luminosity distribution within each band makes it possible to model the distribution of z using a simultaneous autoregressive model.

Models, as those presented in [111], [112], [113] [114] and [115], attempt to incorporate a smoothness constrain while preserving the edges in the image. However, they don't consider the correlations between the MS bands.

The conditional probability distribution of the observed low resolution MS image (y) and the Pan image (x), given the original high resolution MS image z, called the likelihood and denoted as p((y, x)|z), is usually defined as:

$$p((y,x)|z) = p(y|z)\,p(x|z) \tag{2.3}$$

by considering that the observed low resolution MS image and the Pan image are independent given the high resolution image. This allows an easier formulation of the degradation models.

Bayesian inference is performed, after defining the prior and conditional distributions, to estimate the high resolution MS image. Linear minimum mean square error (LMMSE) [116], maximum likelihood (ML) [108], maximum a posteriori (MAP) [109], the variational approach [111], [112] and simulated annealing [113] are some of the methods used to carry out the inference.

While the hypothesis of Gaussian additive noise for mathematical convenience is used, in practice, remote sensing imagery noise shows non-gaussian characteristics [117]. It is more convenient to use the Poisson noise, or a shaping filter [118] transforming a non-Gaussian noise into Gaussian.

In next section the multiresolution transform based category for pansharpening is considered.

### 2.3.5 Multiresolution category

Since the pioneering HPF technique [83], pansharpening based on injecting high-frequency components into MS data have demonstrated a superior performance [102]. Basically, spatial details derived from the Pan image are added to an upsampled version of the MS image. These details result from the difference between the Pan image and corresponding lowpass version, i.e.

average of the MS bands. Later efforts benefit from an underlying multiresolution analysis. The multiresolution decomposition provides an intermediate representation between transforms using local image information, such as convolution, and others using frequency content, such as the Fourier transform; and can assure good localization properties in both the spatial and Fourier domains. It allows to separately accessing to the spectral content of an image and the spatial information over a wide range of scales from local to global [1].

The multiresolution decomposition presents a simple hierarchical framework to fuse images with different spatial resolutions. Techniques such as Laplacian pyramids [119], wavelet transform [120], curvelet transform [121], ridgelet transform [122] and contourlet transform [61] are the most used multiscale decomposition techniques in multiresolution analysis. Most of these techniques have been used in pansharpening. The Pan and MS images are decomposed in different levels. The spatial information derived from Pan components is injected in finer scales of the MS images. Multiscale decomposition techniques highlight relationships between Pan and MS images in coarser scales and enhance spatial details [123]. A short explanation of the multiresolution methods and their applications in pansharpening process are given below.

### Laplacian pyramid

Multiresolution analysis based on the Laplacian Pyramid (LP) decomposition was originally developed by Burt and Adelson in [119] and inspired from the Gaussian pyramid (GP). In the GP, the original image is convolved with a Gaussian kernel, producing a low-pass filtered version of the original image. The difference between the original image and the low-pass filtered version represents the Laplacian. This process is continued to obtain a set of band-pass filtered images. The LP transform decomposes into disjoint band-pass channels the spatial frequency domain of an image [124]. Example of a two-level pyramid decomposition and reconstruction is shown in figure 2.7.

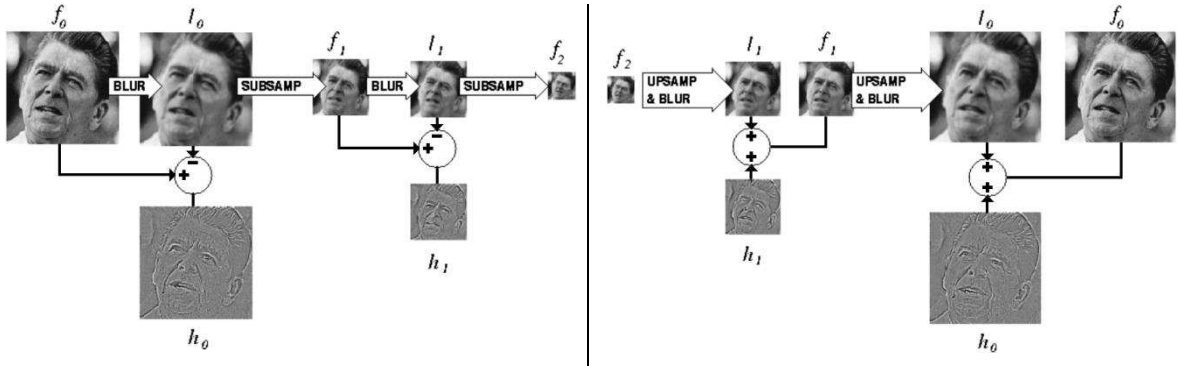


Decomposition Reconstruction

Figure 2.7 two-level Laplacian Pyramid[2]

[2] Source: http://sepwww.stanford.edu/~morgan/texturematch/paper_html/node3.html

In [125], the LP was extended to a more general scheme (GLP) allowing the use of a scale factor different from two. The modulation transfer function of the Pan image may be considered in the design of the Gaussian low-pass filter used for this image. This will improve the pansharpening results. The GLP-based pansharpening method can be accomplished in the following steps:

1. Upsample each MS band to the size of the Pan image.

2. Apply GLP on the Pan image

3. Fix the weighting parameters at each level, depending on the model used for details injection.

4. Sum the details from the GLP to each weighted MS band in order to obtain the pansharpened image.

This algorithm was used in [58] and [126] with different injection models. In [126], the authors described the use of two injection models embedded in "`a trous" wavelet transform analysis. The context-based decision model provided good results, however, a set of parameters must be chosen empirically. In addition, the optimal values of the parameters depend on the image content (vegetation, buildings). On the other hand, the spectral distortion minimizing the injection modelling is less sensitive to parameters tuning and can provide very good spectral and radiometric quality. The injection model described in [58], known as Ranchin-Wald-Mangolini model, models the MS details as a space and spectral-varying linear combination of the Pan image coefficients [3].

### Wavelet transform

A second well-known category of multiresolution pansharpening methods is the one based on wavelets. The basic idea of these methods is to inject the MS data on a decomposition level of the Pan images. This is achieved by addition, replacement or selection of the corresponding coefficients [59], [127]. The final synthesis of the fused coefficients provides an image that incorporates the spectral information of the MS bands and the spatial resolution of the Pan band.

The wavelet transform provides a hierarchical framework to decompose images. Moreover, it allows the separation of spatial details of the image between two successive levels [128].

An overview of image fusion techniques based on wavelet is given in [129].

In general, wavelet-based fusion schemes produced encouraging results, even if some artifacts in the fused image may occur when decimated algorithms are used [129]. Initially, the improvement of wavelet-based schemes was verified compared to standard schemes [127] and [130]. The discrete approach of the wavelet transform can be performed with different algorithms, Mallat's [53], [54], [54], [56] and the 'à trous' [66], [59], [60] are the most well-known ones for image pansharpening purposes. A detailed comparison of the application of these two algorithms in

pansharpening is given in [128]. It is found that "à trous" wavelets are more suitable for image fusion [129]. Later, the wavelet was associated with image transformations, like IHS and PCA, in hybrid scheme to improve the pansharpened results [131] and [128]. The wavelet transform was used to extract the detail information from Pan image, and the standard transformations were used in order to incorporate this information into the MS images.

Figure 2.8 shows the case of the additive wavelet fusion scheme, where the main steps are [129]:

1. Generate one Pan image for each MS band, histogram-matched to that band.

2. Apply the discrete wavelet transform (DWT) to both the MS and the new Pan images.

3. Add the detail images from the transformed Pan images to those of the transformed MS images. If multiple decompositions were applied, add the detail images at each resolution level.

4. Perform the inverse transform on the MS images with added Pan detail.

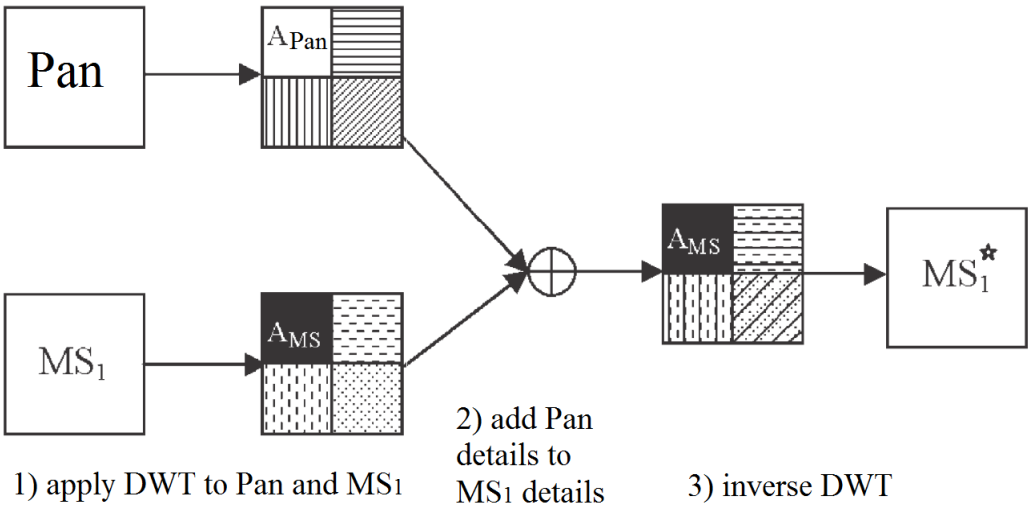


Figure 2.8 Fusion using a conventional DWT [129].

### Curvlet transform (CT)

Most of the wavelet-based image pansharpening methods preserve highly the MS spectral quality in the fused images; but fail in maintaining the Pan details compared with the conventional techniques such as: IHS, PCA and Brovey. Recently, a multiresolution analysis method, named the curvelet transform, was proposed in [121] for image denoising purposes. This transform is a non-separable multi-resolution analysis, whose basis functions are directional edges with progressive increasing resolution [133]. The curvelet transform represents edges better than wavelets; and since edges are crucial in representing an image, preserving edges will enhance details in the fused images. Thus, the use of the curvelet transform in fusing MS and Pan images will improve both the spatial and spectral qualities compared to the use of the wavelet transform.

In [132], the proposed method is based on embedding the curvelet transform in the wavelet fusion scheme. The combination of the two transforms allows enhancing both spatial and spectral information. The authors claim that the obtained pansharpened image has the same details as the original Pan image, due to the use of curvelet; and the same color as the original MS images, because of the wavelet use [132].

The experiments conducted in [133], on QuickBird images, show that the curvelet-based method outperforms quantitatively the state-of-the-art image pansharpening techniques, in terms of geometric, radiometric, and spectral fidelity. The pansharpening is based on the curvelet transform. The flowchart of this technique is summarized in figure 2.9. In this scheme, one Pan image and L spectral bands of an MS image are used. The enhancement of each band is synthesized from levels $S_1$ and $S_2$ of the curvelet transform of the Pan image. The inter band structure model (IBSM) [134], [66] establishes how the missing details information, to be injected into the resampled MS bands, are extracted from the Pan image. This model deals with the radiometric transformation (gain and offset) of spatial structures (edges and textures) when passing from Pan to MS images.

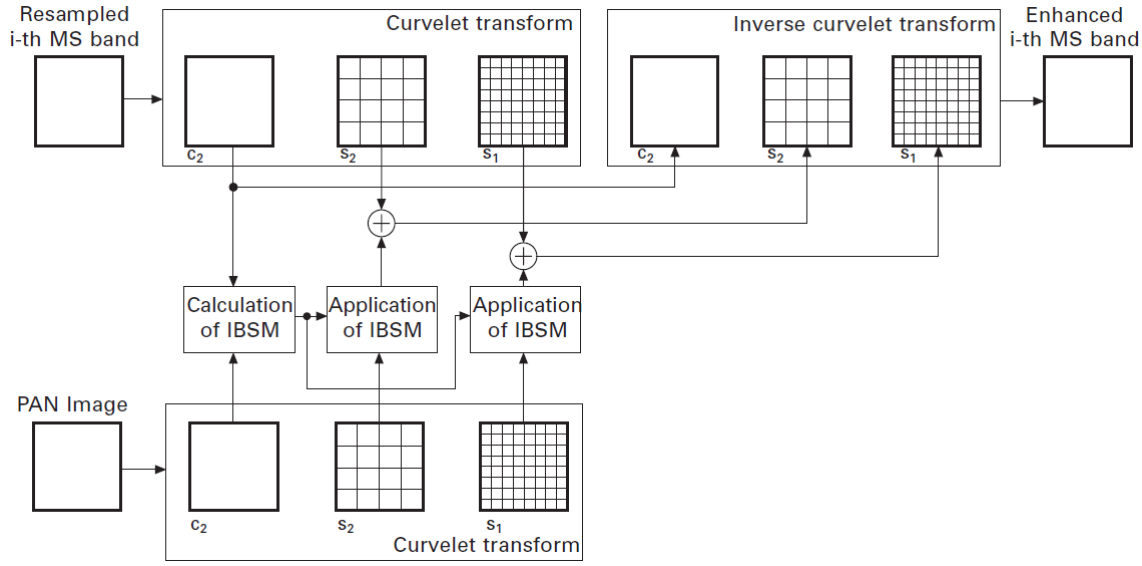


Figure 2.9 Flowchart of curvelet-based fusion of MS and Pan data with 1:4 scale ratio.

Details extracted from Pan by means of curvelet transform are added to the MS bands. The two sets of curvelet coefficients, one for each level, calculated from Pan are soft-thresholded to reduce the noise, weighted by the IBSM, and used to synthesize, by means of the inverse curvelet transform, two maps of zero-mean spatial edges and textures that are added to the corresponding detail frames of the ATWT of the resampled MS bands [133]. The pansharpened MS image is obtained by ATWT synthesis, i.e. by summing approximations and enhanced detail frames of each band.

### Contourlet transform

The contourlet transform has been proposed by Do and Vetterli in [135]. It is a new multi-scale, multi-direction framework of discrete images. It is so called due to its capacity to capture and to represent the contours. The contourlet, being a true 2-D transform, can capture intrinsic geometric structure information of images and achieve better expression than the discrete wavelet 2-D transform. The 2-D wavelet, which is obtained by a tensor-product of 1-D wavelet, is good for detecting the discontinuities at edge points; however it fails in detecting the smoothness along the contours [135]. In the contourlet transform, the multi-scale analysis and the multi-direction analysis are separated in two stages. The Laplacian pyramid (LP) [119] is first used to obtain the point of discontinuities and multiscale transformation, and then followed by directional filter banks (DFB) to group these coefficients for obtaining a smooth contour [77]. The overall result is an image decomposition using basic elements like contour segments. The framework of the contourlet transform is shown in figure 2.10 [136].

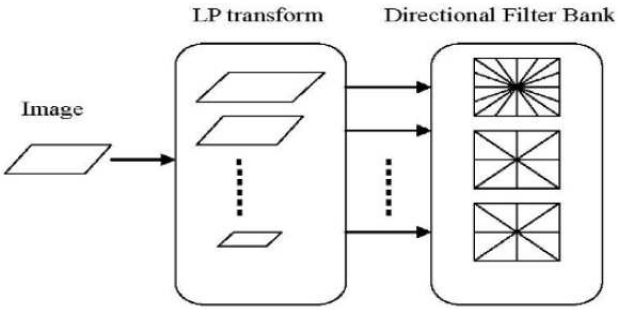


Figure 2.10 Framework of the contourlet transform.

Compared with traditional image decomposition transforms, contourlet can capture 2-D geometrical structure in natural images much more efficiently [136]. The contourlet transform satisfies the anisotropy principle and can capture intrinsic geometric structure information of images. Nevertheless, it lacks shift-invariance and results in ringing artifacts due to downsamplers and upsamplers present in both the LP and the DFB [61]. The shift-invariance is needed in edge detection, contour characterization and image fusion applications. In [61] the nonsubsampled contourlet transform (NSCT) is proposed. First, the nonsubsampled pyramid (NSP) is used to obtain a multi-scale decomposition by using two-channel nonsubsampled 2-D filter bands. Second, the nonsubsampled directional filter bank (NSFB) is used to split band-pass sub-bands in each scale into different directions. The NSCT have better frequency characteristics than contourlet [137]. The Contourlet and the NSCT transforms have been used in the image fusion domain. In [138] and [139], they were used to fuse optical and SAR imagery. and more specifically in pansharpening process. The algorithm is carried out using the three main steps:

1. Forward transform the Pan and MS images using the contourlet transform.

2. Apply a fusion rule onto the obtained coefficients.
3. Generate the pansharpened image by performing the inverse transform.

In [140], the authors demonstrated that the contourlet-based algorithm has better performance compared to known fusion algorithms based on wavelets and pyramid decompositions. They used the region-energy as a rule for the combination of the Pan and MS Contourlet coefficients. Their method was extended in [136] by considering the processing time. To speed up this method the authors in [136] proposed to directly replace all the details information of the MS image with that of Pan, or combine the IHS with contourlet. In [141], the authors combine IHS and NSCT in order to fuse QuickBird Pan and MS images of an urban area. NSCT has been also combined with PCA in [77] to improve the spectral quality of the pansharpened images. More studies, using the contourlet and NSCT, are currently developed for fusion purposes. They take into account the number of decomposition levels, the combination rules for the coefficients, the joint use of IHS, PCA or Brovey, …. Generally, the techniques used with wavelet are extended to the contourlet. In [142], the authors replace the MS detail bands coefficients with those of the Pan band. While in [143], the authors integrate statistics of images in multiresolution frame using the wavelet/ contourlet domain.

The authors in [63] extended the wavelet-based fusion method, presented in [144], to a use with NSCT instead of the wavelet transform. This method weights the contribution of the Pan image to each MS band, but it uses a different method to calculate these weights [63]. Pansharpened images using wavelet and contourlet-based methods are shown in figure 2.11. The pansharpened images appear similar. The use of IHS or PCA, conjointly with wavelet or contourlet, decreases the processing time. However, IHS introduces spectral distortions, while PCA produces spatial distortions, as shown in figure 2.11.

It was shown that the image fusion is a trade-off between the spectral and the spatial information, issued from an MS and Pan sensors, respectively [120], [54], [145]. However, as shown in [73], perfect pansharpening methods must generate results preserving both original spectral and spatial qualities of MS and Pan images, respectively. In general, multiresolution based pansharpening methods perform well [146].

Wavelet fused result NSCT fused result

Wavelet combined with IHS fused result NSCT combined with IHS fused result

Wavelet combined with PCA fused result NSCT combined with IHS fused result

Figure 2.11 Some pansharpening results based on multiresolution analysis.

## 2.4 Conclusion

This chapter provides an overview of the different methods proposed in the literature until now and classify them into different categories according to the main technique they use. Even if the classical component substitution and relative spectral contribution methods provide satisfying results for some applications; usually they introduce high spectral distortion [147]. Their results highly depend on the correlation between each spectral band and the Pan image. To improve the CS category, the MS image is transformed to imitate the Pan image. Generally, a linear combination of the MS image is utilized with some weighting parameters. These parameters are obtained either from the spectral response of the sensor or by minimizing the difference between the Pan image and this linear combination. This allows reducing the spectral distortion and enhancing color of the pansharpened images.

The local analysis of the images represents an important research area. It can improve methods based on the injection of structures in the pansharpened image. Moreover, in this category, the use of the MTF of the sensor as low-pass filter is recommended to reach good results.

The presented pansharpening methods, based on the statistics of the image, provide good results in general. Their major problem is the used models. In contrast, these methods allow incorporating the knowledge available about the MS image and the physics of the sensors (MTF, spectral response) and modelling the MS and Pan relationship.

The multiresolution analysis category provides the most successful pansharpening methods. Decomposing the images at different resolution levels and different directions allows injecting the details information, issued from the Pan image, into the MS image. From the presented methods, we conclude that the GLP and redundant shift-invariant contourlet transforms are the most popular multiresolution techniques applied to the fusion problem.

The quality of the resulting images, obtained by the discussed pansharpening method, is assessed qualitatively and quantitatively. In the next chapter, some of the most used techniques and quality evaluation indices are presented.

# 3

# Quality assessment

## 3.1 Introduction

The various pansharpening algorithms, discussed in chapter 2, aim to increase the spatial resolution of the MS images, using Pan image, while preserving their original spectral information. The spectral and spatial qualities of the resulting images are the objective of pansharpening. Visual analysis may be used to evaluate the pansharpened images. In practice, however, this subjective evaluation is time-consuming and expensive [148]. Thus, in addition to the visual analysis, quantitative evaluation must be considered [149]. Quantitative assessment is very important in remote sensing applications. The goal of this objective quality measure is to predict quickly perceived image quality. It tries to quantify the difference oriented toward an improvement in the image due to processing. Quantitative metrics exploit the pixel difference between images, correlation between images, and changes in histogram [150]. Quality refers to both the spatial and spectral quality of images, however, one can focus on the spatial fidelity while another targets the spectral fidelity [149]. Image quality metrics are mainly used to quantitatively measure the quality of an image that correlates with human perceived quality. They can be also used to compare pansharpening algorithms. These metrics should be accurate, and monotonic in predicting the quality of an image [150]. Nevertheless, as no reference images are available at high resolution, quantitative assessment is not an easy task [3].

Wald et al. [102] established the following three properties of the pansharpened images:

- Any pansharpened image once down-sampled to its original spatial resolution should be as identical as possible to the original image.

- Any pansharpened image should be as identical as possible to the image that a corresponding sensor would observe with the same high spatial resolution.
- The MS set of pansharpened images should be as identical as possible to the MS set of images that a corresponding sensor would observe with the same high spatial resolution.

Based on that, these properties have been reduced to two properties: consistency property, which is equivalent to the first property, and synthesis property, which combines the second and third properties [151]. Several protocols have been proposed, using these properties, to define an MS reference for comparison purposes.

Recently, a set of quality assessment algorithms have been proposed without the need of using a reference image. Those methods aim at providing reliable quality measures at full scale following Wald's protocol [3].

In this chapter, quality assessment is presented, where visual and quantitative analysis are discussed in sections 3.2 and 3.4, respectively. The quantitative indices are classified in spectral and spatial categories. In addition, the recent protocol of pansharpening quality assessment, established without using a reference image, is considered in section 3.3.

## 3.2 Visual analysis

The most consistent judgment of image quality evaluation is subjective, and conducted by human observers, and known as qualitative or visual analysis [152]. In the qualitative evaluation, the pansharpened images are compared to the original MS images in term of color, and to the original Pan images in term of spatial details [153]. This method depends on the observers experiences, which will introduce some uncertainty. Qualitative evaluation cannot be represented by accurate mathematical models [152]. However, in the quantitative evaluation, a set of metrics for assessing the spectral and the spatial qualities of the pansharpened images are used. Moreover, the display conditions of the images play an important role when visual evaluation is conducted. Consequently, a comparison of images quality will not provide efficient results, if it is conducted under different visualization conditions. The original MS image generally appears dark. Changing visualization conditions, by conducting for example a histogram stretching, allows more reliable display of this image. These different appearances are not issued from the quality difference, but just by the conditions of the image display. Therefore, one cannot conclude that one image is better than another if the display condition is not the same [153].

Qualitative analysis is a necessity to verify if the objective of pansharpening has been met.

- In addition to the spatial details and the local contrast, the visual assessment targets the global image quality as the geometric shape and size of objects. Moreover, several visual quality parameters for testing the properties are [154]:

- Spectral preservation of features in each MS band: based on the appearance. The appearance of the objects in the pansharpened images is analyzed in each band based on the appearance of the same objects in the original MS images.
- Multispectral synthesis in fused images: pansharpening should preserve the original spectral characteristics of objects. The multispectral characteristics of objects of the pansharpened images should be similar to those in the original MS images. This propriety may be verified by analyzing different color composites of the pansharpened images and comparing them with those of original MS images.
- Synthesis of images close to actual images at high resolution as defined by the synthesis property of fused images. This property cannot be directly verified but can be analysed from our knowledge of spectra of objects in the lower spatial resolutions.

Because visual approach may contain a subjective factor and may be influenced by personal preference [153], a quantitative evaluation, fusing the individual assessment, is usually required to validate the visual assessment.

## 3.3 Quality assessment without a reference

Quantitative evaluation of pansharpening algorithms is an efficient method to assess the quality of the resulting images. This evaluation is possible when an image reference is available. In pansharpening, image reference is obtained using the assumption of invariance of fusion performances to scale changes [102]. Therefore, when an algorithm performs well on spatially down-sampled data, it will be efficient when the data are considered at higher spatial resolution. Consequently, the image reference is generated by down-sampling the available images to a coarser resolution before performing pansharpening. Authors in [155] proclaimed that the assumption is invalid for very high resolution images, particularly in urban environment, except if low-pass filters, matching the modulation transfer functions (MTF) of the sensor, are used for the spatial degradation of images. Thus, they proposed a global index capable to assess pansharpened images and to work at the full scale without performing spatial degradation on the images. This approach, allowing evaluation of fusion quality without requiring reference images, is known as "quality with no reference" (QNR). It is based on the universal quality index Q proposed in [156], and includes two indices, one for spectral distortion ($D_\lambda$) and the other for spatial distortion ($D_S$).

### 3.3.1 The universal quality index (Q)

The Q index measures the local correlation, luminance, and contrast between two images. For two images *x* and *y*, it is calculated as follows:

$$Q(x,y) = \frac{4 \cdot \sigma_{xy} \cdot \bar{x} \cdot \bar{y}}{[\sigma_x^2 + \sigma_y^2] \cdot [(\bar{x})^2 + (\bar{y})^2]} \tag{3.1}$$

Where $\sigma_{xy}$ is the covariance between x and *y*, and $\sigma_x^2$ and $\sigma_y^2$ are the variances of *x* and *y*, respectively. $\bar{x}$ and $\bar{y}$ are the means of x and y, respectively. Equation (3.1) can be rewritten as the combination of three factors as:

$$Q = \frac{\sigma_{xy}}{\sigma_x \cdot \sigma_y} \cdot \frac{2 \cdot \bar{x} \cdot \bar{y}}{[(\bar{x})^2 + (\bar{y})^2]} \cdot \frac{2 \cdot \sigma_x \cdot \sigma_y}{[\sigma_x^2 + \sigma_y^2]} \tag{3.2}$$

The three factors measure the correlation, similarity in luminance and similarity in contrast, respectively. The Q index dynamic range is [-1 to 1] and the value Q = 1 is achieved if x = y for all pixels. The computation of Q is done using a sliding window of size N×N in order to increase the differentiation capability and measures the local distortion. Then the Q index is averaged over all the local indices to calculate the global value.

In the QNR approach, it is assumed that the inter bands spectral quality of the pansharpened images is unchanged after the fusion process. When Q is closer to 1, the pansharpened images are similar to the original ones.

### 3.3.2 The spectral distortion $D_\lambda$

Based on the Q index, the spectral distortion $D_\lambda$ index is derived without a reference image. Two sets of inter-band Q values are calculated separately at low and high resolutions. The differences of the corresponding Q values at the two scales yield the spectral distortion introduced by the pansharpening process. Thus, the spectral distortion can be represented mathematically as

$$D_\lambda = \sqrt[p]{\frac{1}{L(L-1)} \sum_{l=1}^{L} \sum_{r=1(r \neq l)}^{L} \left| Q(\hat{G}_l, \hat{G}_r) - Q(\tilde{G}_l, \tilde{G}_r) \right|^p} \tag{3.3}$$

Where L is the total number of bands, $\hat{G}$ represents the original MS band and $\tilde{G}$ is the pansharpened MS band. The positive integer exponent p is chosen to emphasize large spectral differences: for p=1, all differences are equally weighted; as p increases, large components are given more relevance [155].

### 3.3.3 The spatial distortion $D_S$

The second index $D_S$ concerns the spatial distortion. It is determined by calculating the Q index between each MS band and the Pan image at low and high resolutions. The difference between the two values provides the spatial distortion. The spatial distortion index is given by:

$$D_s = \sqrt[q]{\frac{1}{L} \sum_{l=1}^{L} \left| Q(\hat{G}_l, \hat{P}) - Q(\tilde{G}_l, P) \right|^q} \tag{3.4}$$

where P represents the Pan image, and $\hat{P}$ is a spatially degraded version of the Pan image, generated by low-pass filtering followed by decimation.

Analogously, $D_s$ is proportional to the q-norm of the difference vector, where q may be chosen so as to emphasize higher difference values.

### 3.3.4 QNR

The indices $D_\lambda$ and $D_S$ reach their minimum (equal to zero), when the two images are identical and they are upper bounded by one if clipping below zero of Q values is enabled. Their combination, carried out as the product of the one's complements of $D_\lambda$ and $D_S$, produces the QNR index.

$$QNR = (1 - D_\lambda)^\alpha \cdot (1 - D_s)^\beta \tag{3.5}$$

The two exponents jointly determine the non-linearity of response in the interval [0, 1] to achieve a better discrimination of the compared pansharpened images [155].

Another QNR method was proposed in [157]. It is based on the measure of the mutual information (MI) between different images instead of the Q index. The mutual information between upsampled original and fused MS bands is used to assess the spectral quality, while the mutual information between the Pan image and the fused bands measures the spatial quality.

Recently, in [101] another protocol was proposed for evaluating spectral and spatial quality of pansharpened images. A Flowchart of the spectral quality evaluation procedure is given in figure 3.1. To assess the spectral quality, the MTF of each spectral channel is used to low-pass filter the pansharpened image. After the decimation process, a comparison is accomplished with original low-resolution MS images using the Q4 index [158].

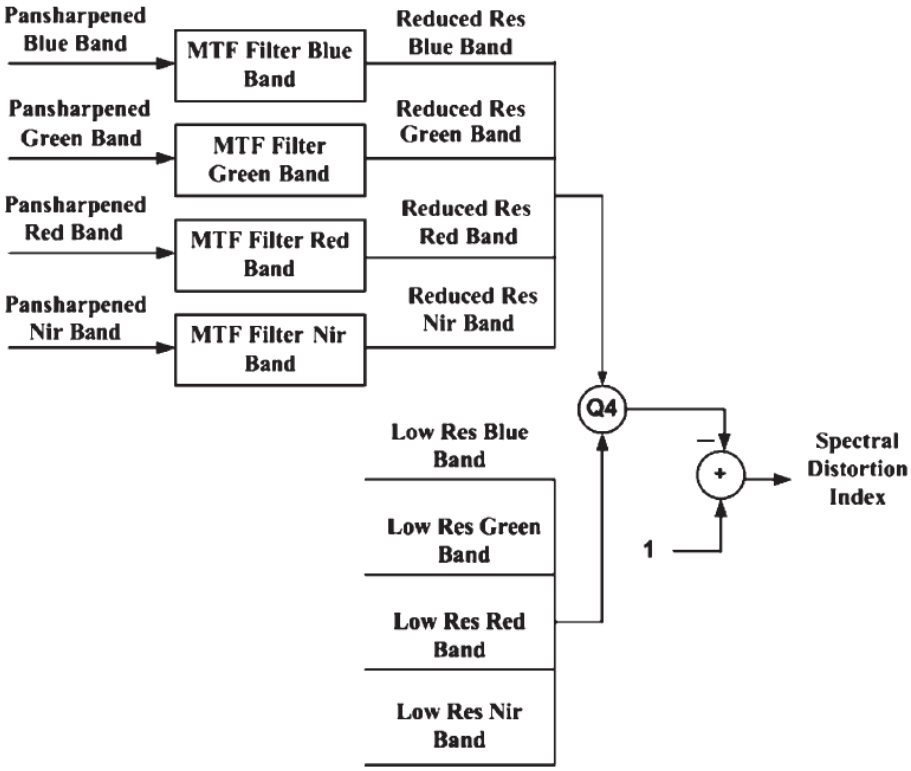


Figure 3.1 Flowchart of spectral quality assessment [101]

Note that the MTF filters for each sensor are different and the exact filter response is not usually provided by the instrument manufacturers.

On the other hand, the spatial quality assessment procedure is shown in figure 3.2. The high-pass complement of the MTF filters is used to extract the high-frequency information from the MS images at both high (fused) and low (original) resolutions. Moreover, the Pan image is down-sampled to the same spatial resolution of the original MS image, and high-frequency information is extracted from high- and low-resolution Pan images. The Q index of [156] is calculated between the details of each MS band and the details of the Pan image at the two resolutions. The average of the absolute differences in the Q index values across scale of each band produces the spatial index.

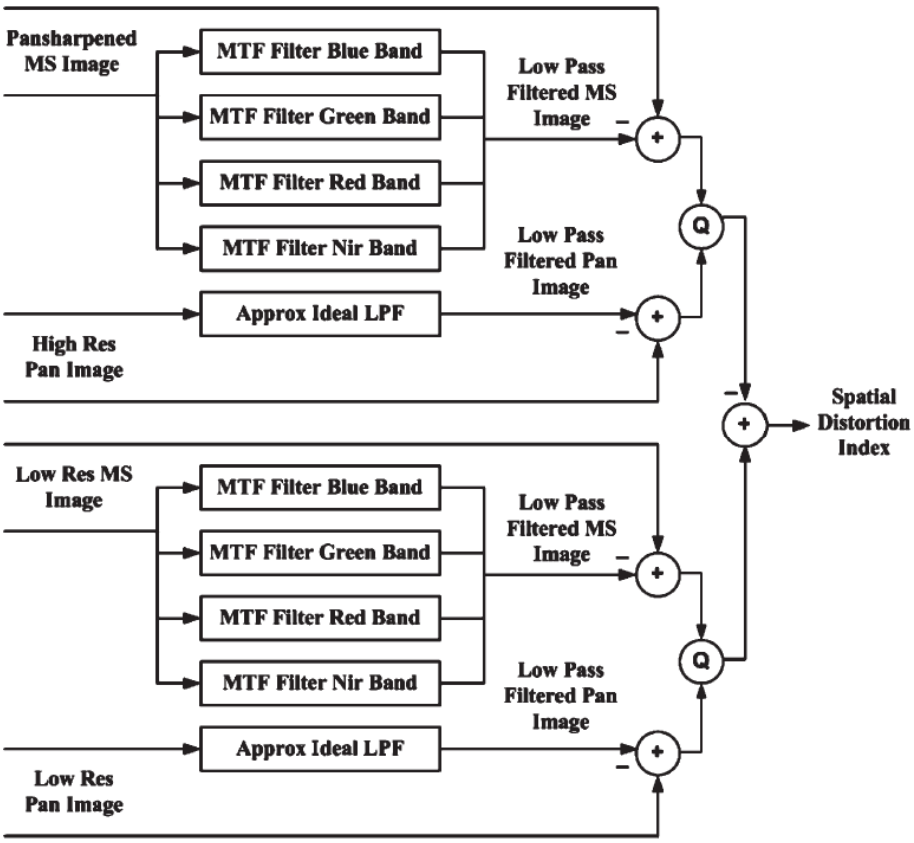


Figure 3.2 Flowchart of spatial quality assessment [101]

It is to note that the QNR approach is not widely used in quality assessment since its introduction. We think that the quantitative analysis still be the mostly used approach, based on the properties of Wald, to assess pansharpened images.

## 3.4 Quantitative analysis with a reference

A set of metrics have been proposed to quantitatively evaluate the spectral and spatial quality of the images. The quality assessment of pansharpened MS images is a difficult task. Even when reference MS images are available for comparisons with fusion results, the assessment of fidelity to the reference usually requires computation of a number of different indexes. Suppose that the

spatial resolution of original MS images is *l* and the Pan one is *h*. Generally, the original MS images are considered as reference. The fusion process is conducted on degraded versions of the MS and Pan images. The degraded Pan and MS images are obtained by down-sampling them by a factor of (*l*/*h*) [131]. For the Ikonos or QuickBird cases, this factor is 4. The fused MS images are compared to those original MS images using the quantitative assessment. In this section, we will present the more usually used indexes in two categories: spectral and spatial assessment.

## 3.4.1 Spectral quality assessment

To measure the spectral distortion due to the pansharpening process, each fused image is compared to the reference MS image, using one or more of the following quantitative indexes:

### 3.4.1.1 Band to band measuring indexes

1) Bias, variance (VAR) and the standard deviation (SD): the bias is the difference between the mean of the original image and that of the fused one. In the relative value, the bias is divided by the mean of the original image. The relative variance is the difference in variance between the original and the fused images, divided by the variance of the original image. The ideal value for each of these measures is zero. The standard deviation of the difference image in relation to the mean of the original image indicates the level of the error at any pixel. The lower the value of SD, the better the spectral quality of the fused image.

2) Spectral Angle Mapper (SAM): SAM denotes the absolute value of the angle between two vectors, whose elements are the values of the pixels of different bands of the pansharpened and the MS images. A SAM value equal to zero denotes the absence of spectral distortion, but radiometric distortion may be present (the two pixel vectors are parallel but have different lengths). SAM has been widely used in multispectral and hyperspectral image analysis to measure spectral similarity between substance signatures for material identification. To compute a SAM value between two images, each having L bands B, two spectral vectors v and w are constructed, both having L components, where $v = \{v_1, v_2, \ldots, v_L\}$ with $v_k = B(k)(i, j)$ corresponding to pixel (i,j) in the $k^{th}$ original band, while $w = \{w_1, w_2, \ldots, w_L\}$ with $w_k = Fused\_B(k)(i, j)$ corresponding to pixel (i,j) in the $k^{th}$ fused band. SAM takes the arccosine of the dot product between two spectral vectors:

$SAM(v,w) = \cos^{-1}\left(\frac{\langle v,w\rangle}{\|\vec{v}\|\cdot\|\vec{w}\|}\right)$, which can be written as [159]:

$$SAM(v,w) = \cos^{-1}\left(\frac{\sum_{i=1}^{L} v_i w_i}{\sqrt{\sum_{i=1}^{L} v_i^2}\sqrt{\sum_{i=1}^{L} w_i^2}}\right) \tag{3.6}$$

SAM is measured either in degrees or in radians and is usually averaged over the whole image to yield a global measure of spectral distortion [160]. Small angles indicate high similarity and high angles indicate low similarity.

3) Relative-shift mean (RM): The RM [150] of each band of the pansharpened image helps to assess the change in the histogram of the pansharpened image and is defined as the percentage of variation between the mean of the reference image and the pansharpened image:

$$RM = \frac{|outputmean - originalmean|}{originalmean}\% \tag{3.7}$$

A RM value of 0 signifies that the two images are greatly similar.

4) Correlation coefficient (CC): the CC between each band of the reference and the pansharpened image indicates the spectral integrity of the pansharpened image [92]. However, CC is insensitive to a constant gain and bias between two images and does not allow for subtle discrimination of possible pansharpening artifacts [68]. CC is the most popular quantitative index. It shows the similarity in small size structures between the fused and original pixels. It is defined as:

$$CC(x,y) = \frac{\sum_{i=1}^{M}\sum_{j=1}^{N}(x_{i,j} - \bar{x})(y_{i,j} - \bar{y})}{\sqrt{\sum_{i=1}^{M}\sum_{j=1}^{N}(x_{i,j} - \bar{x})^2 \sum_{i=1}^{M}\sum_{j=1}^{N}(y_{i,j} - \bar{y})^2}} \tag{3.8}$$

Where (MxN) is the size of the images and $\bar{x}$ and $\bar{y}$ stand for the mean values of the two images x and y between which the correlation is computed and CC is calculated globally for the entire image. A CC value of +1 indicates that the two images are highly correlated [161].

5) Root mean square error (RMSE): the RMSE between each band of the reference and the pansharpened image measures the changes in radiance of the pixel values [102]. RMSE is a very good indicator of the spectral quality when it is considered along homogeneous regions in the image [150]. RMSE should be as close to 0 as possible.

RMSE, between a reference image x and a fused image y with a MxN size, is defined by [162]:

$$RMSE = \sqrt{\frac{\sum_{i=1}^{M}\sum_{j=1}^{N}\left(x_{i,j} - y_{i,j}\right)^2}{M \times N}} \tag{3.9}$$

6) Structure Similarity Index (SSIM): after the proposition of the Universal Image Quality Index Q, given in equation (3.2), Wang proposed in [148] an improved version of Q named Structure Similarity Index (SSIM), where the Q index is a particular case for SSIM index for $C_1=C_2=0$.

$$SSIM(x,y) = \frac{(2 \cdot \bar{x} \cdot \bar{y} + C_1)(2 \cdot \sigma_{xy} + C_2)}{((\bar{x})^2 + (\bar{y})^2 + C_1)(\sigma_x^2 + \sigma_y^2 + C_2)} \tag{3.10}$$

Where $C_1=(k_1L)^2$ and $C_2=(k_2L)^2$ are two variables to stabilize the division with weak denominator; and L represents the dynamic range of the pixel values. The commun values for $k_1$ and $k_2$ are 0.01 and 0.03, respectively [148]. SSIM is a perceptual measure that combines several factors related to the way humans perceive the quality of the images. Beside luminosity and contrast distortions, the structure distortion is considered in SSIM index and calculated locally in 8 × 8 square windows. The value varies between -1 and 1. Values close to 1 show the highest similarity with the original images.

### 3.4.1.2 Global measuring indexes

While previous indexes only evaluate the difference in spectral information between each band of the fused and the reference image, in order to estimate the global spectral quality of the pansharpened images, the following indices are used:

1) The index of the relative average spectral error (RASE) : this index, expressed as a percentage, characterizes the average performance of the method of image fusion in the spectral bands considered

$$RASE = \frac{100}{M}\sqrt{\frac{1}{L}\sum_{i=1}^{L} RMSE^2(B_i)} \tag{3.11}$$

Where M is the mean radiance of the L spectral bands ($B_i$). The lower the value of RASE, the higher the similarity of the fused and original image.

2) “Erreur relative globale adimensionnelle de synthése” (ERGAS) for which the English translation is relative dimensionless global error in fusion [130], is a global quality index sensitive to mean shifting and dynamic range change [149]. The lower the ERGAS value, especially a value lower than the number of bands, the higher the similarity between original and fused images. ERGAS is as follows:

$$ERGAS = 100\frac{h}{l}\sqrt{\frac{1}{L}\sum_{i=1}^{L}\frac{RMSE^2(B_i)}{\mu_i^2}} \tag{3.12}$$

Where h is the resolution of the high spatial resolution image, l is the resolution of the low spatial resolution image, $\mu_i$ is the mean radiance of each spectral band $B_i$ and L is the number of the bands involved in the fusion. The lower the value of ERGAS, the higher the spectral quality of the fused image.

3) Mean SSIM (MSSIM) and Average Quality (Qavg): These indices [148], [144] are used to evaluate the overall image SSIM and Q indexes quality, by averaging these measures. The higher, closer to one, the value, the higher the spectral and radiometric quality of the merged images.

4) Another global measure, Q4, proposed in [158] depends on the individual Q index of each band, but also on spectral distortion, embodied by the spectral angle SAM. The problem of this index is that it cannot be extended to images with a number of bands greater than four.

Let a, b, c and d denote the radiance values of a given image pixel in the four bands, typically acquired in the B, G, R, and NIR bands. Q4 is defined by:

$$Q4 = \frac{\left|\sigma_{z_1 z_1}\right|}{\sigma_{z_1}\sigma_{z_2}} \times \frac{2\left|\overline{z_1}\right|\left|\overline{z_2}\right|}{\left|\overline{z_1}\right|^2 + \left|\overline{z_2}\right|^2} \times \frac{2\sigma_{z_1}\sigma_{z_2}}{\sigma_{z_1}^2 + \sigma_{z_2}^2} \tag{3.13}$$

Where $z_1 = a_1 + ib_1 + jc_1 + kd_1$ and $z_2 = a_2 + ib_2 + jc_2 + kd_2$

Q4 achieves the maximum value of 1 when two images are identical. Thus, the higher the quality of the image, the higher the metric Q4. The first term, which is the modulus of the hypercomplex CC between $z_1$ and $z_2$, is sensitive to both the loss of correlation and the spectral distortion between the two MS datasets. The second term measures simultaneously the mean bias on all bands, and the third term measures the changes in the contrast.

All of the expectations were calculated as averages on $N \times N$ blocks. Hence, Q4 also depends on N and is denoted as Q4N. Eventually, Q4N is averaged over the entire image to yield the global score index. Because all the fusion methods yielded rather steady plots for N>16 in [158], Q4 with N=32 was calculated and averaged on the entire image.

## 3.4.2 Spatial Quality Assessment

To assess the spatial quality of a pansharpened image, its spatial detailed information must be compared to that of in the reference high resolution MS image. Just a few quantitative metrics have been found in the literature to evaluate the spatial quality of fused images. Zhou [54] proposed the following procedure to estimate the spatial quality of the fused images: to compare the spatial information present in each band of these images with the spatial information present in the Pan image.

To evaluate similarities between spatial details, a high-pass filter is applied to the images and then the CC between the resulting images is computed. This quantity is also called spatial correlation coefficient sCC. The authors in both [54] and [144] used the high-pass filter given by:

$$F = \begin{bmatrix} -1 & -1 & -1 \\ -1 & 8 & -1 \\ -1 & -1 & -1 \end{bmatrix} \tag{3.14}$$

While in [54] the fused bands are compared with the Pan image, in [144] these fused ones are compared with the original MS images. However, the use of the Pan image as a reference is incorrect as demonstrated in [73], [163], and the high resolution MS image has to be used, as done by Otazu et al. in [144]. The high correlation coefficients between the fused filtered image and the reference filtered one (sCC) indicate that most of the spatial information of the reference image was incorporated during the fusing process. The sCC has the same definition as the CC. The ideal value is 1.

Recently, a new spatial quality metric was proposed in [164], related to the quantitative edge analysis. The authors state that a good pansharpening method should preserve all the edges present in the Pan image in the sharpened image [164]. Therefore, a Sobel edge operator is applied on the image in order to detect its edges which are then compared with the edges of the Pan image.

Additionally, some spectral quality measures have been adapted to the spatial quality assessment. Pradhan et al. [164] suggested the use of structural information in the SSIM measure between Pan and pansharpened images as a spatial quality measure. Lillo-Saavedra et al. [165] proposed to use the spatial ERGAS index that includes in its definition the spatial RMSE calculated between each fused spectral band and the image obtained by adjusting the histogram of the original Pan image to the histogram of the corresponding band of the fused MS image.

## 3.5 Conclusion

In this chapter, pansharpening quality assessment is considered. The quantitative approach, with or without a reference, in addition to the visual approach may be used to conduct an accurate assessment.

However, the visual evaluation of pansharpened images is time-consuming and expensive. Moreover, the quantitative quality assessment without a reference, recently proposed, has not yet proved to be efficient. Therefore and in our opinion, a good solution to assess pansharpening products is to focus, mainly, on the use of quantitative tools. Nevertheless, care must be taken in the choice of the used indices. The spectral as well as the spatial quality must be considered. Indices give a way to rank different algorithms and give an idea of their performance. Recent advances in full-scale quality measures set the trend for new measures.

# Part B

***Contributions in***

***Improving Pansharpening,***

***Vegetation extraction***

***and***

***Quality assessment***

# 4

# Contributions in improving pansharpening and vegetation extraction

## 4.1 Introduction

Earth observation satellites provide multispectral and panchromatic data having different spatial, spectral, temporal, and radiometric resolutions. The fusion of a panchromatic (Pan) image having high spatial but low spectral resolutions with multispectral (MS) images having low spatial but high spectral resolutions is a key issue in many remote sensing applications that require both high spatial and high spectral resolutions. The fused image may provide feature enhancement, and classification accuracy increase. The design of a sensor to provide both resolution requirements is limited by the tradeoff between spectral resolution, spatial resolution, and signal-to-noise ratio of the sensor. The spectral and spatial resolutions have an inverse relationship. Thus, a high spectral resolution results in a low spatial one and vice versa [77]. Hence, there is an increasing use of image processing techniques to fuse the available multispectral images and Pan images with the objective to obtain the highest resolutions spatially and spectrally. These image processing techniques are known as pansharpening or resolution fusion techniques. Pansharpening has been an active area of research for more than a decade, and many image fusion techniques and software tools have been developed for specific applications [55], [67], [72], [76], [77], [78], [85], [86], [90], [129], [131], [144], [145], [166], [167] and [168].

In this chapter, we present our main contributions in the fields of pansharpening and vegetation extraction. For a better readability, the chapter is divided into three main parts. In the first part, two pansharpening methods based on the IHS transform are presented. The second part is devoted to presenting the NSCT-based pansharpening method. In the third part, a vegetation extraction technique is considered, and at the end, a chapter conclusion is given.

It is to note that the pansharpening, conducted in part one, uses the vegetation enhancement to improve the resulting images quality. In this context, a new vegetation index for high resolution images, where the Pan image was introduced in the vegetation detection process, is defined. The method of vegetation from Ikonos imagery, being presented in the third part, is essentially based on this index.

The proposed algorithm based on the NSCT, presented in part 2, is tested in the context of the participation to the 2012 IEEE GRSS Data Fusion Contest: Multimodal/multi-temporal fusion.

Before, the presentation of the proposed methods, it is essential to mention that we have studied the impact of the interpolation on the pansharpened images in [169], where the classical bicubic interpolation, usually used in pansharpening, is compared to a more efficient existing interpolation given in [170]. It was shown that using an efficient interpolation algorithm can improve the pansharpened images [169] (see Appendix A).

# 4.2 Part1:

# Proposed IHS-based pansharpening methods

In practical applications, the IHS-based fusion is the most widely used [131]. This technique is suitable when exactly three MS bands are concerned. When more than three bands are available, a good solution is to use all the MS bands located within the Pan band, especially the Near Infra Red (NIR) band. In this context, the authors in [72] defined a fast IHS (FIHS) transform for three bands and a generalized IHS (GIHS) transform for four bands by including the NIR band in the computation of the intensity component (*I*). Besides its fast computing capability for fusing images, this method can extend traditional three-order transformations to an arbitrary order. It can also quickly fuse massive volumes of data, with different resolutions, by requiring only resampled MS data. That is, it is well suitable in terms of processing speed for fusing Ikonos images. However, GIHS fusion also distorts color in the same way as the traditional IHS fusion technique. Various methods, like those presented in [145], [90] and the spectral adjusted IHS developed in [72], were proposed in order to improve the fusion based on the IHS transform. These methods make use of the spectral characteristics of sensors in the fusion process, i.e. the *I* component is obtained by weighting the MS bands according to their spectral responses. Moreover, for vegetation visualization applications, recent methods make use of vegetation enhancement to improve color quality [85], [86], [78]. This enhancement is applied in the vegetation areas, which are delimited using a vegetation index.

Our contributions in this context consist in using IHS and boosting the G band in the vegetated area. Two methods are proposed. In the first one [85] and [173], the vegetation is detected by the NDVI and the boosting is done before the fusion process. In contrast, for the second method [171], the boosting is done after the fusion process and the vegetation is delineated using a new index proposed for high resolution images [172] and defined in equation (4.25).

## 4.2.1 Problem positioning

To date, various image fusion methods have been proposed in the literature [72], [129], [131], [134], [145], [160], and [174]. In the context of Spot sensor, the Pan image is obtained only in the visible part of the electromagnetic spectrum. Therefore the I component produced by combining R, G and B bands appears like the Pan image. Traditionally, the IHS-based pansharpening consists of:

- Using R, G and B bands to compute the IHS components.

- Replacing the I component by the Pan image, then reversely transforming the Pan, H and S components from the IHS space into the RGB space, resulting in a fused color image [131].

If the I component has high correlation with the Pan image being fused, this will produce a satisfactory fusion result.

However, in the context of Ikonos or QuickBird, the Pan image is produced in a larger spectral band: from the visible to NIR. Therefore, the I component obtained from combining R, G and B, often differs from the Pan image. Hence, the color distortion becomes a common problem of the IHS technique for Ikonos and QuickBird imagery. In [72], Tu et al. presented a simple spectral-adjusted scheme integrated into a fast IHS method to reduce spectral distortion. In [145] Choi used a trade-off parameter in another approach for image fusion based on fast IHS fusion.

### 4.2.2 Method 1:

Based on the fact that the grey values of Pan in the green vegetated regions are far larger than the grey values of intensity (I), we propose to adjust spatially the I image, in the vegetated area only, in order to get grey values in the same range as those of the Pan image. For this purpose we use the Normalized Difference Vegetation Index (NDVI) to identify the vegetation area in which the green (G) band by using the red (R) and the NIR bands. This will minimize color distortion arising from the spectral mismatch between the Pan and MS bands. In this approach, we propose to enhance the vegetation area in the green band using a proportion b of the difference between the NIR and Red bands. We then use the conventional IHS method to fuse the MS and Pan bands. The enhancement is accomplished only for the region where the NDVI is superior to a preset positive value a. We have tested a large number of images to select the value of the proportion b. In our experiments, for Ikonos a value of 0.4 for b gave best results in terms of fused image quality. For QuickBird the best fused results were achieved with b=0.2. For a, we have used a value of 0.1 for both Ikonos and QuickBird images.

Figure 4.1 shows the proposed method described by the following steps:

1. Given the NIR and the R bands, calculate the NDVI index by using (4.1)

$$NDVI = \frac{NIR - R}{NIR + R} \tag{4.1}$$

2. For any pixel (i,j) compute the enhanced green band ($G_{Boosted}$) using (4.2) :

$$G_{Boosted}(i,j) = \begin{cases} G(i,j) + b \cdot (NIR(i,j) - R(i,j)) & if\ NDVI(i,j) > a \\ G(i,j) & otherwise \end{cases} \tag{4.2}$$

3. The IHS transform is then applied on the R, B and $G_{Boosted}$.

4. The enhanced H and S are used with the Pan to get the enhanced multispectral RGB image ($MS^*_{RGB}$), by use of the inverse IHS transform. We then subtract the amount added in (4.2), only for the enhanced pixels, from the green band.

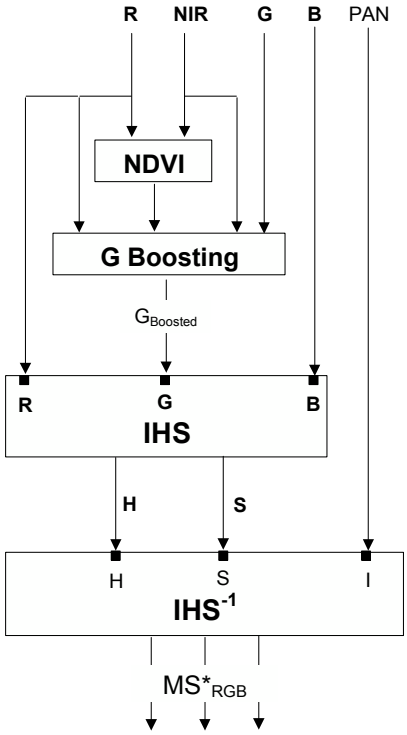


Figure 4.1 Proposed fusion technique.

### 4.2.2.1 Experimental results

To evaluate the proposed fusion procedure with examples, two data were used for this experiment. The first one is an image scene on Mt. Wellington, Tasmania, Australia, taken by the Ikonos satellite sensor on January 2005. The image size is approximately 10000×10000 pixels. The second one is an image scene on the *Kokilai Lagoon*, a Marine Protected Area in *Sri Lanka,* taken by the QuickBird satellite sensor on April 2005. The image size is approximately 2600×3200 pixels. Before the image fusion, the multispectral images were co-registered to the corresponding panchromatic images and resampled to the same pixel sizes of the panchromatic images. Two small areas in these images are shown; the first one is mostly vegetation and the second one contains less vegetation. Their Pan images are shown in Figure 4.2(a) and Figure 4.3 (a), and the original RGB images in Figure 4.2(f) and Figure 4.3(f), respectively.

For comparison purposes, three other IHS fusion methods have been tested. The first one is the classical IHS (Classic). The second method (Tu), described in [72], is given in (4.3).

$$\begin{bmatrix} F(R) \\ F(G) \\ F(B) \end{bmatrix} = \begin{bmatrix} R + Pan - I_{sa} \\ G + Pan - I_{sa} \\ B + Pan - I_{sa} \end{bmatrix} \tag{4.3}$$

Where $I_{sa} = (R + 0.75 \cdot G + 0.25 \cdot B + NIR)/4$

The third method (Choi) is given in [145] by the following formula (4.4):

$$\begin{bmatrix} F(R) \\ F(G) \\ F(B) \end{bmatrix} = \begin{bmatrix} Pan - \frac{(Pan - I_4)}{4} + (R - I_4) \\ Pan - \frac{(Pan - I_4)}{4} + (G - I_4) \\ Pan - \frac{(Pan - I_4)}{4} + (B - I_4) \end{bmatrix} \tag{4.4}$$

where $I_4 = (R + G + B + NIR)/4$

**Visual analysis**

As shown for the test site in Figure 4.2, most of the area is covered by green vegetation. The fusion results are shown in Figure 4.2 (b-e).

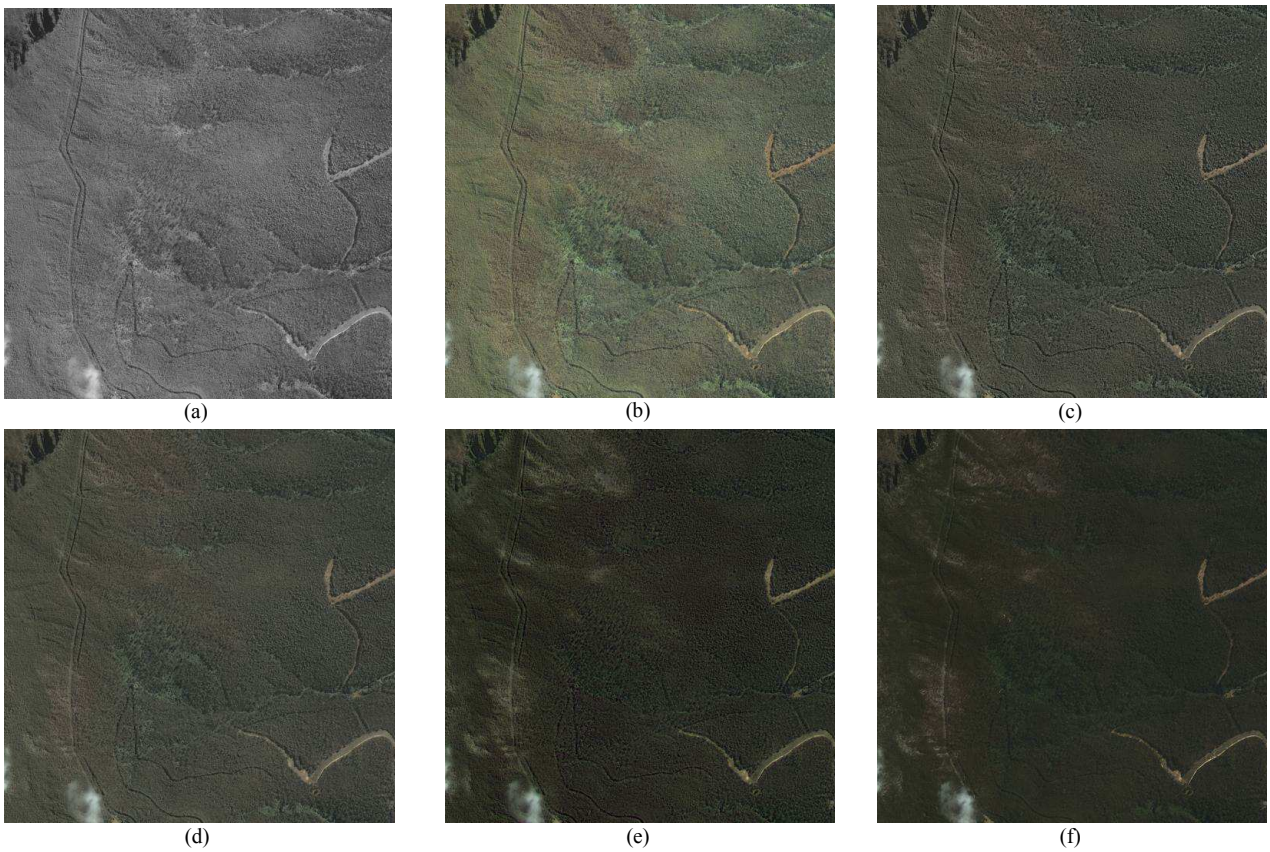

(a) (b) (c) (d) (e) (f)

Figure 4.2 Ikonos test region: (a) Pan image. (b) Classic IHS fused result. (c) TU fused result. (d) CHOI fused result. (e) Proposed fused result. (f) Original MS image.

Obviously, the fused image generated by the classical IHS suffers from significant color distortion. By including the NIR band, the color distortion of the fused image obtained by the rest of methods is mitigated. Furthermore, the fused image achieved by the new method provides the highest spectral similarity to the original color image in Figure 4.2(f). The spatial and the spectral resolutions of the initial MS images appear to have been enhanced. That is, the results of the fusion contain structural details of the Pan image's higher spatial resolution and rich spectral information

from the MS images. Moreover, compared with the results of the fusion obtained by the other tested methods, the results of the proposed method have better visual accuracy. For further verification, the test area in Figure 4.3(f), acquired by QuickBird, is used. This latter image includes more complicated land covers, such as bare soil, and green vegetated areas. The fusion results are displayed in Figure 4.3(b-e). Again, those figures show the same concluding remarks as those corresponding to Figure 4.2.

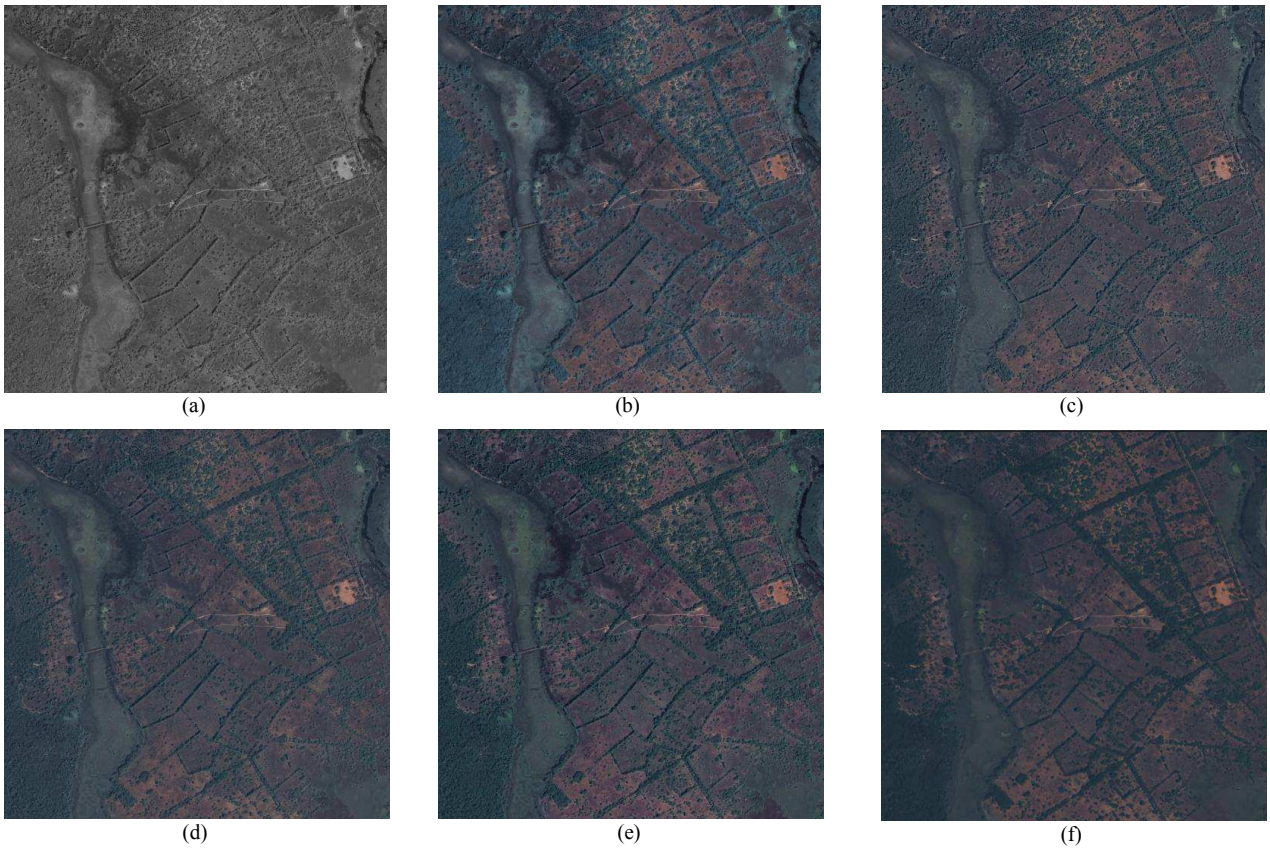

(a) (b) (c)

(d) (e) (f)

Figure 4.3 QuickBird test region: (a) Pan image. (b) Classic IHS fused result. (c) TU fused result. (d) CHOI fused result. (e) Proposed fused result. (f) Original MS image.

**Quantitative analysis**

In addition to visual analysis and in order to quantitatively assess the quality of the fused images in terms of CC, Q, bias, RASE and ERGAS. We created spatially degraded Pan and MS images derived from the original ones. They have a resolution of 1 and 4 m, respectively. Then, they are synthesized at a 1m resolution and compared to the original MS images. Using these factors, Tables 4.1 and 4.2 compare the experimental results of image fusion for the two tested regions with the four methods.

The obtained results show that the proposed approach provides better fusion in terms of bias, RASE and ERGAS for the two tested regions comparatively to TU and CHOI methods. In general, the larger vegetation area is, the better results are obtained.

| Metric | Band | Classic | TU | CHOI | Proposed |
|---|---|---|---|---|---|
| CC | R | 0.5521 | 0.6846 | 0.7321 | **0.8601** |
| | G | 0.5065 | 0.6794 | **0.7271** | 0.7139 |
| | B | 0.4822 | 0.5888 | 0.6419 | 0.**8546** |
| *Q* | R | 0.2667 | 0.3666 | 0.4317 | **0.6273** |
| | G | 0.2352 | 0.3531 | **0.4203** | 0.3932 |
| | B | 0.1680 | 0.2192 | 0.2668 | **0.4938** |
| Bais | R | 0.2093 | 0.0981 | 0.1004 | **0.0011** |
| | G | 0.2166 | 0.0981 | 0.1004 | **0.0001** |
| | B | 0.1791 | 0.0981 | 0.1004 | **0.0008** |
| RASE | | 271.3365 | 194.6752 | 193.7181 | **99.8919** |
| *ERGAS* | | 30.9925 | 16.1258 | 15.9635 | **4.3290** |

Table 4.1 A Comparison of image fusion by Classic IHS, Tu Method, Choi Method and the Proposed Method for Ikonos Test region.

| Metric | Band | Classic | TU | CHOI | Proposed |
|---|---|---|---|---|---|
| CC | R | 0.8176 | 0.8354 | 0.8614 | **0.8941** |
| | G | 0.6614 | 0.7397 | **0.7767** | 0.7381 |
| | B | 0.3716 | 0.5311 | 0.5736 | **0.6209** |
| *Q* | R | 0.7183 | 0.7194 | 0.7592 | **0.8228** |
| | G | 0.5643 | 0.6306 | **0.7116** | 0.6143 |
| | B | 0.2848 | 0.4025 | **0.4859** | 0.4650 |
| Bais | R | 0.0435 | 0.0464 | 0.0385 | **0.0218** |
| | G | 0.0492 | 0.0464 | 0.0385 | **0.0261** |
| | B | 0.0556 | 0.0464 | 0.0385 | **0.0257** |
| RASE | | 107.9817 | 101.1529 | 92.1941 | **86.6141** |
| *ERGAS* | | 6.9703 | 6.1965 | 5.1628 | **4.5098** |

Table 4.2 A comparison of image fusion by Classic IHS, Tu Method, Choi Method and the Proposed Method for QuickBird Test region.

#### 4.2.2.2 Conclusion

We have presented a new approach for image fusion based on the IHS method. Due to non ideal spectral responses of the Ikonos and QuickBird imagery, the original IHS technique often produces color distortion problems in fused images, especially on vegetated areas. The proposed method boosts the green band, by using NIR and red bands information, in the vegetation area in order to magnify the intensity grey values. The fusion of the Pan and enhanced intensity image reduces the distortion in MS color images. Visual and quantitative analyses of experimental results show that the proposed method gives the best fused images in terms of CC, Q, bias, RASE and ERGAS when the area of the manipulated images is mostly vegetation. Moreover, even when the image contains less vegetation, the results obtained by the proposed technique are still satisfactory and promising.

### 4.2.3 Method 2

In this second proposed method, the vegetation enhancing is done after the fusion process, allowing the production of images with natural colors. Instead of using NDVI for delineating the vegetation, we propose and use a new vegetation index. This index is the high resolution normalized difference vegetation index (HRNDVI). The pansharpening procedure is performed in two steps: multispectral fusion using the IHS technique and then vegetation enhancement. The vegetation enhancement is a correction step and depends on the considered application. The new approach provides excellent results in terms of objective quality measures. In addition, visual analysis proves that the concept of the proposed approach improves well the fusion quality by enhancing the vegetated zones, thus is promising. The contribution of this algorithm is to define a fusion technique that can preserve the Pan spatial and the MS spectral qualities, and that produces the best possible images for vegetation visualization. Hence, an overview of some recent related research is presented and then a new inspired approach is proposed and described. It can be used for fusion and for vegetation visualization applications. It is accomplished in two steps. The first one is a fusion scheme, based on the GIHS method with spectral adjustment. The second step is a vegetation enhancement process, where only the vegetated areas are boosted. The value of the parameter used for boosting the vegetation depends on the considered application. This value will be high if vegetation visualization is considered.

Before presenting the proposed method 2, some details about the spectral response of Ikonos and the IHS transformation formulas are presented in the next sections. This is necessary for the easy explanation of method 2.

#### 4.2.3.1 Spectral response of Ikonos

Figure 1.15, given in chapter 1, shows the spectral responses of Ikonos. In this spectral response, three major problems are noticeable [175]:

- The Pan band response extends from the visible to the NIR part of the electromagnetic spectrum.
- Most of the B band response is out of the Pan band range.
- The G and B bands overlap substantially.

Obviously, the color distortion in the fusion process results from these mismatches. Generally speaking, if the spectral responses of the MS bands do not lay perfectly within the Pan band, as it happens with the most advanced very high resolution imagers, namely Ikonos, then the IHS-based methods may yield poor results in terms of spectral fidelity. Therefore, in order to improve the fused results, the spectral response must be considered in the merging process.

Hence, to obtain a better quality in image fusion, the authors in [72] proposed a spectral adjustment scheme integrated into an IHS transformation (SAIHS). In this case, the *I* component is obtained by a weighted sum of the four bands: R, G, B and NIR. The choice of these weights is related to the spectral responses of the Pan and MS bands by considering the spectral characteristics of the sensors. In [72], the authors decreased the contribution of the B and G bands in the computation of the *I* component and introduced the NIR band in it. In [145], Choi used the average of the four bands R, G, B and NIR as the *I* component. The fusion is conducted using a parameter to control the tradeoff between the spatial and the spectral resolutions of the image to be fused. To obtain a color-enhanced image, the author proposed to use three different tradeoff parameters. The parameter used for the G band was greater than the parameter used for the B band. Decreasing the contribution of the B band reduces its effect in the vegetated area.

#### 4.2.3.2 IHS fusion technique

Before conducting an IHS fusion, the color image should be registered with the high-resolution Pan image and resampled to the same pixel size with the Pan image [38]. Next, the three bands R, G and B of a color image have to be transformed from the RGB space into the IHS space. The IHS fusion consists of the following steps [67]:

- Upsample MS RGB images to the Pan pixel size, then convert them as:

$$\begin{bmatrix} I \\ v_1 \\ v_2 \end{bmatrix} = \begin{bmatrix} \frac{1}{3} & \frac{1}{3} & \frac{1}{3} \\ -\frac{\sqrt{2}}{6} & -\frac{\sqrt{2}}{6} & \frac{2\sqrt{2}}{6} \\ \frac{1}{\sqrt{2}} & -\frac{1}{\sqrt{2}} & 0 \end{bmatrix} \times \begin{bmatrix} R \\ G \\ B \end{bmatrix} \tag{4.5}$$

Where R, G, and B represent the corresponding values in the original RGB image, $v_1$ and $v_2$ are intermediate components used to calculate the H and S components.

- Substitute the intensity component *I* with the co-registered Pan image;
- Transform the H, S and the substituted Pan image back to the RGB space by the inverse IHS transform:

$$\begin{bmatrix} R' \\ G' \\ B' \end{bmatrix} = \begin{bmatrix} 1 & -\frac{1}{\sqrt{2}} & \frac{1}{\sqrt{2}} \\ 1 & -\frac{1}{\sqrt{2}} & -\frac{1}{\sqrt{2}} \\ 1 & \sqrt{2} & 0 \end{bmatrix} \times \begin{bmatrix} PAN \\ v1 \\ v2 \end{bmatrix} \tag{4.6}$$

R', G', and B' are the corresponding values to RGB in the fused images.

By rewriting (4.6), the authors in [67], present a computationally efficient method (FIHS) as:

$$\begin{bmatrix} R' \\ G' \\ B' \end{bmatrix} = \begin{bmatrix} R+\delta \\ G+\delta \\ B+\delta \end{bmatrix} \tag{4.7}$$

where $\delta = Pan - I$ and $I = (R+G+B)/3$ (4.8)

Equation (4.7) states that the fused image $[R', G', B']^T$ can be obtained easily and directly from the original image $[R, G, B]^T$ by simple addition operations. The fused image obtained after the FIHS fusion provides the full details of Pan but introduces color distortions. In (4.7), a large value of $\delta$ appears to cause a large spectral distortion in the fused images. In order to reduce this effect, one must generate an intensity component *I*, which must be as close as possible to the Pan image.

The authors demonstrated that when the NIR band is available, a possible solution is to define a generalized IHS transform by including the response of the NIR band into the intensity component. In this case, *I* is obtained by weighting each band with a set of coefficients. The choice of these weights can be related to the spectral responses of the Pan and MS bands by considering the spectral characteristics of the sensors. By differently weighting the contributions coming from the MS images, one obtains:

$$I = w_R R + w_G G + w_B B + w_{NIR} NIR \cong Pan \tag{4.9}$$

Two algorithms, corresponding to two sets of the weighting coefficients ($w_R$, $w_G$, $w_B$, $w_{NIR}$), are presented in [72]. The first scheme consists of the generalized IHS (GIHS) method, where the intensity component is simply the average of the four MS images, i.e. $I = (R+G+B+NIR)/4$. The second algorithm uses the spectral-adjustment IHS (SAIHS) method with another weighting for *I* : $I = (R+aG+bB+NIR)/3$. The values of 0.75 and 0.25 corresponding to *a* and *b*, respectively, are found to be suitable to fuse the Ikonos images.

With these considerations, a general expression can clearly be defined for the fusion process as:

$$Fused\,Band = Band + \delta \text{ where } \delta = Pan - I \tag{4.10}$$

Where *Band* represents one of the MS bands and :

$$I = I_3 = (R+G+B)/3 \qquad \text{for FIHS} \tag{4.11}$$

$$I = I_4 = (R+G+B+NIR)/4 \qquad \text{for GIHS} \tag{4.12}$$

$$I = I_{SA} = (R+aG+bB+NIR)/3 \qquad \text{for SAIHS} \tag{4.13}$$

In [145], while using GIHS, Choi proposed a new IHS approach for image fusion with an adjustment parameter reflecting spectral characteristics of the sensors. Instead of using the spectral

adjustment in the computation of *I* component, he used it to calculate each fused band. His proposed method is expressed as follows:

$$\begin{bmatrix} R' \\ G' \\ B' \\ NIR' \end{bmatrix} = \begin{bmatrix} Pan - \dfrac{(Pan - I_4)}{t} + (R - I_4) \\ Pan - \dfrac{(Pan - I_4)}{t} + (G - I_4) \\ Pan - \dfrac{(Pan - I_4)}{t} + (B - I_4) \\ Pan - \dfrac{(Pan - I_4)}{t} + (NIR - I_4) \end{bmatrix} \tag{4.14}$$

Where *t* is a tradeoff parameter.

To write (4.13) in a general expression form, let:

$$\alpha = \frac{t-1}{t} \tag{4.15}$$

Then:

$$Fused\,Band = Band + \alpha\delta_4, \text{ where } \delta_4 = Pan - I_4 \tag{4.16}$$

A suitable value of the tradeoff parameter *t* for Ikonos images was found to be equal to 4, hence $\alpha = 3/4$.

In Ikonos, the vegetation zones of the MS images are much darker because the vegetation appears to have relatively low reflectance in RGB bands. To overcome this problem and to obtain a color-enhanced image, three different tradeoff parameters: $t_R = 2.5$, $t_G = 3.5$ and $t_B = 2.0$ are used in [145]. Each MS band was enhanced with a parameter reflecting its spectral response.

The technique presented in [78] tries, also, to solve the same problem. Then a new vegetation index (VI), given in (4.21), is proposed to boost the G band in vegetated areas. The obtained modified FIHS was then derived as:

$$\begin{bmatrix} R' \\ G' \\ B' \end{bmatrix} = \begin{bmatrix} R + \delta_3 \\ G + \delta_3^{'} \\ B + \delta_3 \end{bmatrix} \tag{4.17}$$

with $\delta_3 = Pan - I_3$, (4.18)

To detect a vegetated area, two ways are proposed

- If VI is considered, then $\delta_3^{'} = \begin{cases} \delta_3 & VI \le 0 \\ k\delta_3 & VI > 0 \end{cases}$ (4.19)

- If NDVI is used, then $\delta_3^{'} = \begin{cases} \delta_3 & NDVI \le \theta \\ k\delta_3 & NDVI > \theta \end{cases}$ (4.20)

Where $k$ is a constant fixed to 2 for Ikonos imagery. In practice, the threshold $\theta$ is selected manually. The idea of using the vegetation detection in the fusion procedure, reported in [85], [86] and [78], is that the fused images have a true natural color, especially in the vegetated zones.

#### 4.2.3.3 Ikonos high resolution vegetation index

The NDVI is the most used vegetation index for a variety of remote sensing applications. It was generally developed for coarse resolution imagery, and is rarely used to generate high-resolution vegetation maps directly. On the other hand, in some applications, the Ikonos imagery can be used to map a vegetation cover or to validate a vegetation cover classified from other remote sensing images [176]. In addition, the Ikonos Pan images provide more details of buildings and individual trees, while vegetation structural variations can be well detected with 1-meter spatial resolution images. However, the vegetation zones of the MS images are much darker because the vegetation appears to have relatively low reflectance in RGB bands. Therefore, when vegetation is the object of interest, an enhanced-vegetation fused result is the objective. In this case, usually a vegetation index is used in order to delineate the vegetated area where the enhancement is to be done. In [86], the author proposed a technique for Ikonos image fusion, for when the main purpose of a specific image is vegetation visualization. The technique consists of a hue spectral adjustment scheme integrated into an IHS transformation. The NDVI was used to correct the hue component. The idea reported in [85] is to boost the G band, and hence the $I$ component, in order to minimize the difference between the Pan image and the $I$ component. The boosting was applied only in the vegetated area detected using the NDVI. The IHS type used was the classical transform. In a recent study [78], the FIHS is used and a G band boosting in the vegetated area is performed. A vegetation index VI was proposed: it takes advantage of the high spatial resolution information of the Pan images. This VI is expressed as:

$$VI = \frac{Pan - I_3}{Pan + I_3} \tag{4.21}$$

It uses the Pan image and the $I$ component instead of the NIR and R bands and seems to be interesting since it contains much spatial details provided by the Pan image. However, applying the VI on our images did not yield expected good results. In fact, although several thresholds are used, some confusion is always observed in distinguishing vegetation and from shadows.

In order to take into account the spatial resolution of the Pan images, a new NDVI is proposed using the fused bands. A high resolution vegetation map can be generated using the fused low resolution R and NIR bands with the high-resolution Pan image. This index will be denoted HRNDVI for High Resolution NDVI. As the conventional NDVI is defined by:

$$NDVI = \frac{NIR - R}{NIR + R}, \tag{4.22}$$

The new index is defined by:

$$HRNDVI = \frac{Fused\,NIR - Fused\,R}{Fused\,NIR + Fused\,R} \tag{4.23}$$

Generally, the fused bands R and NIR contain a part from the Pan image, which spatially improves the proposed HRNDVI. The fused bands are obtained using (4.16):

$$\begin{bmatrix} Fused\,R \\ Fused\,NIR \end{bmatrix} = \begin{bmatrix} R + \alpha\delta_4 \\ NIR + \alpha\delta_4 \end{bmatrix} \tag{4.24}$$

We use $\alpha = 1$ so that the fused bands provide the full details of Pan [177], which is a real advantage for the HRNDVI.

Based on this, (4.23) is rewritten, using the MS and Pan images, as:

$$HR\,NDVI = 2\frac{NIR - R}{NIR + R - B + 4Pan - G} \tag{4.25}$$

Equation (4.25) is the definition of the new index HRNDVI that is proposed for Ikonos images. This formula is highly similar to the one of the Enhanced Vegetation Index (EVI) [178].

The importance of using Pan images for computing the vegetation index is illustrated by the example of Figure 4.4. Comparing the Pan image (Figure 4.4(a)) with the RGB image (Figure 4.4(b)) states that a “monument” surrounded by a white ellipse is not visible in the MS images. This “monument” is recovered after the IHS fusion, using the GIHS method: the fused image is shown in Figure 4.4(c). The NDVI and HRNDVI thresholds are set to 0.2 and 0.15 respectively. If the NDVI is based on the R and NIR bands only, then an error in vegetation detection may occur in the “monument” area. However, if NDVI makes use of the fused bands, this error will mitigate. In Figure 4.4(e), the vegetation indexes, corresponding to the “monument” column 67 (red column in Figure 4.4(d)), namely NDVI, HRNDVI and VI are plotted.

All the VI values are higher than 0 which means that the VI index considers this column as a vegetation area. Moreover, some NDVI values, corresponding to rows (55 to 64), are also significant (higher than 0.2). This is due to the large difference between the NIR and R bands. In this range of rows, NDVI confuses the detection of the “monument” with vegetation. Unlike the two vegetation indexes all the values of HRNDVI are smaller than the threshold leading to no error in the vegetation detection. In this example, the impact of the Pan image, in vegetation detection, is obvious. In general, if the Pan image is considered in the computation of the vegetation index, more errors related to detailed information will disappear.

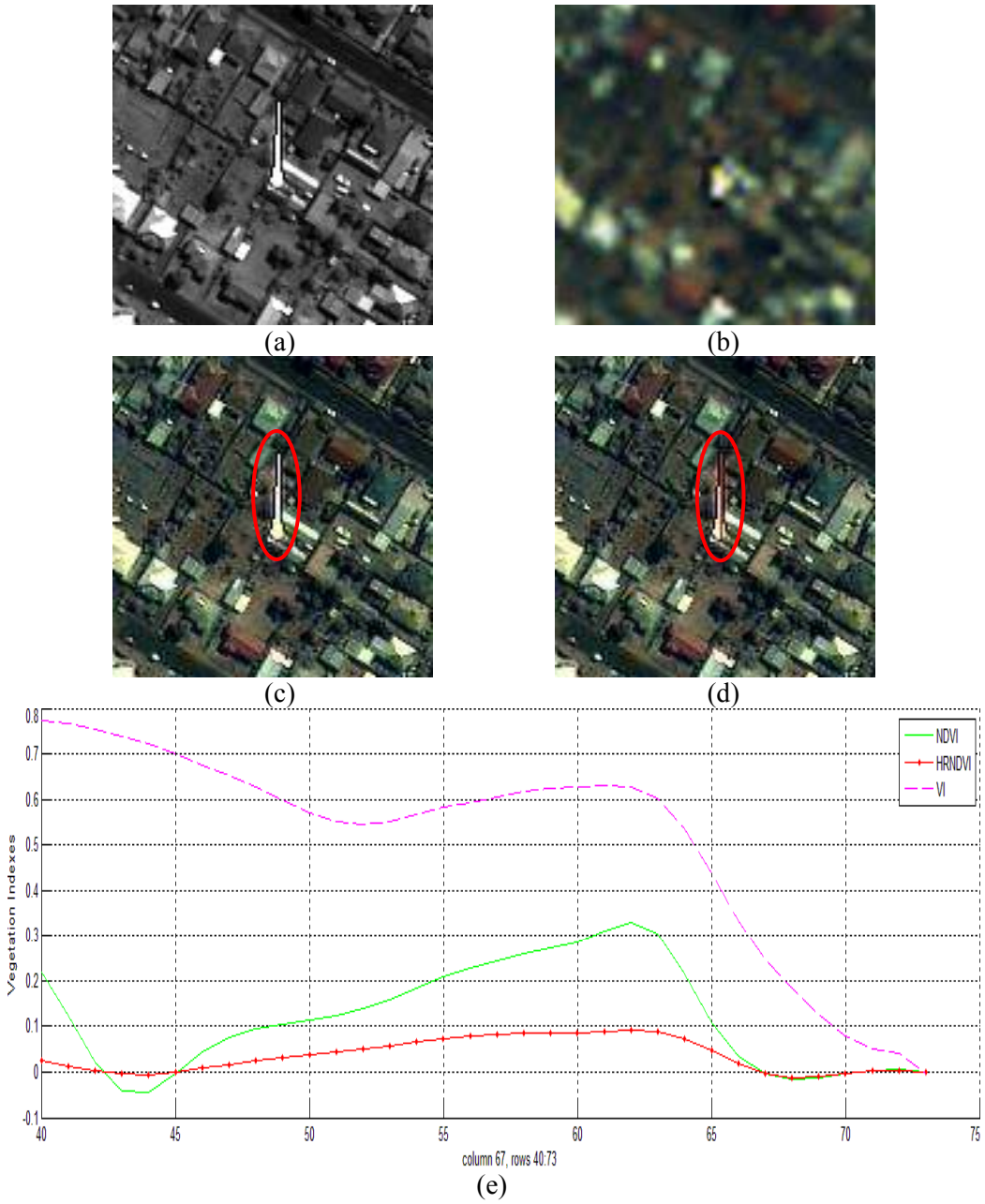


Figure 4.4 (a) Pan image, (b) RGB image, (c) GIHS fused image, (d) considered column in red color, (e) NDVI, VI and HRNDVI corresponding to the red column in (d).

Figure 4.5 shows an example for comparing NDVI, VI and HRNDVI. The scene contains a part of a stadium and some surrounding buildings. The upsampled RGB image and the Pan image are given in Figure 4.5(a) and Figure 4.5(b) respectively.

The white line showed in Figure 4.5(a) will be used to compare vegetation indexes. Figure 4.5(c) shows the vegetation mapping using NDVI with a 0.25 threshold. The vegetation mapping using VI is reported in Figure 4.5(d) and Figure 4.5(e) with 0 and 0.2 thresholds respectively. The white color in Figure 4.5(c), Figure 4.5(d), Figure 4.5(e) and Figure 4.5(f) corresponds to vegetation. Figure 4.5(f) illustrates the vegetation mapping using HRNDVI with a threshold of 0.2. Figure 4.5(d) and Figure 4.5(e) state that a threshold of 0 does not give good results, as stated by the

author in [78], and when increasing the threshold, to improve this result, some vegetation information are lost, and some building shadows appear as vegetation.

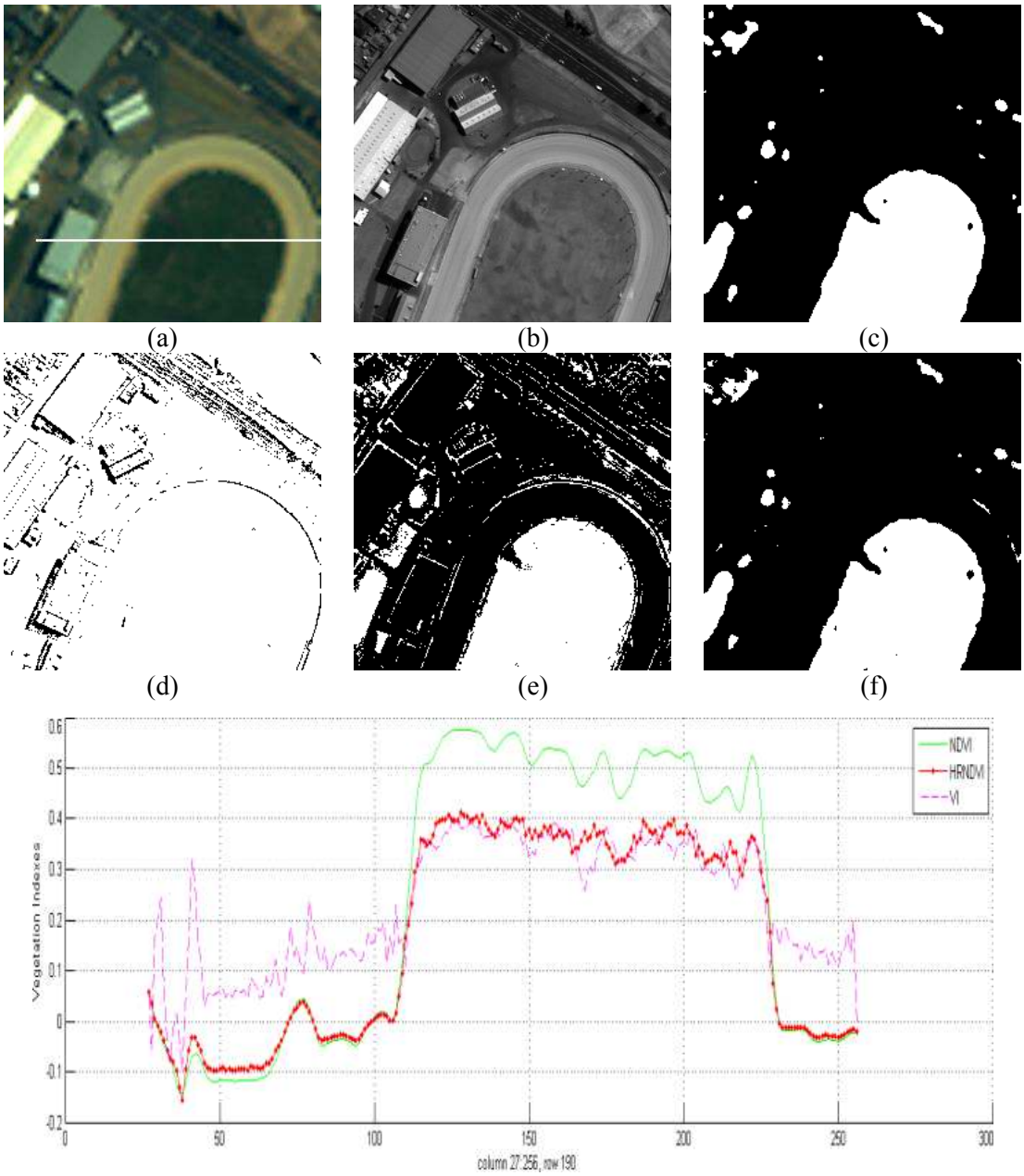


Figure 4.5 (a) RGB image, (b) Pan image, (c) NDVI with threshold 0.25, (d) VI with threshold = 0, and (e) VI with threshold = 0.2 (f) HRNDVI with threshold = 0.2 (g) NDVI, VI and HRNDVI corresponding to the white line in RGB image.

The VI and HRNDVI indices make use of the Pan image to include more details than the conventional NDVI index. Consider only one line (white line) from Figure 4.5(a). The corresponding NDVI, HRNDVI and VI indices are plotted in the same figure (Figure 4.5(g)). HRNDVI and VI have more high frequencies than NDVI. Observing this plot, they have a better spatial resolution compared to the NDVI index. However, VI presents some confusion in vegetation detection, namely around edges. Normally, from column 27 to 99 and from 228 to 256, there is no vegetation in Figure 4.5(a). But some values of VI are significant in these intervals. This

is due to the large values of the Pan image compared to $I_3$ in non-vegetated areas. In conclusion, HRNDVI appears to be a solution where the spatial information of the Pan image is used without any vegetation detection confusion.

Figure 4.6 shows the difference between NDVI (Figure 4.6(b)) and HRNDVI (Figure 4.6(c)) obtained from the MS and Pan images. High frequency is obviously apparent in Figure 4.6(c), especially in dense vegetation (top and middle boxes).

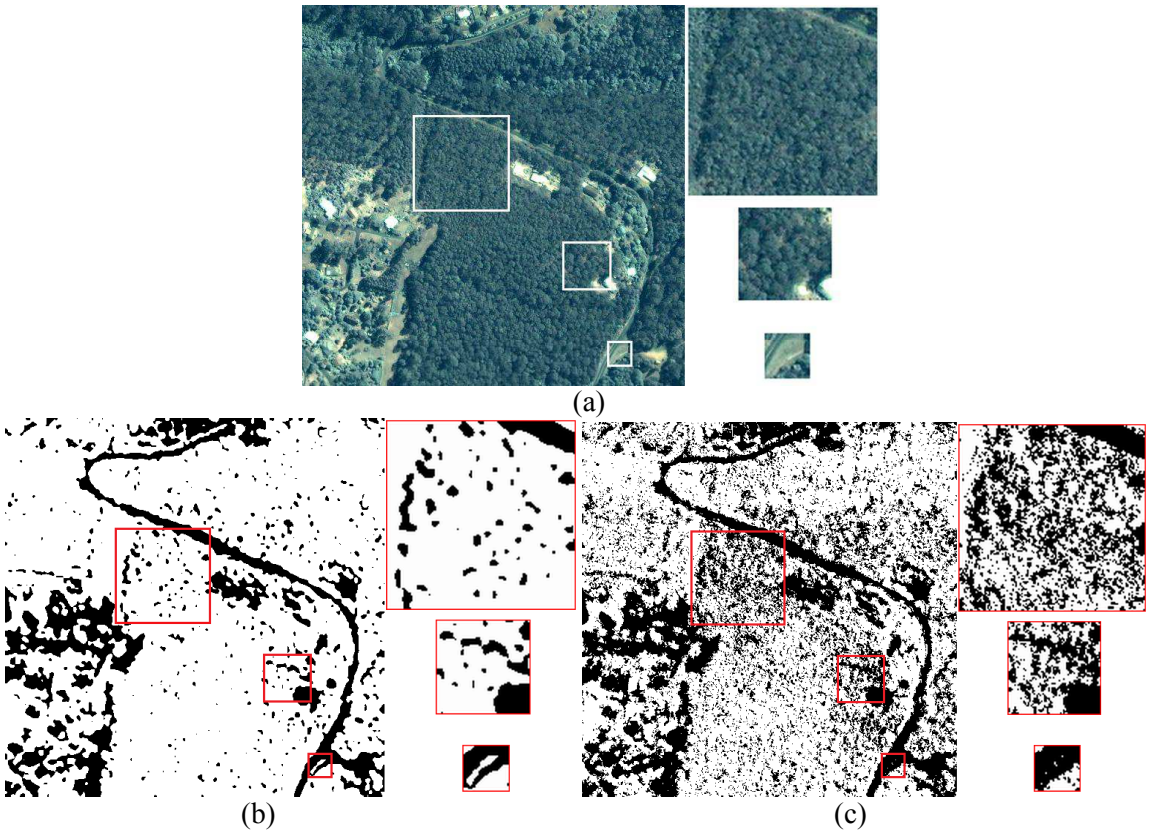


Figure 4.6 (a) GIHS fused image, (b) NDVI with threshold 0.35, (c:) HR NDVI with threshold 0.3.

The HRNDVI index preserves more detailed vegetation areas than the conventional NDVI one. In Figure 4.6(a), in the bottom box, the oblique structure, which is not a vegetation area, appears in Figure 4.6(b) in white, corresponding to false vegetation detection, while it can be noticed that this false detection does not occur in Figure 4.6(c).

The contribution of the Pan image, in detecting vegetation, is obviously apparent in the VI and HRNDVI maps. By this means, these two vegetation indexes preserve more detailed vegetation areas than the conventional NDVI. Although, VI has a better spatial resolution, compared to NDVI, all the conducted and observed examples show that VI presents some confusion in vegetation detection. The proposed HRNDVI index is a good solution to introduce the spatial resolution in the computation of NDVI and guaranties less confusion in the vegetation detection process. It provides a new data source for monitoring agricultural production, and for giving information for the development of crops during the growing season. For all the experiments conducted, a good value

of the HRNDVI threshold is estimated as being 0.05 less than the threshold value of NDVI. So in the case of the traditional threshold of 0.2 for NDVI, the threshold of HRNDVI is 0.15.

#### 4.2.3.4 Description of method 2

The spectral response of Ikonos and the works conducted in [85], [145], [86], [72] and [78] state that the Ikonos pansharpening process needs boosting the G band, decreasing the contribution of the B band and exploiting the NIR band. Moreover, because the problems of color distortion are more visible in the vegetated areas, only these areas will be enhanced in our approach.

In order to improve the fused images, particularly in the vegetated areas, a new fusion algorithm is proposed. The most important novelty is to tune the two bands G and B, rather than the G band alone, in the vegetated areas. Moreover, the proposed HRNDVI index is used to detect the vegetation. In addition, the NIR band, which reflects vegetation, is used in the computation of the *I* component. As in GIHS, equation (4.12) expresses this component.

Equation (4.17) is reformulated, in a manner to distinguish the two processes: the fusion and the vegetation enhancement. Hence, this equation can be expressed as:

$$\begin{bmatrix} R' \\ G' \\ B' \end{bmatrix} = \begin{bmatrix} R+\delta_3 \\ G+\delta_3{}' \\ B+\delta_3 \end{bmatrix} = \begin{bmatrix} R+\delta_3 \\ G+k\delta_3 \\ B+\delta_3 \end{bmatrix} = \begin{bmatrix} R+\delta_3 \\ G+\delta_3 \\ B+\delta_3 \end{bmatrix} + \begin{bmatrix} 0 \\ (k-1)\delta_3 \\ 0 \end{bmatrix} \tag{4.26}$$

Where k = 2 for the vegetated areas and k = 1 for the non-vegetated areas if Ikonos images are used [78]. $\delta_3$ is given in (4.18). The term $(k-1)\delta_3$ in (4.26), applied for the G band, represents the vegetation enhancement.

In [145], for color enhancement applications, each fused band used a different value of t; $t_R$, $t_G$ and $t_B$. Using equation 4.15, for three bands, equation (4.14) is rewritten as:

$$\begin{bmatrix} R' \\ G' \\ B' \end{bmatrix} = \begin{bmatrix} R+\alpha_R\delta_4 \\ G+\alpha_G\delta_4 \\ B+\alpha_B\delta_4 \end{bmatrix} \tag{4.27}$$

Where $\delta_4$ is given in equation (4.16), and $\alpha_R$, $\alpha_G$, and $\alpha_B$ are computed using (4.15) from $t_R=2.5$, $t_G=3.5$ and $t_B=2.0$, respectively. Rewriting (4.27) in the same format as (4.26), where the fusion and vegetation enhancement are distinguished, gives

$$\begin{bmatrix} R' \\ G' \\ B' \end{bmatrix} = \begin{bmatrix} R+\alpha\delta_4 \\ G+\alpha\delta_4 \\ B+\alpha\delta_4 \end{bmatrix} + \begin{bmatrix} \beta_R\delta_4 \\ \beta_G\delta_4 \\ -\beta_B\delta_4 \end{bmatrix} \tag{4.28}$$

where $\alpha = 0.6$ (4.29)

and where $\beta_R = 0$, $\beta_G = 0.11$ and $\beta_B = 0.13$ (4.30)

Equation (4.28) compared to (4.26) states that the enhancement is applied to the G and B bands for the whole fused image.

By using the idea of [85], [86] and [78], we propose to enhance only the vegetated areas. Moreover, to simplify the fusion problem, the number of parameters in (4.28) is decreased by assuming that: $\beta_G = \beta_B = \beta$. Hence, in the proposed method, the same amount $\beta\delta_4$ is used to increase the values of the G band and decrease those of the B band, but only in the vegetation zones.

The visual analysis conducted on 132 images confirm that the average values of 0.6 and 0.12 for α and β, respectively, provide good overall results in fusion applications. These values are well suited for images where most of the areas are vegetation. Additionally, for images with less vegetation, the results may be improved by adapting different values for a parameter α in a 0.6~0.8 range. The value of α controls the spatial information injected in the fused images and is related to the vegetation quantity in the image.

The new proposed algorithm, generalized for four bands, can be summarized by the following procedure:

- Calculate the HRNDVI index using (4.25).
- Compute the intensity component $I_4$ and the corresponding difference $\delta_4$ using (4.12) and (4.16).
- Compute the fused bands as : $\begin{bmatrix} R' \\ G' \\ B' \\ NIR' \end{bmatrix} = \begin{bmatrix} R+\alpha\delta_4 \\ G+\alpha\delta_4 \\ B+\alpha\delta_4 \\ NIR+\alpha\delta_4 \end{bmatrix}$, where $\alpha = 0.6$, (4.31)
- Enhance the vegetated zones by applying a correction in the two bands G and B :

$$\begin{bmatrix} G'' \\ B'' \end{bmatrix} = \begin{bmatrix} G'+\beta\delta_4 \\ B'-\beta\delta_4 \end{bmatrix}, \quad \text{for } HRNDVI > \theta \tag{4.32}$$

The resulting fused-enhanced bands are $[R', G'', B'', NIR']$. $\beta$ is the enhancing term and depends on the considered application. From the performed experiments, a value of $\beta = 0.12$ produces better results, for fusion purposes. In addition, if this algorithm is used for vegetation visualization, a value of 0.25 for $\beta$ gives a natural look to the vegetated areas making the fused image more appreciable. Experimental results for fusion and vegetation visualization will be discussed in the next section.

### 4.2.3.5 Experimental results

The same Ikonos images, used for evaluating the first method, were used for assessment of this second method. In order to illustrate the efficiency of our algorithm, two subsets of images are used. The first one is mostly vegetation and the second one contains less vegetation. Small size images of 256x256 pixels will be considered. For comparison purposes, the FIHS, GIHS, SAIHS given in equations 4.10 – 4.13, the Choi's method given in equation 4.14 with t = 4 and the Tu's method expressed in 4.17 – 4.19, are implemented and tested. Finally, the proposed method is presented with two values for the enhancing term: $\beta_1 = 0.12$ for fusion and $\beta_2 = 0.25$ for both fusion and vegetation visualization.

**Quantitative analysis**

For each spectral band, we compute: the bias in relative value, the difference in variance in relative value, the standard-deviation of the differences on a pixel basis in relative value, the correlation coefficient and the correlation between high frequencies. For the whole data set, the average spectral angle mapper (SAM), the relative dimensionless global error in synthesis (ERGAS) and the quality index (Q4) are used.

To evaluate the spectral and spatial quality of the fused images, degraded Pan and MS images are used. The MS images have a 4m resolution, which is four times less than the Pan image's 1m resolution. By down-sampling the MS and Pan images by a factor of four, the degraded MS and Pan images with 16m and 4m resolutions, respectively, are obtained [131]. The fusion process is applied on the degraded MS and Pan images to produce MS fused images with a 4m resolution. The MS images, before down-sampling, are considered as original images. The fused MS images are compared to those original MS images using the quality indexes presented previously. Tables 4.3 and 4.4 compare the experimental results of image fusion of the proposed method with the five presented methods. As previously seen, the results corresponding to the new proposed method are given with the two selected values: $\beta_1$ for fusion and $\beta_2$ for both fusion and vegetation visualization. Table 4.3 corresponds to the first image set, which is mostly vegetation, given in Figure 4.7. Table 4.4 characterizes the second image set, containing less vegetation, given in Figure 4.8. Both tables show that the method, for the two values of $\beta$, gives good results in terms of bias and standard deviation, regardless of the presence of vegetation. Choi's method produces better values of variance in dense vegetation images for the R and G bands unlike the proposed method which is more suitable for non-dense vegetation images in terms of variance.

The results presented in Tables 4.3 and 4.4 show that our technique gives very good values in terms of spectral and spatial correlations in dense vegetation image.

The developed method gives appreciable results in terms of the global quality measure. Regardless of the image type and for the three metrics: SAM, ERGAS and Q4, our method performs better.

| | Band | FIHS | GIHS | SAIHS | Choi | Tu et al. | Proposed method | |
|---|---|---|---|---|---|---|---|---|
| | | | | | | | $\beta_1$ | $\beta_2$ |
| BIAS | R | 1.0178 | 0.6921 | 0.6459 | 0.5187 | 1.0178 | **0.4149** | **0.4149** |
| | G | 0.6892 | 0.4687 | 0.4374 | 0.3513 | 1.3802 | **0.3248** | 0.3686 |
| | B | 0.6568 | 0.4467 | 0.4169 | 0.3348 | 0.6568 | 0.2260 | **0.1842** |
| VAR | R | 0.8338 | 0.7119 | 0.5485 | **0.0157** | 0.8338 | 0.2978 | 0.2978 |
| | G | 0.6464 | 0.5274 | 0.3929 | **0.1435** | 10.9205 | 0.4409 | 0.4662 |
| | B | 2.8384 | 2.4379 | 2.1388 | 0.6094 | 2.8384 | **0.0657** | 0.1908 |
| SD | R | 0.4101 | 0.3489 | 0.3287 | 0.2620 | 0.4101 | **0.2227** | **0.2227** |
| | G | 0.2800 | 0.2389 | 0.2252 | 0.1792 | 0.5994 | **0.1713** | 0.1947 |
| | B | 0.2917 | 0.2562 | 0.2444 | 0.1889 | 0.2917 | 0.1346 | **0.1234** |
| CC | R | 0.7909 | 0.8416 | 0.8489 | 0.8683 | 0.7909 | **0.8822** | **0.8822** |
| | G | 0.7796 | 0.8303 | 0.8380 | **0.8573** | 0.6898 | 0.8423 | 0.8060 |
| | B | 0.6336 | 0.7001 | 0.7091 | 0.7403 | 0.6336 | 0.8142 | **0.8447** |
| sCC | R | 0.7054 | 0.7051 | 0.7050 | 0.7092 | 0.7054 | **0.7116** | **0.7116** |
| | G | 0.7199 | 0.7171 | 0.7169 | **0.7259** | 0.6998 | 0.7008 | 0.6687 |
| | B | 0.6239 | 0.6140 | 0.6129 | 0.6362 | 0.6239 | 0.6866 | **0.7079** |
| SAM | - | 9.4650° | 8.4745° | 8.3353° | 7.7114° | 13.9798° | **7.4296°** | 7.9132° |
| ERGAS | - | 19.5491 | 13.8652 | 12.9800 | 10.4849 | 25.4848 | **8.6554** | 8.8244 |
| Q4 | - | 0.2166 | 0.2826 | 0.2964 | 0.3631 | 0.1656 | 0.4475 | **0.4605** |

Table 4.3 set 1 Ikonos Image Fusion Results For Mostly Vegetated Areas.

| | Band | FIHS | GIHS | SAIHS | Choi | Tu et al. | Proposed method | |
|---|---|---|---|---|---|---|---|---|
| | | | | | | | $\beta_1$ | $\beta_2$ |
| BIAS | R | 0.3593 | 0.3289 | 0.3207 | 0.2465 | 0.3593 | **0.1972** | **0.1972** |
| | G | 0.2983 | 0.2731 | 0.2663 | 0.2047 | 0.6171 | **0.1734** | 0.1830 |
| | B | 0.3397 | 0.3110 | 0.3032 | 0.2331 | 0.3397 | 0.1755 | **0.1645** |
| VAR | R | 0.8793 | 1.2177 | 1.1182 | 0.5252 | 0.8793 | **0.2238** | **0.2238** |
| | G | 0.7256 | 1.0542 | 0.9943 | 0.4249 | 5.3392 | 0.1217 | **0.0952** |
| | B | 1.8889 | 2.5675 | 2.5237 | 1.1099 | 1.8889 | **0.5724** | 0.6156 |
| SD | R | 0.2643 | 0.2111 | 0.1944 | 0.1763 | 0.2643 | **0.1744** | **0.1744** |
| | G | 0.2267 | 0.1837 | 0.1699 | **0.1512** | 0.4746 | 0.1531 | 0.1618 |
| | B | 0.2802 | 0.2365 | 0.2220 | 0.1710 | 0.2802 | 0.1343 | **0.1313** |
| CC | R | 0.8780 | 0.9277 | **0.9371** | 0.9338 | 0.8780 | 0.9313 | 0.9313 |
| | G | 0.8667 | 0.9188 | **0.9299** | 0.9286 | 0.7684 | 0.9217 | 0.9122 |
| | B | 0.7747 | 0.8597 | 0.8785 | 0.8915 | 0.7747 | 0.9182 | **0.9242** |
| sCC | R | 0.8128 | 0.8137 | **0.8138** | 0.8130 | 0.8128 | 0.8086 | 0.8086 |
| | G | 0.7951 | 0.7962 | 0.7964 | **0.7970** | 0.7777 | 0.7872 | 0.7779 |
| | B | 0.7466 | 0.7478 | 0.7480 | 0.7565 | 0.7466 | 0.7662 | **0.7671** |
| SAM | - | 6.0904° | 5.9155° | 5.8674° | 5.7153° | 8.3383° | **5.6044°** | 5.7179° |
| ERGAS | - | 10.2626 | 9.0587 | 8.7092 | 6.9788 | 13.3448 | **5.9777** | 5.9993 |
| Q4 | - | 0.6694 | 0.7041 | 0.7158 | 0.7768 | 0.5871 | 0.8098 | **0.8107** |

Table 4.4 set 2 Ikonos Image Fusion Results For Mixed Areas.

The examination of Tables 4.3 and 4.4 indicates that:

- When the vegetation is not dense, the proposed method produces very satisfactory results. Even if the SAIHS method appears to have better CC and sCC for the R and G bands, the proposed method improves well the B band, and the global measures show this improvement.

- For an image, which is mostly vegetation, the proposed method, again, gives the best results, even if in terms of variance for the R and G bands, Choi's method is better. To have the same values for variance as those of Choi's method, α must be increased to 0.75. By doing this, the bias and the standard deviation will increase. In addition, the rest of indexes are affected. Hence, a value of 0.6 for α is retained. This value guarantees improvement for all the quality metrics.

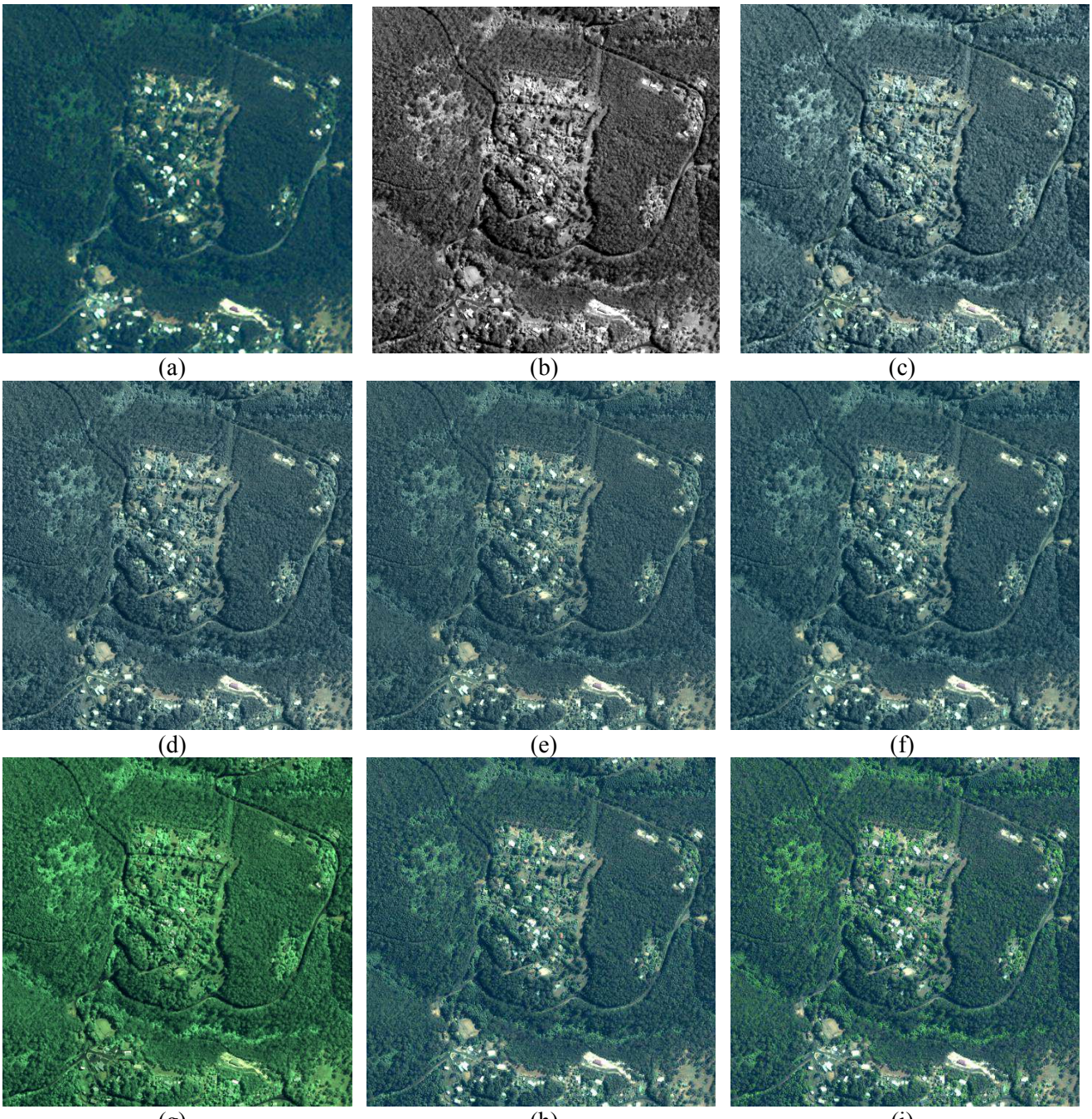

Figure 4.7 First image set (a) RGB image. (b) Pan image. (c) FIHS results. (d) GIHS results. (e) SAIHS results. (f) Choi's results. (g) Tu et al. results. (h) Proposed method results with $\beta_1$. (i) Proposed method results with $\beta_2$.

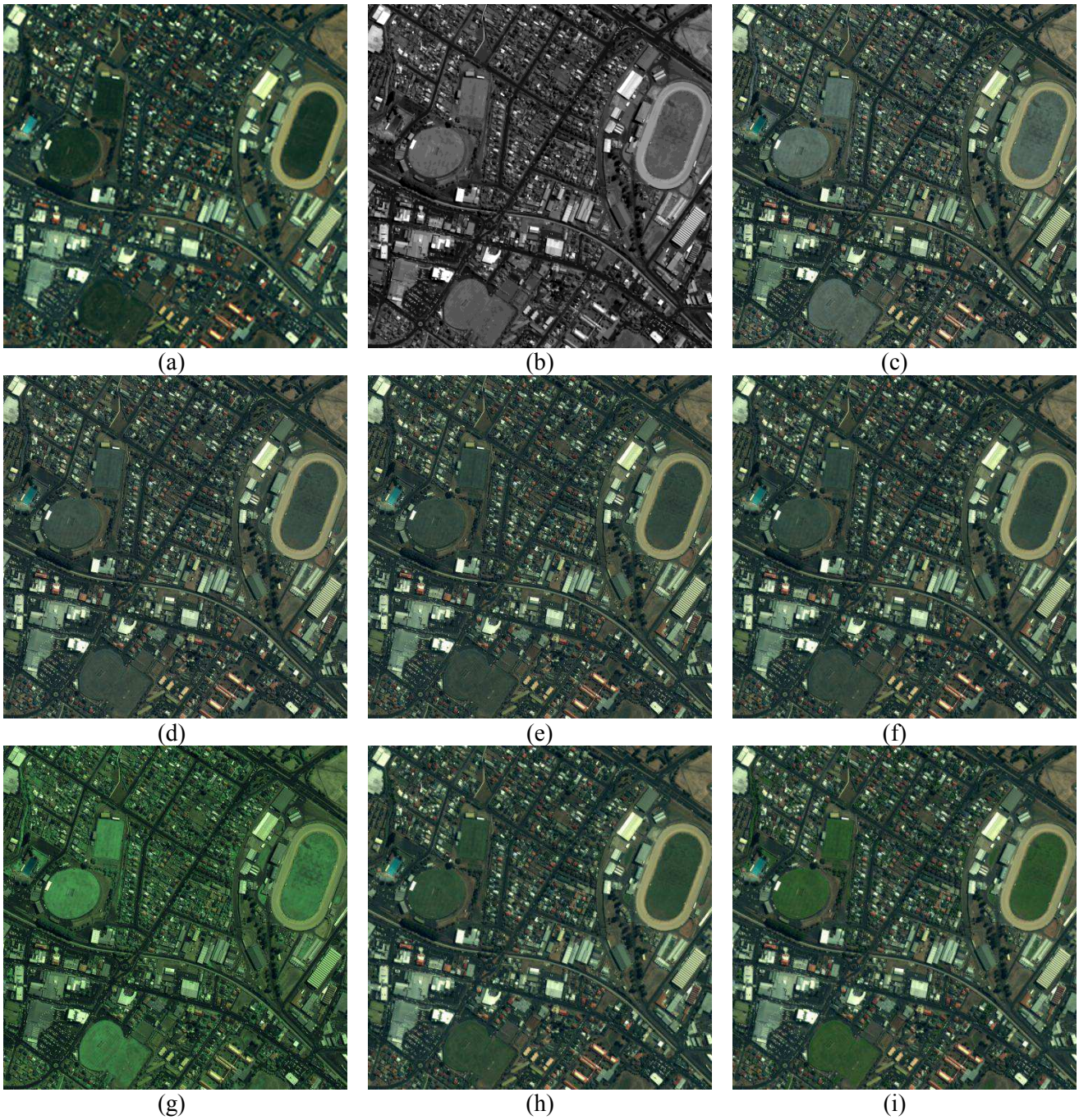

(a) (b) (c)

(d) (e) (f)

(g) (h) (i)

Figure 4.8 Second image set (a) RGB image. (b) Pan image. (c) FIHS results. (d) GIHS results. (e) SAIHS results. (f) Choi's results. (g) Tu et al. results. (h) Proposed method results with $\beta_1$. (i) Proposed method results with $\beta_2$.

**Visual analysis**

Figure 4.7 and Figure 4.8 show the fusion results obtained using different methods. In the two figures, (a) represents the original RGB image upsampled to the Pan image size shown in (b). The fused results obtained using the FIHS, GIHS, SAIHS, Choi and Tu methods are illustrated in (c), (d), (e) (f) and (g), respectively. To show the efficiency of our method according to objectives in fusion or vegetation visualization, two fused results are presented. The first one (h) for fusion purposes, and the second one (i) for both fusion and vegetation enhancement.

The color distortion is apparent in the FIHS and GIHS results. However, the SAIHS and Choi results are better, but the vegetation appears unnatural. The Tu et *al.* results show an excessive greenness in the vegetated area. This is due to the use of VI with a 0 threshold. Normally, increasing the threshold value improves the results, if the used images are natural. In fact, the VI index is designed for the vegetation layer of GIS and military applications as Camouflage.

In any case, the proposed method provides good results. This method tries to solve the problems evoked in [175] and presented in section 2.1. Hence, the NIR band is used in computing the intensity component, and the contribution of the three bands are weighted according to the spectral response of the sensors. The use of a correction term, in vegetated areas, for the G and B bands has strongly improved the visual quality, and a natural color is obtained.

**Color enhancement**

In order to show the capabilities of the proposed method, two examples (A and B) are illustrated in Figure 4.9(a). The first case is presented in Figure 4.9(b), Figure 4.9(d) and Figure 4.9(f). This area is chosen in order to demonstrate the improvement for the G and B bands. The proposed method produces the best results, as can be seen: the green and blue colors appear natural. In Figure 4.9(c), Figure 4.9(e) and Figure 4.9(g) corresponding to the second case, the importance of using the new vegetation index HRNDVI is highlighted. The fused results presented in Figure 4.9(e) and Figure 4.9(g), are obtained using the conventional NDVI and HRNDVI indices, respectively. In the proposed method, enhancement is applied in vegetation areas only. So if some errors are made in the vegetation detection process, the final result is affected. As shown in Figure 4.4, NDVI introduces some errors in the “monument” area. Then enhancing these false vegetation areas introduces color distortions, where a white color pixel appears as yellow due to increasing the G and decreasing the B bands. One can notice that using HRNDVI has eliminated the color distortions (bright regions characterized by a fluorescent color) that are observed (white circles) in Figure 4.9(e) when using the conventional NDVI index. Our method is based on the vegetation detection in order to enhance the vegetated area. Hence, if the detection of vegetation presents some error, color distortion may be introduced in the resulting image. Using HRNDVI minimizes this error, especially in regions with sharp edges.

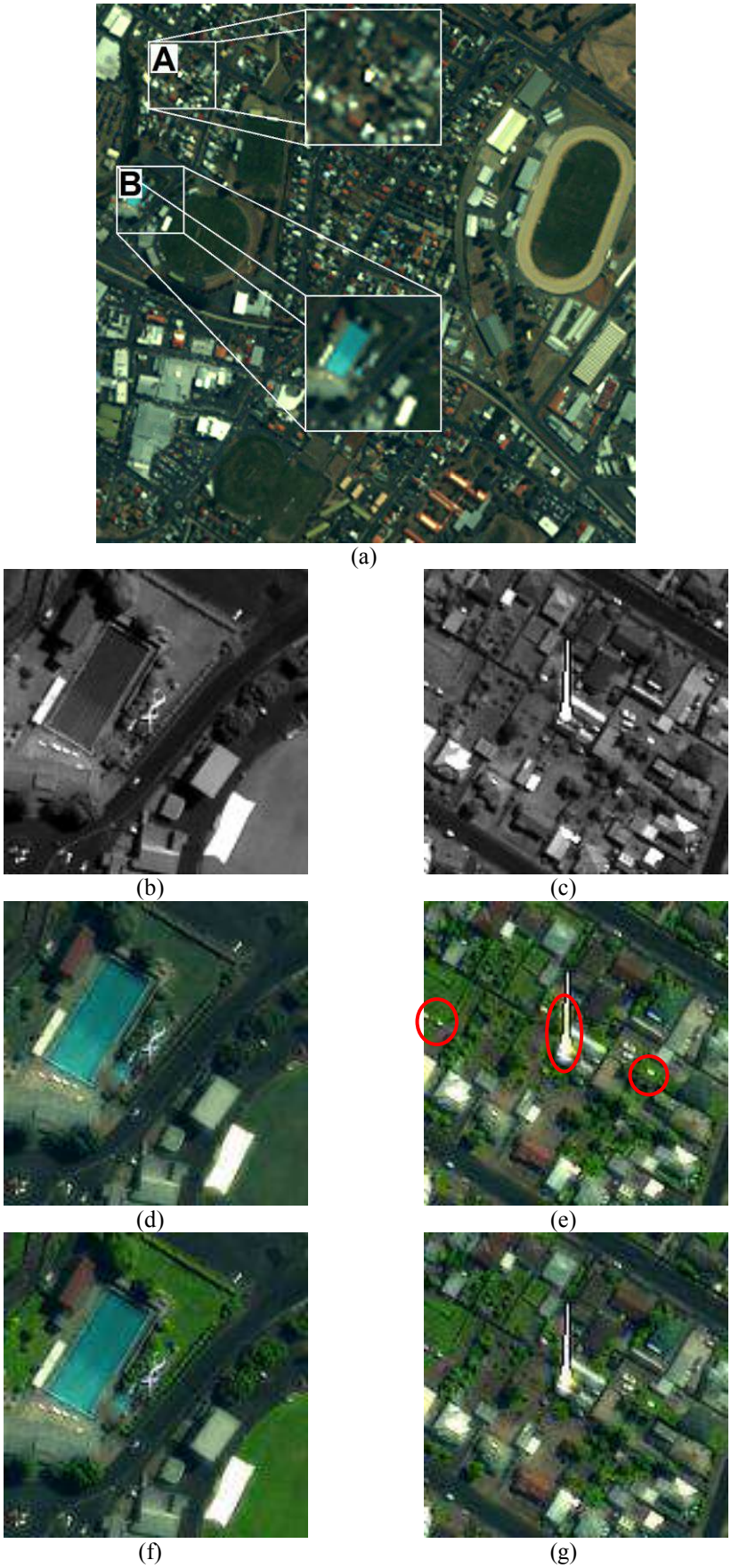


Figure 4.9 (a) RGB image with two zoomed areas, A and B. (b) Pan image for area A. (c) Pan image for area B. (d) Proposed method results with $\beta_2$, using NDVI. (e) Proposed method results with $\beta_1$, using HR NDVI. (f) and (g) Proposed method results with $\beta_2$, using HR NDVI.

#### 4.2.3.6 Conclusion

The proposed algorithm 2 can be used for both image fusion and vegetation visualization. It is based on GIHS with some G and B bands enhancement in the vegetated zones. In this context, a modified vegetation index (HRNDVI) is proposed for better vegetation detection. This technique has been evaluated both subjectively and objectively, and has been proven efficient in the process of pansharpening Ikonos images. For that, most classical evaluation indexes were used to assess the quality of the resulting images. Experimental results show that the method performs well on the images containing mixed or mostly vegetated areas. The results were then compared with those obtained from other existing approaches. This comparison clearly shows that Method 2 gives very good visual results and produces non-distorted and perfectly natural image colors. Moreover, in terms of quantitative indexes, this approach provides a global appreciable fusion quality and improves the spectral and spatial correlations in dense vegetation images. In addition of its performance, algorithm 2 still remains as simple as the other IHS based techniques.

# 4.3 Part2:

# Proposed NSCT-based pansharpening method

Up to now, a large collection of pansharpening methods have been proposed to improve the MS images to higher resolutions using spatial information of the Pan images. Several pansharpening methods are based on multiresolution approaches of the Laplacian pyramid, wavelet and contourlet transforms. The wavelet transform was a popular choice for pansharpening, but it is shown that the contourlet transform is a better transformation approach for pansharpening [77]. Moreover, the NSCT transform is very efficient in representing the directional information and capturing intrinsic geometrical structures of the objects. It has characteristics of high multiresolution, shift-invariance and high directionality. In the multiresolution-based pansharpening the number of decomposition levels for MS images is usually identical to that of the Pan images. However, when using Multiresolution analysis in pansharpening, a low number of decomposition levels preserves better the spectral quality while a high number of decomposition levels is recommended to maintain the spatial quality.

In this section, an NSCT based pansharpening method is considered and optimized using an adequate number of decomposition levels. A low number of levels is used for MS images while a high number is used for Pan images relatively to the ratio of the Pan pixel size to the MS pixel size. This keeps both spectral and spatial qualities. In addition, both the classical scheme and the hybrid scheme using the PCA transform are evaluated. Experiments conducted on QuickBird and WorldView-2 datasets show that the proposed method improves spectral quality and while keeping spatial information unchanged.

### 4.3.1 Standard PCA-Based pansharpening

The PCA transform is commonly used in signal processing, statistics and for spectral transformation to produce uncorrelated components. It is assumed that the first principal component, PC1, collects the information that is common to all input data to PCA, i.e., the spatial information, while the spectral information is captured in the other principal components [3]. The Pan image is histogram-matched with PC1 before substitution. The remaining PCs, considered to have band-specific information, are unaltered. Inverse PCA is performed on the modified Pan image and the PCs to obtain a high-resolution pan-sharpened image [77]. Hybrid algorithms based on PCA attempt to improve the PCA aspects by including a multiresolution transform in the pansharpening process. In this case, PC1 and the Pan image are decomposed using the

multiresolution transform. The obtained coefficients are merged and the inverse multiresolution transform is applied [77]. The results are obtained after an inverse PCA.

### 4.3.2 Contourlet-based pansharpening

Fusion techniques based on multiresolution analysis use multi-scale decomposition methods to decompose MS and Pan images, and then inject the spatial details contained in Pan but missing in MS into MS images. The wavelet transform fusion methods are used to control the trade-off between the spectral and the spatial information delivered from an MS sensor and the Pan one, respectively. A large number of methods had been proposed for wavelets [129]. However it was proven that the contourlet transform is a better approach than the wavelet one for pansharpening [77]. The nonsubsampled contourlet Transform (NSCT) provides a complete shift invariant and multiscale representation. NSCT is obtained via a two-stage non shift-invariant process [61]. The first stage achieves the multiscale property, while the second one provides directionality information. Both stages of NSCT are constructed to be invertible to have an overall invertible system. Figure 4.10 shows an overview of the NSCT transform [61].

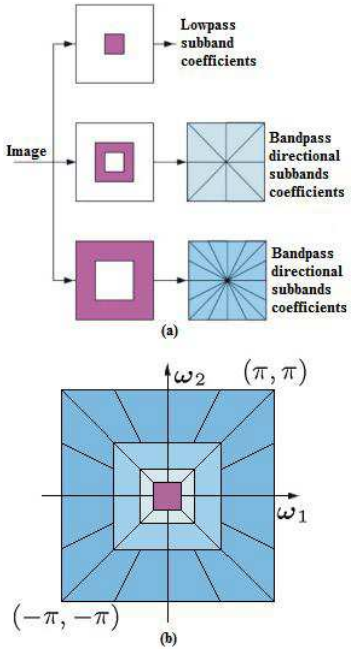


Figure 4.10 Nonsubsampled contourlet transform. (a) Implementation of NSCT. (b) Frequency partitioning in idealized form.

In general, all the multiresolution-based pansharpening methods adopt the following process [3]:

1. Forward transform the Pan and MS images using a sub-band and directional decomposition such as the subsampled or non-subsampled wavelet or contourlet transform.
2. Apply a fusion rule onto the transform coefficients.
3. Generate the pan-sharpened image by performing the inverse transform.

A number of pansharpening methods using the contourlet transform have been proposed [77]. Usually, MS and Pan images are decomposed using the same number of decomposition levels, then appropriate rules are applied to fuse the obtained coefficients. However, a lower number of decomposition levels preserves better the spectral quality while a higher number of decomposition levels is recommended to maintain the spatial quality [164]. For QuickBird or WorldView-2 the ratio of the Pan pixel size to the MS pixel size is equal to 4. This means that MS images need upsampling before doing pansharpening. Moreover, the multiresolution decomposition down-samples the image at each level. From these observations, we propose to use the NSCT-based pansharpening with a dynamic number of decomposition levels. A resolution ratio of 4 corresponds to two levels of multiresolution decomposition. When ***n*** decomposition levels are used for MS images ***n+2*** decomposition levels are used for Pan images.

The conducted experiments show that a fixed value of 1 for the MS decomposition levels (***n=1***) is practical and provides good results. Figure 4.11 shows the process of pansharpening.

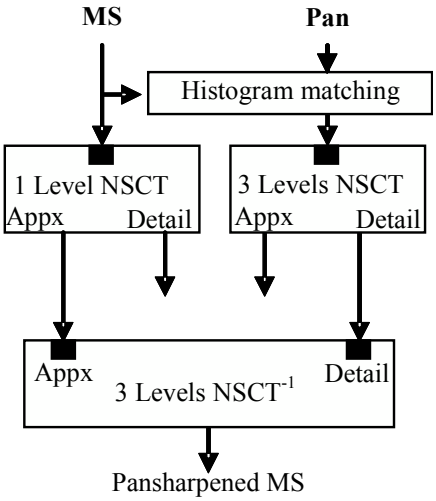


Figure 4.11 Bloc diagram of the NSCT pansharpening scheme using different numbers of decomposition levels for MS and Pan images.

Three levels of the NSCT decomposition are applied to the histogram-matched Pan image in contrast to the MS images where only one level is used. The approximation coefficients of the MS and the Pan detailed coefficients are merged to obtain the pan-sharpened image by taking the three level inverse NSCT transform.

### 4.3.3 Experimental results

The quality assessment of the pansharpened MS images presents a problem since no reference image exists at the pan-sharpened resolution. Invariably one must downsample the pan-sharpened image to the original multispectral resolution, which allows direct computation of the quality index [188]. In this work, we have selected the following metrics for assessing the quality of the obtained results, the correlation coefficient (CC) and the correlation between high frequencies (CCs) [171],

the average spectral angle mapper (SAM) which computes the change in angle of spectral vectors [159], the Spectral Information Divergence (SID) which considers each pixel spectrum as a random variable and then measures the discrepancy of probabilistic behaviour between spectra [79], the relative dimensionless global error in synthesis (ERGAS) that provides a single quantity synthesizing the quality of the fused data set [130], and finally the universal image quality index (Q4) which models any distortion as a combination of three different factors: loss of correlation, luminance distortion, and contrast distortion [158].

The proposed method is evaluated on a dataset acquired by QuickBird, and WorldView-2 provided for the 2012 IEEE GRSS Data Fusion Contest: Multimodal/multi-temporal fusion. For the MS images of WorldView-2, only four bands are used: B5, B3, B2 and B7. Pan and MS images of 2048x2048 and 512x512 pixels, respectively, are selected for the demonstration purposes. NSCT using the same number of decomposition levels for both MS and Pan images is noted NSCT1, while NSCT2 refers to the NSCT with a different number of decomposition levels. NSCT-based pansharpening is evaluated in the classical scheme and the hybrid scheme using PCA. The conducted experiments show that: applying three levels of decomposition to the Pan image provides good visual quality. Visually, in Figure 4.12 and Figure 4.13, the images obtained using NSCT1 and NSCT2 appear similar, there are no major differences. However, the quality metrics, given in Tables 4.5 and 4.6, show an improvement of the obtained results using NSCT2 compared with those obtained using NSCT1 for all metrics.

| | / | NSCT1 | NSCT1 | NSCT2 | NSCT2 |
|---|---|---|---|---|---|
| | PCA | / | PCA | / | PCA |
| CC | 0,910 | 0,948 | 0,955 | 0,956 | **0,961** |
| sCC | 0,595 | 0,613 | 0,674 | 0,654 | **0,706** |
| SAM | 4,199 | 4,700 | 3,334 | 4,400 | **3,250** |
| SID | 0,057 | 0,101 | 0,081 | 0,103 | **0,087** |
| ERGAS | 7,613 | 5,681 | 5,292 | 5,233 | **4,886** |
| Q4 | 0,837 | 0,907 | 0,922 | 0,922 | **0,934** |

Table 4.5 QuickBird: Average quality indices between the original MS and the fused images.

| | / | NSCT1 | NSCT1 | NSCT2 | NSCT2 |
|---|---|---|---|---|---|
| | PCA | / | PCA | / | PCA |
| CC | 0,951 | 0,960 | 0,969 | 0,966 | **0,972** |
| sCC | 0,909 | 0,845 | 0,913 | 0,855 | **0,914** |
| SAM | 4,052 | 4,374 | 3,128 | 4,116 | **3,035** |
| SID | 0,079 | 0,035 | 0,031 | 0,032 | **0,025** |
| ERGAS | 4,698 | 4,130 | 3,744 | 3,761 | **3,440** |
| Q4 | 0,886 | 0,914 | 0,934 | 0,928 | **0,944** |

Table 4.6 WorldView-2: Average quality indices between the original MS and the fused images.

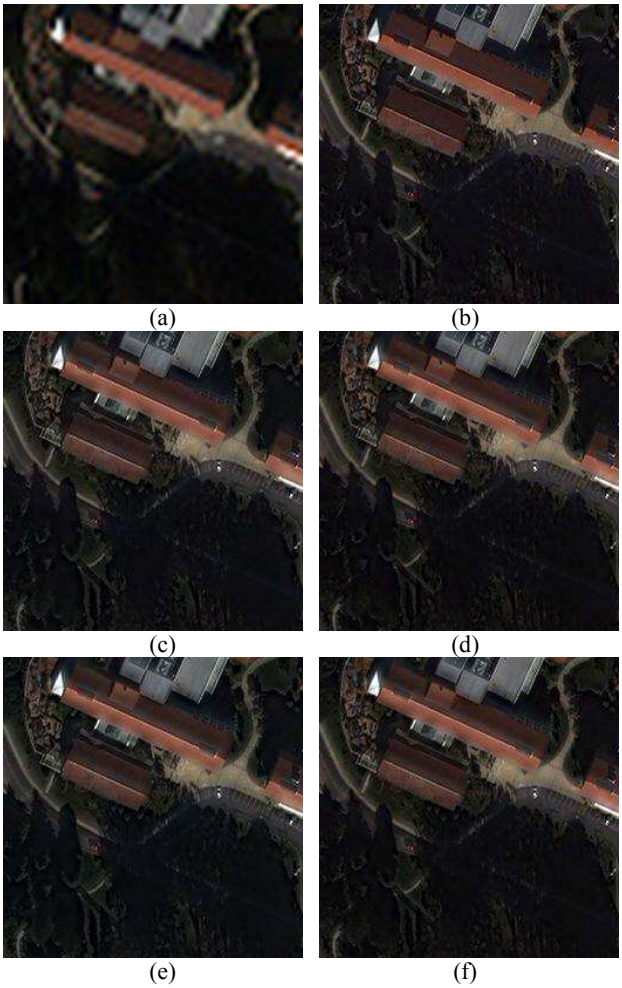


Figure 4.12 Pan-sharpened QuickBird: 256×256. (a) upsampled MS, (b) PCA,(c) NSCT, (d) PCA-NSCT, (e) New NSCT, (f) New NSCT PCA

The use of a low number of decomposition levels (one) for MS images and a high one (three) for the Pan image has a significant positive impact on the pan-sharpened images. Moreover, in case of images with a lot of vegetation, the carried research shows that the use of PCA produces some color distortion in the vegetated areas mainly for WorldView-2 images. In this case the classical scheme is more attractive than the PCA hybrid scheme. The idea of the dynamic number of decomposition levels seems to outperform the fixed number of decomposition levels approach.

The 2012 IEEE GRSS Data Fusion Contest was organized by the Data Fusion Technical Committee (DFTC) of the Geoscience and Remote Sensing Society (GRSS) of the International Institute of Electrical and Electronic Engineers (IEEE). More than 1150 researchers across the globe registered for the contest and the data set was downloaded from 78 different countries. The presented work was selected to be among the 10 best submitted papers. The final results are published on the page web: http://www.grss-ieee.org/community/technical-committees/data-fusion/data-fusion-contest/

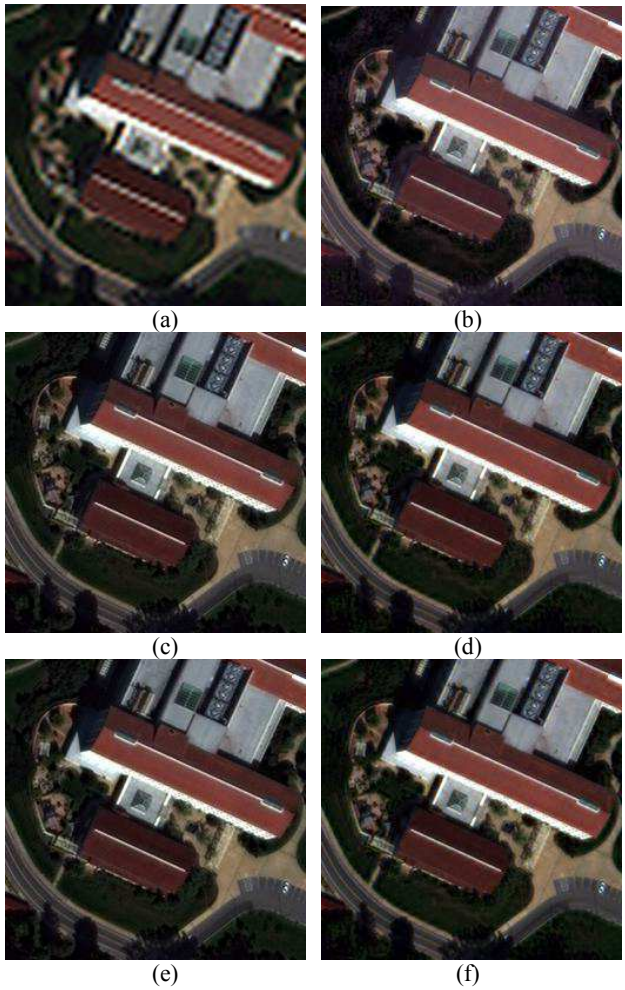


Figure 4.13 Pan-sharpened WorldView-2: 256×256. (a) upsampled MS, (b) PCA,(c) NSCT, (d) PCA-NSCT, (e) New NSCT, (f) New NSCT PCA

### 4.3.4 Conclusion

In this section, the NSCT-based pansharpening methods in their classical forms as well as in their hybrid forms using PCA are considered. The improvement of the NSCT-based image pansharpening is assured by using a low number of decomposition levels for MS images and a high number of decomposition levels for the Pan image. This strategy allows getting satisfying visual and quantitative results. The spectral quality of MS images is better preserved when a lower number of decomposition levels is used, in contrast, this number must be higher to preserve the spatial quality of the Pan image in the pansharpened images.

The performance of the proposed strategy is tested on QuickBird and WroldView-2 data. The obtained results confirm the added-value of using an adequate number of decomposition levels.

# 4.4 Part3:

# Proposed vegetation extraction method

Nowadays, the technologies and methods for spaceborne remote sensing have evolved dramatically to include a suite of sensors operating at a wide range of imaging scales with potential interest and importance to planners and land managers [178]. Very high resolution satellite remote sensing systems are now capable of providing imagery with similar spatial detail to aerial photography. However, a comparison between the two image types suggests that the use of satellite images is much more cost effective than aerial photographs for urban vegetation monitoring over large areas [180]. Satellite data provide valuable information for mapping vegetation and monitoring vegetation change [181]. Vegetation can be distinguished from most other materials by virtue of its notable absorption in the red and blue segments of the visible spectrum, its higher green reflectance and, especially, its very strong reflectance in the near infrared. The near infrared is the most sensitive spectral domain used to map vegetation canopy properties and may improve the discrimination of vegetation surfaces [176]. Many vegetation indices have been developed primarily based on the feature of low red and high near-infrared reflectance: the most widely used index being NDVI [182].

In case of urban environment, vegetation maps derived from moderate resolution imagery (e.g., MODIS) fail to detect the scattered trees and fragmented grass that are indiscernible at this resolution. Since the resolution of the vegetation index is dependent upon that of the retrieved image, high-resolution imagery from the Ikonos satellite and similar high spatial resolution sensors (e.g., Quickbird, Worldview) may be useful for informing many resource management applications. The Ikonos sensors produce four MS bands and one Pan band of 4-m and 1-m resolutions, respectively as shown in Figure 1.15. Ikonos data has an extremely wide range of applications extending from archaeological and geological research to urban planning, environmental monitoring and fishing conservation, to agriculture and vegetation, and military to zoology. It is a valuable resource for achieving map accuracies comparable to those of manual aerial photo interpretation and can aid in the development of a wide range of mapping and spatial modeling applications [183].

In an urban environment, the presence, abundance and life form of vegetation have long been considered as an important factor influencing the environment quality, conferring diverse benefits [182]. Vegetation is generally considered a key component of the urban environment. However, the

urban environment is complex and very different from rural and natural environment [183]. Increasing demands on the accuracy and thematic resolution of vegetation area species maps from satellite imagery has created a need for novel image analysis techniques [184]. These studies have investigated the possibility of using Ikonos MS images to quantify urban vegetation, in some cases obtaining accuracy similar to that achieved from aerial photographs [180].

The NDVI index is generally used for vegetation extraction applications consisting of differentiating between vegetation and other surface types. However, in some cases, NDVI fails in the detection process. In recent studies [185] and [78], alternative vegetation indices and extraction applications are proposed. In [185], the authors presented a fixed-threshold vegetation index ($VTC_{map}$) based on the extended Tasseled Cap Transformation (TCT). A resulting low resolution vegetation map is obtained from MS images, and resized to the same pixel size as that of the Pan image by using the cubic convolution. It is then combined with the Pan image using the IHS fusion method, in order to produce high resolution vegetation maps. Unlike this index, which is based on the MS images only, the authors in [78] used Pan images to determine their proposed vegetation index ($VI_{TU}$) for Ikonos and QuickBird satellites. These two methods are globally adequate, but in some cases, like urban environment, they fail in the vegetation extraction.

In this section, we propose a method to differentiate between vegetation and the other surface types when using Ikonos imagery. Moreover, the interpolation method used to up-sample the MS images was chosen in order to preserve the edges, making the vegetation extraction more accurate in the urban areas.

### 4.4.1 Existing methods for vegetation extraction for Ikonos imagery

Vegetation extraction is an important application that is used to monitor crops in terms of identity, health and stage of growth. In [185], a fixed threshold approach generating high-resolution vegetation maps for Ikonos imagery was proposed. In this technique an extended TCT is used to produce the vegetation map, and then a high-resolution version of this map is obtained after a FIHS fusion method [72]. The Tasseled Cap Transformation vegetation index ($VI_{TC}$) was derived as:

$$VI_{TC} = \frac{1}{2}TC_2 - \frac{1}{4}TC_1 - \frac{1}{4}TC_3 , \tag{4.33}$$

where the Ikonos TCT coefficients [186] are given by:

$$\begin{aligned} TC_1 &= +0.326B \quad +0.509G \quad +0.560R \quad +0.567NIR \\ TC_2 &= -0.311B \quad -0.356G \quad -0.325R \quad +0.819NIR \\ TC_3 &= -0.612B \quad -0.312G \quad +0.722R \quad -0.081NIR \end{aligned} \tag{4.34}$$

with R, G, B and NIR are the digital numbers representing the retrieved reflectance for an individual pixel of the red, green, blue and near infrared bands, respectively. The vegetation index,

$VI_{TC}$, given in equation (4.33) is derived from emphasizing the second component ($TC_2$) and depressing the other two components [185].

Rewriting equation (4.33) using equation (4.34), gives

$$VI_{TC} \cong 0.29NIR - 0.48R - 0.08B - 0.23G \tag{4.35}$$

The vegetation map $VTC_{map}$ is then produced by thresholding $VI_{TC}$:

$$VTC_{map} = \begin{cases} VI_{TC}, & if\ VI_{TC} \geq 0 \\ 0, & otherwise \end{cases} \tag{4.36}$$

As reported by the authors in [185], the threshold is experimentally set at the fixed value of zero. All $VI_{TC}$ values, above this threshold, correspond to the vegetation information; on the other hand the values below this threshold represent all non-vegetation information.

When using the FIHS fusion method [72], the fused image is obtained by adding to each MS band, resized up to the same pixel size as the Pan image, the same amount representing the difference between the Pan image and the Intensity (I) component, where I represents the mean of the MS band. By adopting the FIHS technique, a high spatial resolution vegetation map is generated in [185]. The low resolution $VTC_{map}$ is resized up to an image $VTC'_{map}$ with the same spatial resolution as the Pan image by using the cubic interpolation. Hence, an RGB pseudo color image T can be formed as T=[0, $VTC'_{map}$,0], where $VTC'_{map}$ represents the green band of T, and the 0 represents a full black image in the red or blue band. Then, T is fused with the Pan image using the FIHS method. Each band of T is increased by the same amount δ, representing the difference between the Pan image and the mean of the pseudo color image T. The obtained three band vegetation map $HR\_VTC_{map}$ is given by:

$$HR\_VTC_{map} = \begin{bmatrix} \delta \\ \delta + VTC'_{map} \\ \delta \end{bmatrix}, \text{ where } \delta = Pan - \frac{1}{3}VTC'_{map} \tag{4.37}$$

Generally, vegetation indices take advantage of the fact that the red edge falls between the red and NIR bands. However, in a recent study [78], the authors claim that the digital number (DN) values of vegetation in the Pan are much greater than those of the intensity (I) component. Hence, the difference (Pan-I) DN's values is used to develop a new vegetation index. This was proposed in [78] for the vegetation layer of GIS and military applications as camouflage and is expressed as ($VI_{TU}$):

$$VI_{TU} = \frac{Pan - I_3}{Pan + I_3} \tag{4.38}$$

where $I_3$=(R'+G'+B')/3 with [R',G',B'] obtained by up-sampling the original [R,G,B] image up to the same spatial resolution as that of the Pan image, using the cubic interpolation.

The $VI_{TU}$ index is used to produce a high spatial resolution vegetation map. This vegetation map is considered to be an RGB image, where each channel takes the same values as those of the Pan band. Then the G channel is boosted in vegetated areas delineated using $VI_{TU}$. The obtained high spatial resolution vegetation map is expressed as [78]:

$$HR\_VI_{map} = \begin{bmatrix} Pan \\ G' + \delta'_{IHS} \\ Pan \end{bmatrix}, \text{ with } \delta'_{IHS} = \begin{cases} Pan - G' & if\ VI_{TU} \le 0 \\ k(Pan - I_3) & otherwise \end{cases} \quad (4.39)$$

A flowchart is shown in Figure 4.14 to give more details.

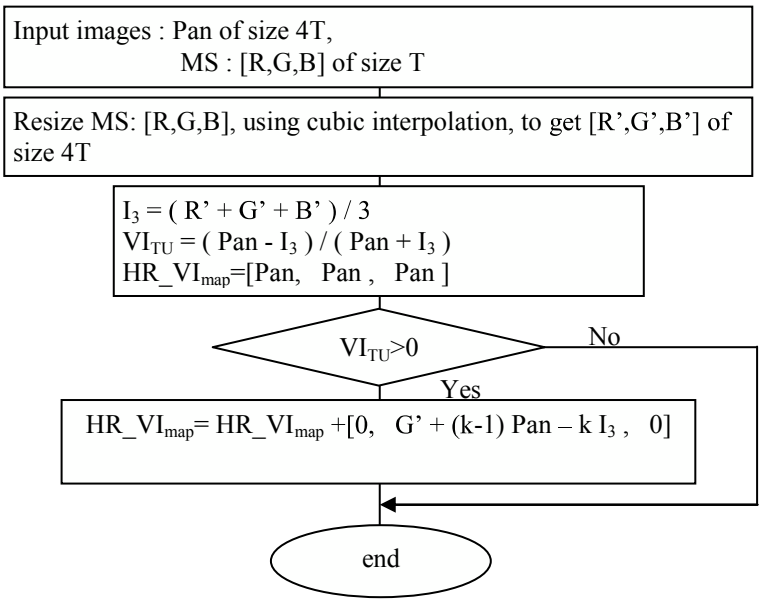


Figure 4.14 A flowchart for the algorithm presented in [78].

For the vegetation extraction, only the G band is enhanced in the vegetated areas. The fused R and B bands are taken as the Pan image. As stated by the authors in [78], the best value for parameter k was found to be equal to 2 for Ikonos images.

## 4.4.2 Vegetation extraction using the HRNDVI index

For the vegetation extraction application, HRNDVI can be used, in the same manner as VI, to produce a high spatial resolution vegetation map as:

$$HR\_HRNDVI_{map} = \begin{bmatrix} Pan \\ G' + \delta'_{IHS} \\ Pan \end{bmatrix}, \text{ with } \delta'_{IHS} = \begin{cases} Pan - G' & if\ HRNDVI \le \theta \\ k_1(Pan - I_4) & otherwise \end{cases} \quad (4.40)$$

where $I_4$=(R'+G'+B'+NIR')/4, and θ is a threshold selected manually after various experimentations. From the conducted experiments, typical values of θ range in [0.1 0.25]. The value of θ depends on the image content. When there is less vegetation in an image, a typical value is 0.15, while a typical value for dense vegetation is 0.25.

Numerous experiments were conducted to select the best parameters in order to get high-resolution vegetation mapping. Several values of $k_1$ (1, 2, 3, 4, 5 …) were tested on 132 images using $I_3$ and $I_4$. The visual analysis shows that the produced images looked blurred in the vegetated areas when $I_3$ is used and that good results are obtained when using $I_4$ with a value of 4 for $k_1$. In addition, for all of these experiments, a good value of the HRNDVI threshold is estimated to be 0.05 less than the threshold value of NDVI. Therefore, while in the case of NDVI the traditional threshold is 0.2, this one is rather found to be 0.15 in the case of HRNDVI.

The importance of using Pan images for computing the vegetation index was illustrated by the example of Figure 4.4. In Figure 4.15 the same example is used.

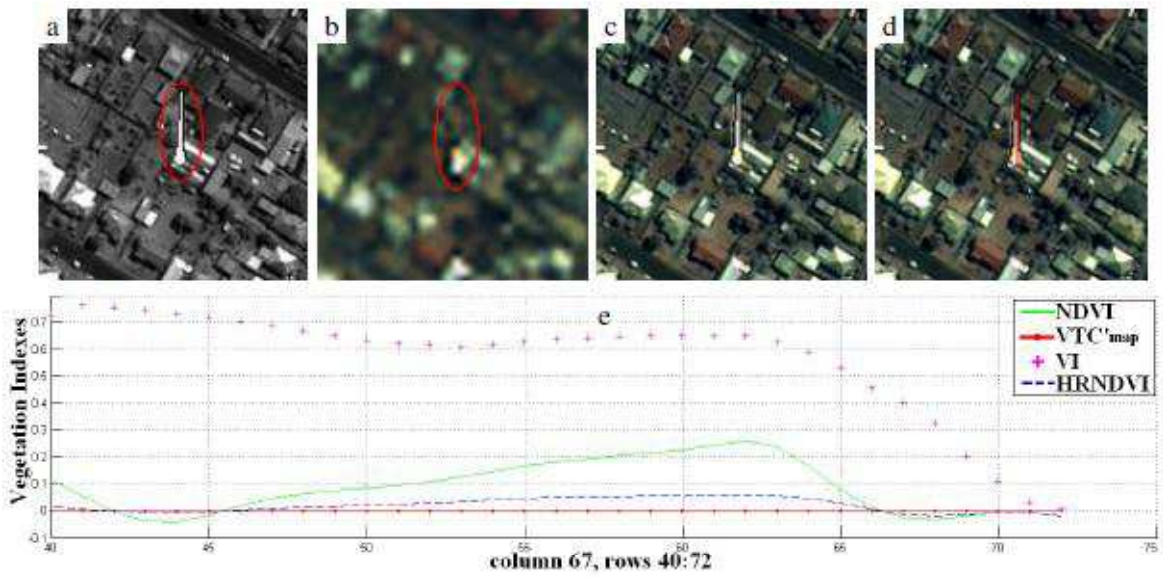


Figure 4.15 (a) Pan image, (b) RGB image, (c) GIHS fused image, (d) considered column in red color, (e) NDVI, VTC'map, VITU and HRNDVI corresponding to the red column in (d).

The only difference is that in figure (e) we have added the case of $VTC'_{map}$. All the values of the $VTC'_{map}$ are less than 0, producing a correct vegetation map for this case.

In order to evaluate the quality of the presented vegetation indices, a process of vegetation enhancement was conducted on pansharpened images. Various methods, like those presented in [78], [85], [86] and [173] make use of a modified IHS index to enhance green vegetation. The modified HIS index, enhancing vegetation, is derived as [78]:

$$\begin{bmatrix} Fused\_R \\ Fused\_G \\ Fused\_B \end{bmatrix} = \begin{bmatrix} R' + \delta_{IHS} \\ G' + \delta'_{IHS} \\ B' + \delta_{IHS} \end{bmatrix} \text{ with } \delta_{IHS} = Pan - I \text{ and } \delta'_{IHS} = \begin{cases} \delta_{IHS} & if\ VIdx \le \theta \\ \alpha\,\delta_{IHS} & otherwise \end{cases} \quad (4.41)$$

where I is the intensity component of the IHS transform and α is a constant experimentally set to define the degree of vegetation enhancement. When α is 1, there is no vegetation enhancement, this is the case of a simple fusion. Thus, to enhance the vegetated areas, α must be greater than 1.0. VIdx is the vegetation index delineating the vegetation, and θ is a threshold to be determined with respect to the used vegetation index. Equation 4.41 is a general form: three different equations can be derived when using $VTC'_{map}$, $VI_{TU}$ or HRNDVI in place of VIdx. As reported by the authors in [78] and [185], when using $VTC'_{map}$ [185] or $VI_{TU}$ [78], threshold θ is always set at the fixed value of 0. However, for the HRNDVI case, threshold θ is experimentally chosen, according to the image content as it is generally done for NDVI.

To evaluate the quality of the merged images obtained using $VTC'_{map}$, $VI_{TU}$ and HRNDVI, four quantitative evaluation indices are used [187]: ERGAS, $Q_4$, SAM and CC.

### 4.4.3 Experimental results

The same Ikonos images, used for evaluating the first algorithm, were also used to test the proposed procedure of vegetation extraction based on HRNDVI. Two subsets of images were used: the first one (I1) is mostly vegetation (around 85%) and the second one (I2) contains less vegetation (around 20%). Based on equation 4.41, we applied some vegetation enhancement using $VTC'_{map}$, $VI_{TU}$ and HRNDVI. The value of parameter α is set to 2, experimentally. When using $VTC'_{map}$ or $VI_{TU}$, threshold θ is set to 0, but it is 0.15 when HRNDVI is used. For images I1 and I2, the ideal and the measured values of the four quality indices are reported in Table 4.7.

The values of the resulting indices depend on the amount of vegetation contained in an image. In images with less vegetation (e.g. I1), there is less enhancement leading to less vegetation color changes than in images with more vegetation (e.g. I2), when compared to the original images. To demonstrate this, we select an image region, with nearly no vegetation information, and another region with dominant vegetation. The obtained results are shown in Table 4.8.

| | VIdx | ERGAS | SAM | CC | Q4 |
|---|---|---|---|---|---|
| Ideal | / | 0 | 0° | 1 | 1 |
| Image I1 | VTC'map | 15.474 | 12.472 | **0.830** | 0.108 |
| | $VI_{TU}$ | 12.33 | 13.980 | 0.751 | 0.166 |
| | HRNDVI | **10.346** | **11.854** | 0.759 | **0.225** |
| Image I2 | VTC'map | 14.726 | 7.551 | **0.893** | 0.295 |
| | $VI_{TU}$ | 9.110 | 8.338 | 0.836 | 0.587 |
| | HRNDVI | **7.339** | **6.424** | 0.885 | **0.688** |

Table 4.7 Quantitative performance evaluation for the whole images.

| | VIdx | ERGAS | SAM | CC | Q4 |
|---|---|---|---|---|---|
| Ideal | / | 0 | 0° | 1 | 1 |
| Vegetation | VTC'map | 15.380 | 12.673 | **0.804** | 0.054 |
| | $VI_{TU}$ | 12.275 | 14.034 | 0.697 | 0.089 |
| | HRNDVI | **10.207** | **11.511** | 0.723 | **0.124** |
| no vegetation | VTC'map | 14.782 | 6.211 | 0.948 | 0.374 |
| | $VI_{TU}$ | 7.093 | 5.294 | 0.946 | 0.806 |
| | HRNDVI | **6.221** | **4.150** | **0.960** | **0.843** |

Table 4.8 Quantitative performance evaluation for images with and without vegetation.

Tables 4.7 and 4.8 show that the enhancing method based on HRNDVI is characterized by less spectral distortion, in most of the cases, this method provides indeed the best quality index. Figure 4.16 shows a part from the obtained results of enhancement of pansharpened images using VTC'map, $VI_{TU}$ and HRNDVI. Moreover, the original RGB image, the Pan image and the IHS fused image are given for comparison purposes.

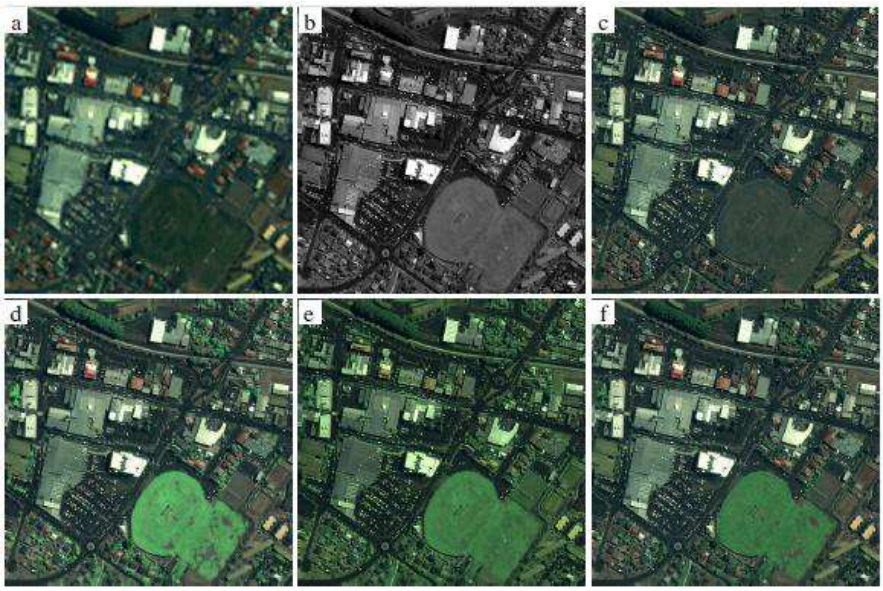


Figure 4.16 enhancement of pan-sharpened images : (a) up-sampled original RGB image, (b) Pan image, (c) IHS fused image, (d) IHS fused image enhanced using VTC'map, (e) IHS fused image enhanced using VITU, (f) IHS fused image enhanced using HRNDVI.

For visual comparison purposes, we consider the vegetation map, given by equations 4.36, 4.38 and 4.25, and their application to vegetation extraction, expressed in equations 4.37, 4.39 and 4.40, respectively. The obtained results are shown in Figure 4.17 and Figure 4.18 for the mostly vegetation and the less vegetation cases, respectively. Figure 4.17(a) and Figure 4.18(a) show that the VTC'$_{map}$ produces low-resolution maps. Moreover, as can be observed visually on Figure 4.19 (white ellipses), some vegetation areas are missing in the vegetation detection process.

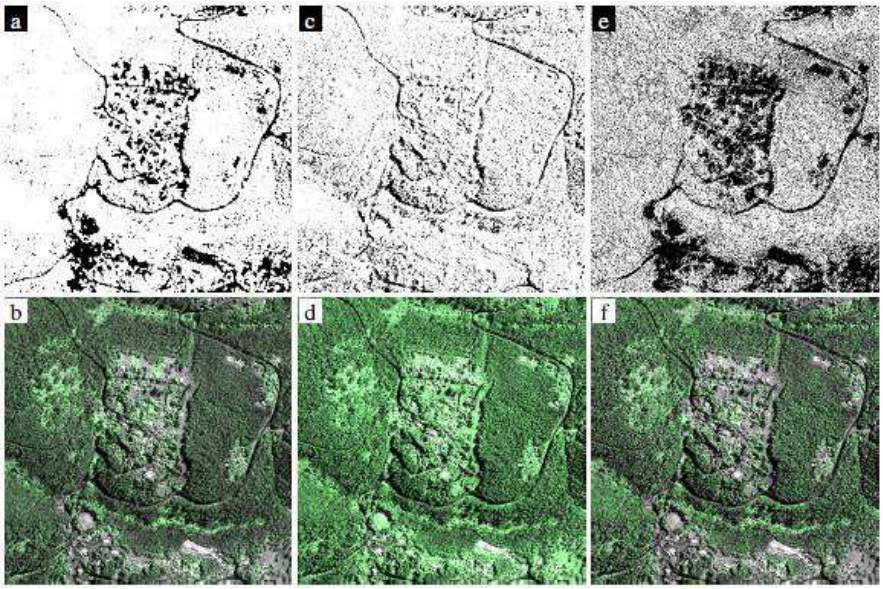


Figure 4.17 The vegetation map and extraction of I1: (a) VTC'map map, (b) extraction using VTC'map, (c) VITU map, (d) extraction using VITU, (e) HRNDVI map, (f) extraction using HRNDVI.

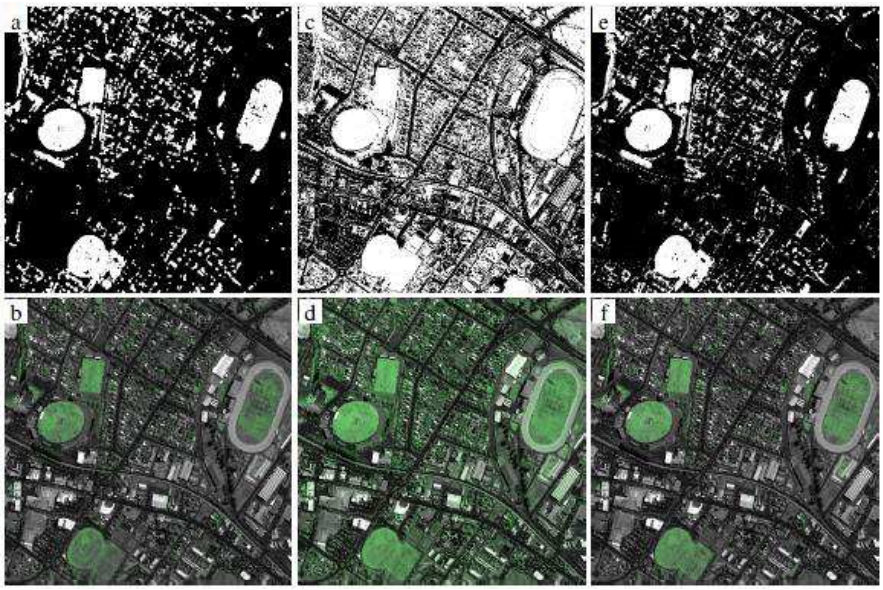


Figure 4.18 The vegetation map and extraction of I2: (a) VTC'map, (b) extraction using VTC'map, (c) VITU map, (d) extraction using VITU, (e) HRNDVI map, (f) extraction using HRNDVI.

For the $VI_{TU}$ index, the obtained maps of Figure 4.17(c) and Figure 4.18(c) illustrate an overestimation of vegetation (see red ellipses on Figure 4.19 and Figure 4.20), due to the large difference between the Pan image and the $I_3$ component in non vegetated areas.

Results presented in Figure 4.17(e) and Figure 4.18(e), indicate that those based on the modified NDVI index are more accurate in comparison with those derived from the two other methods presented in Figure 4.17(a), Figure 4.17 (c) and Figure 4.18(a), Figure 4.18(c). Hence, HRNDVI is

a good solution to introduce high-resolution information in the vegetated areas. The rest of the images Figure 4.17(b), Figure 4.17(d), Figure 4.17(f) and Figure 4.18(b), Figure 4.18(d), Figure 4.18(f) correspond to the vegetation extraction application using $VTC'_{map}$, $VI_{TU}$ and HRNDVI, respectively.

For a better illustration, zoomed areas are considered in Figure 4.19 and Figure 4.20. In Figure 4.19(a), compared to Figure 4.19(c), the white ellipse shows a non-detected vegetation area, whereas the red ellipse in Figure 4.19(b) shows a false alarm vegetation area.

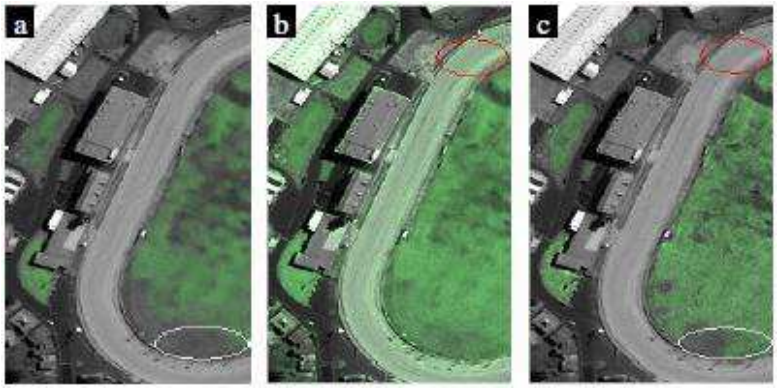


Figure 4.19 The vegetation extraction sample 1: (a) extraction using VTC'map, (b) extraction using VITU, (c) extraction using HRNDVI.

Equation (4.35) shows that the TCT vegetation index ($VI_{TC}$) is based on the low-resolution MS images only. Hence, $VTC'_{map}$ will be of the same resolution, producing a low-resolution vegetation map. The amount of the high spatial resolution added to the G band in equation (4.37) is not significant enough to enhance the spatial resolution of the vegetation zones. The extracted vegetation shown in Figure 4.20 demonstrates that using $VTC'_{map}$ produces blurred vegetation areas, while using the $VI_{TU}$ index introduces errors by considering some non-vegetation areas as vegetation.

HRNDVI, presented in Figure 4.20(c) is more accurate and can be considered as a trade-off between VTC'map and the VITU indices.

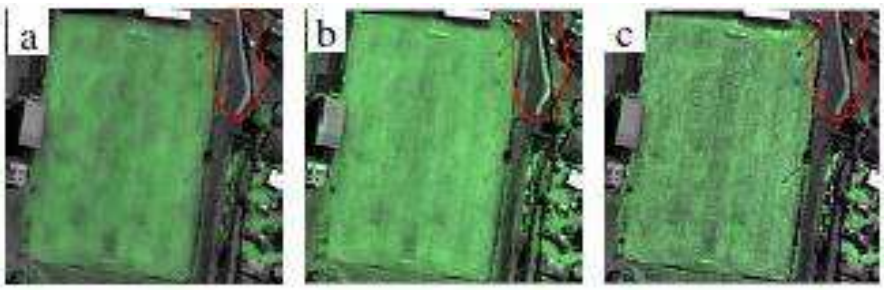


Figure 4.20 The vegetation extraction sample 2: (a) extraction using VTC'map, (b) extraction using VITU, (c) extraction using HRNDVI.

### 4.4.4 Conclusion

In this section, several methods used to extract and map vegetation in Ikonos imagery are presented. Then a new method is proposed to reduce some problems associated with the under and over estimation of vegetation and with the resolution characteristics of the extracted areas. It is shown that HRNDVI can provide a high resolution vegetation mapping. Hence, the extracted images are more accurate especially in the urban area. The proposed technique has been evaluated objectively, and has been proven efficient. The obtained results, compared to those reported for some existing methods; show that the proposed method yields accurate vegetation extraction and high resolution characteristics of the corresponding mapping.

# 4.5 Conclusion

In this chapter, we have presented our main contributions in pansharpening and vegetation extraction domains. For pansharpening, two proposed methods are based on the IHS transform, while another method is based on the NSCT transform. The two proposed IHS based methods boost the Green band in the vegetation areas in order to amplify the Intensity grey values. The fusion of the Pan and enhanced Intensity image produces a reduced distortion in MS color images. The proposed NSCT based pansharpening method uses a low number of decomposition levels for the MS images and a high number of decomposition levels for the Pan image. This strategy allows getting satisfying visual and quantitative results. The spectral quality of MS is better preserved when a lower number of decomposition levels is used, in contrast, this number must be higher to preserve the spatial quality of the Pan image in the pansharpened images.

Furthermore, a new vegetation index, HRNDVI, for high resolution images was developed. Thus allowed the proposition of a technique for vegetation extraction from Ikonos images, in urban area. It is shown that HRNDVI can provide a high resolution vegetation mapping. Hence, the extracted images are more accurate especially in the urban area.

All the proposed methods were tested on high resolution images as those issued from Ikonos, QuickBird or WorldView-2. They were, also, compared to existing methods to show their effectiveness. Evaluation was driven quantitatively and qualitatively and this showed higher performance for proposed methods.

It is to note that when we examined the assessment tools currently used we found that more attention is given to the spectral quality than the spatial one. So for that, we proposed a new protocol to equilibrate both qualities. This is presented in the next chapter.

# 5

# Contribution to objective quality assessment

## 5.1 Introduction

In the previous chapter, three algorithms for pansharpening were proposed. We have used visual analysis conjointly with quantitative assessment. During experiments, in some cases, the obtained pansharpened images look blurry; however, the corresponding quantitative analysis state that they were good: disagreement! We believe that it is due to the nature of the realized measure of the indices. Nearly all the used metrics consider the spectral characteristics of the images more than the spatial ones. In addition, just a few quantitative metrics have been found in the literature to evaluate the spatial quality. The objective of this chapter is to present a solution to this disagreement, through a protocol for pansharpening evaluation; where both the spectral and spatial aspects will be considered. Many assessment indices can be introduced in this protocol, under some assumptions.

Various quality indexes, as those presented in chapter 3, are available to evaluate pansharpening methods. Assessment, between each fused and reference MS band, is possible by using the correlation coefficient (CC), the bias, the difference in variance (VAR), the standard deviation of the differences on a pixel basis (SD), and the correlation between high frequencies (sCC). Moreover, a global evaluation can be done using the average root mean square error, the universal quality index (Q4), the spectral angle mapper (SAM) and the relative dimensionless global error in synthesis (ERGAS) [187]. These indexes can be classified into two groups: spectral and spatial. Often, the pansharpened results are assessed using indexes based mainly on the spectral similarity. Hence, the presented metrics results tend to favor those methods improving the spectral quality. However, the spatial quality is important too. The authors in [187] recommended the use of nine

indexes in pansharpening evaluation, where only one index is considered to assess the spatial quality.

Here, to illustrate and introduce the importance of the choice of the quality indexes: two fusion methods are considered the standard PCA based pansharpening [77] and wavelet (WAV) [129] fusion method.

Results obtained from the PCA and wavelet fusion methods are shown in Figure 5.1. The original MS and Pan images are given in upper left and upper right corners of Figure 5.1, respectively. The fused images, obtained using PCA and wavelet are shown in the lower left and lower right corners of Figure 5.1, respectively. Moreover, the most important indexes, as recommended in [187], are given in table 5.1.

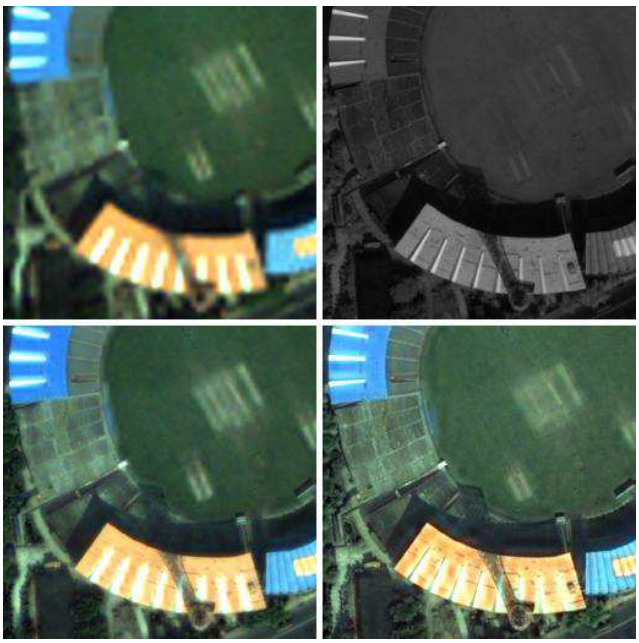

Figure 5.1 Top left: MS, top right: Pan, bottom left: PCA pansharpened, bottom right: wavelet pansharpened.

| | **CC** | **VAR** | **SD** | **sCC** | **$Q_4$** | **ERGAS** | **SAM** |
|---|---|---|---|---|---|---|---|
| PCA | **0.95** | 0.48 | **0.05** | **0.86** | **0.88** | **1.71** | **2.51** |
| WAV | 0.90 | **0.34** | 0.07 | 0.82 | 0.81 | 2.01 | 3.11 |

Table 5.1 metrics comparison between PCA and wavelet fusion methods.

When comparing the PCA and wavelet fusion methods based only on the metrics of Table 5.1, it appears that PCA is more valuable than wavelet, however, visual results, given in Figure 5.1, are not coherent with this conclusion.

Visually it appears that, in addition to preserving the original colors, wavelet results are more accurate for spatial information representation. Hence for assessing fusion techniques, the choice of

indexes usually consistent with the visual results is crucial. In this chapter, we propose an evaluation protocol to assess pansharpening methods. Both spectral and spatial qualities are considered. This protocol will be helpful when a ranking of several techniques is to be accomplished.

## 5.2 Protocol Description

In general, most authors present their quantitative evaluation of the various methods in tables. Then they must add text to classify these methods. Our objective is to find a way to give, in the same table, both metrics and ranking methods in order to facilitate the author's explanation and reader's understanding. This method can also be used during experimentations of fusion techniques for assessment of their results and comparison with other approaches. Thus it can reduce the visual evaluation or help to reduce it.

To assess M fusion methods, let $K_1$ and $K_2$ be, respectively, the numbers of the spectral and the spatial metrics to be used for the assessment. The experiments are achieved on N images. For each image, two tables of size ($K_1$xM) and ($K_2$xM), corresponding to spectral and spatial metrics respectively, are used for presenting the results. As shown in Figure 5.2, each table component is represented as $C_m^n(k)$, where $m \in \{1,2,\cdots,M\}$, $n \in \{1,2,\cdots,N\}$, $k \in \{1,2,\cdots,K_1\}$ for spectral metrics and $k \in \{1,2,\cdots,K_2\}$ for spatial metrics.

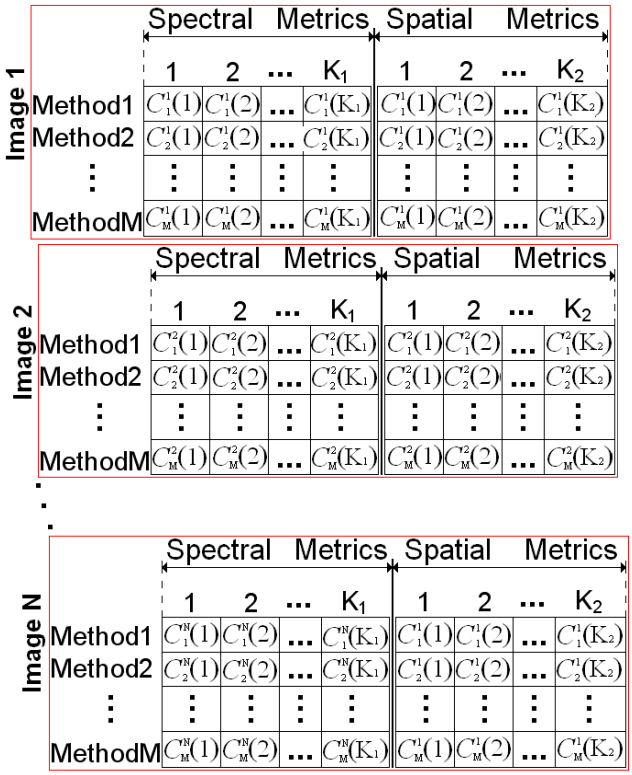


Figure 5.2 Spectral and spatial tables structure.

For the i[th] image and k[th] metric, a column $v^i(k)$ is constructed as $v^i(k)=\left\{C_1^i(k),C_2^i(k),\cdots,C_M^i(k)\right\}$, where the M components correspond to the M values obtained for the M methods to be evaluated, respectively.

At first, for each metric, the methods are sorted into two classes: satisfying and non-satisfying methods, based on a fixed metric threshold. As a simple case, the metric threshold can be chosen as being the mean value of column $v^i(k)$ i.e. ($\mu_{ik}$). However, for more reliability, we consider also the standard deviation of column $v^i(k)$ i.e. ($\sigma_{ik}$). Each metric has an ideal value which is considered in the classification of the methods. Generally, the ideal values are zero (0) or one (1), depending on the type of the metric. Hence, the way of combining $\sigma_{ik}$ with $\mu_{ik}$ depends on the ideal value of the corresponding metric. For each metric, a threshold ($\theta_{ik}$) is defined as:

$$\theta_{ik}=\mu_{ik}\pm\alpha\sigma_{ik} \tag{5.1}$$

where $\alpha$ is a value to be chosen experimentally. In this equation, $\alpha\sigma_{ik}$ is added to $\mu_{ik}$ if the optimal value of the corresponding metric is 1, and is subtracted from $\mu_{ik}$ if the optimal value is 0. Then we use a simple statistical concept, based on logical values (0,1), to decide if a method is satisfactory or not. Using the i[th] image, a method (m) is considered satisfactory in terms of the k[th] metric if its value is greater than the corresponding threshold and "1" is assigned to this method, otherwise "0" will be assigned to it. For metrics with an optimal value of 1, the obtained results are expressed as:

$$B_m^i(k)=\begin{cases}1 & if\ C_m^i(k)\geq\theta_{ik}\\ 0 & otherwise\end{cases} \tag{5.2}$$

In contrast, for the metrics with an optimal value of 0, the expression should be as:

$$B_m^i(k)=\begin{cases}1 & if\ C_m^i(k)\leq\theta_{ik}\\ 0 & otherwise\end{cases} \tag{5.3}$$

Hence, for N images, one obtains N spectral tables and N spatial tables of values 1 and 0. Then both N tables are summed. This will produce two tables corresponding to the spectral and spatial metrics. Each component (A(m,k)) of these resulting tables is expressed as:

$$A(m,k)=\sum_{i=1}^{N}B_m^i(k) \tag{5.4}$$

After that, the columns of the spectral table and the spatial table are summed too. This will produce two columns characterizing the spectral and spatial indices: $QI_{spec}$ and $QI_{spat}$. Each component of these two columns can be expressed as:

$$\sum_{k=1}^{K}A(m,k)=\sum_{k=1}^{K}\sum_{i=1}^{N}B_m^i(k) \tag{5.5}$$

Hence:

$$QI_{spec} = \left\{ \sum_{k=1}^{K_1} \sum_{i=1}^{N} B_1^i(k), \sum_{k=1}^{K_1} \sum_{i=1}^{N} B_2^i(k), \cdots, \sum_{k=1}^{K_1} \sum_{i=1}^{N} B_M^i(k) \right\} \tag{5.6}$$

and

$$QI_{spat} = \left\{ \sum_{k=1}^{K_2} \sum_{i=1}^{N} B_1^i(k), \sum_{k=1}^{K_2} \sum_{i=1}^{N} B_2^i(k), \cdots, \sum_{k=1}^{K_2} \sum_{i=1}^{N} B_M^i(k) \right\} \tag{5.7}$$

The maximum value of each column is reached when a method is satisfactory for all the metrics. This maximum value is $NxK_1$ and $NxK_2$ for the spectral and spatial cases, respectively. Thus, the various methods can be evaluated using, independently, the two columns after they are normalized. Nevertheless, the combination of the spectral and spatial results needs a normalization step, where each value of the spectral (or spatial) column is normalized by dividing it by the corresponding maximum value. Hence, to simplify the assessment, a global measure of quality index ($QI_{glob}$), resulting from the combination of the spectral ($QI_{spec}$) and the spatial ($QI_{spat}$) columns, can be expressed by a linear relation as:

$$QI_{glob} = a \frac{QI_{spec}}{NK_1} + b \frac{QI_{spat}}{NK_2} \tag{5.8}$$

where a and b are values to be adjusted experimentally, so that a+b=1 and $0<QI_{glob}<1$. Clearly, the higher the $QI_{glob}$, the better is the quality, and the lower the $QI_{glob}$, the worse is the quality.

## 5.3 Experimental Results

Experiments were conducted to evaluate the performance of the proposed protocol using Quickbird images downloaded from the landcover.org site. Ten images, shown in Figure 5.3, containing forests, buildings, and roads, are used for the evaluation purpose. The protocol is based on the spectral indexes: CC, VAR, SD, Q4, ERGAS and SAM, and on the spatial indexes: sCC, Zhou spatial CC (ZCC) [187] and true edge (TE) [164].

For the evaluation, we apply some of the popular pansharpening methods which are the Fast Intensity Hue Saturation (FIHS), the Generalized IHS (GIHS), the Spectral Adjust IHS (SAIHS) [171], wavelet [129], PCA and the NonSubsampled Contourlet Transform (NSCT) [77]. These techniques are implemented to test the proposed protocol. Hence, in reference to the protocol N=10, M=6, $K_1$=6, and $K_2$=3. The spectral and spatial tables are shown in Table 5.2 for the ten images.

Figure 5.3 Set of the ten images used for testing the proposed protocol.

| | Method | spectral | | | | | | spatial | | |
|---|---|---|---|---|---|---|---|---|---|---|
| | | CC | Var | SD | $Q_4$ | ERGAS | SAM | sCC | ZCC | TE |
| image 1 | FIHS | 0,696 | 0,633 | 0,108 | 0,625 | 2,821 | 3,397 | 0,801 | 0,973 | 0,829 |
| | GIHS | 0,832 | 0,659 | 0,077 | 0,725 | 2,153 | 3,234 | 0,785 | 0,981 | 0,708 |
| | SAIHS | 0,821 | 0,568 | 0,082 | 0,693 | 2,203 | 3,284 | 0,762 | 0,986 | 0,680 |
| | PCA | 0,948 | 0,477 | 0,051 | 0,877 | 1,706 | 2,511 | 0,855 | 0,863 | 0,455 |
| | Wavelet | 0,903 | 0,344 | 0,072 | 0,811 | 2,014 | 3,112 | 0,819 | 0,951 | 0,692 |
| | NSCT | 0,909 | 0,352 | 0,070 | 0,821 | 1,955 | 3,033 | 0,821 | 0,951 | 0,765 |

| | Method | spectral | | | | | | spatial | | |
|---|---|---|---|---|---|---|---|---|---|---|
| | | CC | Var | SD | $Q_4$ | ERGAS | SAM | sCC | ZCC | TE |
| image 2 | FIHS | 0,702 | 0,881 | 0,101 | 0,689 | 2,964 | 3,387 | 0,843 | 0,970 | 0,803 |
| | GIHS | 0,846 | 0,810 | 0,076 | 0,775 | 2,502 | 3,309 | 0,843 | 0,975 | 0,708 |
| | SAIHS | 0,833 | 0,731 | 0,078 | 0,755 | 2,484 | 3,324 | 0,834 | 0,982 | 0,674 |
| | PCA | 0,903 | 0,582 | 0,065 | 0,840 | 2,367 | 2,990 | 0,846 | 0,866 | 0,452 |
| | Wavelet | 0,887 | 0,505 | 0,068 | 0,829 | 2,247 | 3,189 | 0,860 | 0,953 | 0,719 |
| | NSCT | 0,889 | 0,530 | 0,068 | 0,833 | 2,224 | 3,129 | 0,861 | 0,953 | 0,782 |

| | Method | spectral | | | | | | spatial | | |
|---|---|---|---|---|---|---|---|---|---|---|
| | | CC | Var | SD | $Q_4$ | ERGAS | SAM | sCC | ZCC | TE |
| image 3 | FIHS | 0,746 | 0,810 | 0,078 | 0,731 | 2,653 | 3,125 | 0,878 | 0,952 | 0,785 |
| | GIHS | 0,834 | 0,773 | 0,067 | 0,772 | 2,447 | 3,102 | 0,878 | 0,967 | 0,694 |
| | SAIHS | 0,815 | 0,634 | 0,069 | 0,763 | 2,411 | 3,099 | 0,873 | 0,978 | 0,679 |
| | PCA | 0,881 | 0,741 | 0,062 | 0,809 | 2,277 | 2,609 | 0,868 | 0,868 | 0,538 |
| | Wavelet | 0,883 | 0,636 | 0,058 | 0,843 | 2,033 | 2,662 | 0,896 | 0,927 | 0,726 |
| | NSCT | 0,888 | 0,673 | 0,057 | 0,845 | 2,021 | 2,624 | 0,897 | 0,927 | 0,780 |

| | Method | spectral | | | | | | spatial | | |
|---|---|---|---|---|---|---|---|---|---|---|
| | | CC | Var | SD | $Q_4$ | ERGAS | SAM | sCC | ZCC | TE |
| image 4 | FIHS | 0,610 | 0,765 | 0,081 | 0,649 | 2,786 | 3,398 | 0,850 | 0,936 | 0,768 |
| | GIHS | 0,770 | 0,769 | 0,065 | 0,720 | 2,485 | 3,356 | 0,843 | 0,962 | 0,653 |
| | SAIHS | 0,749 | 0,568 | 0,069 | 0,703 | 2,468 | 3,366 | 0,828 | 0,976 | 0,630 |
| | PCA | 0,807 | 0,792 | 0,064 | 0,779 | 2,525 | 3,246 | 0,781 | 0,737 | 0,334 |
| | Wavelet | 0,817 | 0,797 | 0,061 | 0,796 | 2,157 | 3,014 | 0,865 | 0,910 | 0,683 |
| | NSCT | 0,825 | 0,812 | 0,060 | 0,799 | 2,129 | 2,946 | 0,866 | 0,910 | 0,747 |

| | Method | spectral | | | | | | spatial | | |
|---|---|---|---|---|---|---|---|---|---|---|
| | | CC | Var | SD | $Q_4$ | ERGAS | SAM | sCC | ZCC | TE |
| image 5 | FIHS | 0,341 | 0,799 | 0,094 | 0,480 | 2,917 | 2,282 | 0,889 | 0,924 | 0,774 |
| | GIHS | 0,833 | 0,521 | 0,045 | 0,641 | 1,823 | 1,728 | 0,885 | 0,945 | 0,689 |
| | SAIHS | 0,833 | 1,093 | 0,047 | 0,631 | 1,743 | 1,726 | 0,863 | 0,970 | 0,708 |
| | PCA | 0,752 | 0,756 | 0,059 | 0,626 | 3,231 | 4,274 | 0,712 | 0,393 | 0,149 |
| | Wavelet | 0,888 | 0,302 | 0,041 | 0,679 | 1,998 | 2,124 | 0,901 | 0,907 | 0,718 |
| | NSCT | 0,896 | 0,334 | 0,040 | 0,721 | 1,961 | 2,046 | 0,904 | 0,904 | 0,768 |

Table 5.2 spectral and spatial comparison of pansharpening methods.

| | Method | spectral | | | | | | spatial | | |
|---|---|---|---|---|---|---|---|---|---|---|
| | | CC | Var | SD | $Q_4$ | ERGAS | SAM | sCC | ZCC | TE |
| image 6 | FIHS | 0,636 | 0,853 | 0,129 | 0,587 | 3,460 | 4,232 | 0,800 | 0,974 | 0,828 |
| | GIHS | 0,823 | 0,813 | 0,089 | 0,705 | 2,641 | 4,013 | 0,790 | 0,980 | 0,697 |
| | SAIHS | 0,814 | 0,748 | 0,092 | 0,666 | 2,650 | 4,060 | 0,773 | 0,985 | 0,660 |
| | PCA | 0,930 | 0,200 | 0,063 | 0,825 | 2,305 | 3,360 | 0,837 | 0,813 | 0,338 |
| | Wavelet | 0,884 | 0,211 | 0,081 | 0,746 | 2,338 | 3,620 | 0,817 | 0,961 | 0,691 |
| | NSCT | 0,888 | 0,226 | 0,079 | 0,755 | 2,301 | 3,548 | 0,818 | 0,961 | 0,764 |
| image 7 | FIHS | 0,516 | 0,937 | 0,097 | 0,613 | 3,067 | 4,502 | 0,822 | 0,942 | 0,785 |
| | GIHS | 0,725 | 0,867 | 0,077 | 0,670 | 2,679 | 4,450 | 0,807 | 0,967 | 0,618 |
| | SAIHS | 0,705 | 0,735 | 0,084 | 0,640 | 2,710 | 4,514 | 0,784 | 0,978 | 0,594 |
| | PCA | 0,771 | 0,706 | 0,074 | 0,739 | 2,646 | 3,925 | 0,713 | 0,599 | 0,217 |
| | Wavelet | 0,770 | 0,760 | 0,074 | 0,755 | 2,321 | 3,724 | 0,839 | 0,912 | 0,643 |
| | NSCT | 0,777 | 0,793 | 0,073 | 0,759 | 2,293 | 3,682 | 0,839 | 0,913 | 0,716 |
| image 8 | FIHS | 0,349 | 0,892 | 0,106 | 0,505 | 3,024 | 3,866 | 0,849 | 0,937 | 0,812 |
| | GIHS | 0,762 | 0,673 | 0,063 | 0,598 | 2,217 | 3,589 | 0,837 | 0,961 | 0,602 |
| | SAIHS | 0,754 | 0,503 | 0,071 | 0,550 | 2,258 | 3,659 | 0,802 | 0,976 | 0,596 |
| | PCA | 0,790 | 0,775 | 0,065 | 0,738 | 2,494 | 3,826 | 0,709 | 0,459 | 0,146 |
| | Wavelet | 0,838 | 0,572 | 0,059 | 0,744 | 1,818 | 2,720 | 0,868 | 0,905 | 0,664 |
| | NSCT | 0,848 | 0,579 | 0,057 | 0,770 | 1,766 | 2,617 | 0,870 | 0,904 | 0,755 |
| image 9 | FIHS | 0,659 | 0,812 | 0,081 | 0,608 | 2,143 | 2,559 | 0,851 | 0,955 | 0,767 |
| | GIHS | 0,819 | 0,527 | 0,057 | 0,694 | 1,608 | 2,427 | 0,814 | 0,980 | 0,675 |
| | SAIHS | 0,801 | 0,537 | 0,063 | 0,652 | 1,675 | 2,469 | 0,783 | 0,983 | 0,657 |
| | PCA | 0,941 | 0,278 | 0,039 | 0,863 | 1,361 | 2,014 | 0,878 | 0,857 | 0,391 |
| | Wavelet | 0,901 | 0,437 | 0,051 | 0,794 | 1,488 | 2,170 | 0,859 | 0,932 | 0,654 |
| | NSCT | 0,903 | 0,452 | 0,050 | 0,800 | 1,467 | 2,130 | 0,860 | 0,932 | 0,725 |
| image 10 | FIHS | 0,613 | 0,919 | 0,101 | 0,655 | 3,032 | 3,597 | 0,850 | 0,960 | 0,815 |
| | GIHS | 0,818 | 0,877 | 0,071 | 0,757 | 2,482 | 3,494 | 0,848 | 0,972 | 0,704 |
| | SAIHS | 0,805 | 0,805 | 0,074 | 0,731 | 2,461 | 3,518 | 0,833 | 0,982 | 0,674 |
| | PCA | 0,871 | 0,512 | 0,066 | 0,833 | 2,583 | 3,476 | 0,781 | 0,749 | 0,358 |
| | Wavelet | 0,866 | 0,541 | 0,066 | 0,832 | 2,137 | 3,156 | 0,869 | 0,940 | 0,721 |
| | NSCT | 0,873 | 0,606 | 0,064 | 0,841 | 2,085 | 3,050 | 0,870 | 0,940 | 0,787 |

Table 5.2 (continued): spectral and spatial comparison of pansharpening methods.

In Table 5.3, the different thresholds corresponding to the ten images are shown. The parameter α is chosen to be 0.5. It is noted that for CC, $Q_4$, sCC_O, sCC_Z and TE we use $\theta_{ik} = \mu_{ik} + \alpha\sigma_{ik}$ and for Var, SD, ERGAS and SAM, the formula $\theta_{ik} = \mu_{ik} - \alpha\sigma_{ik}$ is used.

| | spectral | | | | | | spatial | | |
|---|---|---|---|---|---|---|---|---|---|
| Threshold | CC | Var | SD | $Q_4$ | ERGAS | SAM | sCC_O | sCC_Z | TE |
| $\theta_1$ | 0,896 | 0,437 | 0,067 | 0,805 | 1,954 | 2,939 | 0,823 | 0,973 | 0,752 |
| $\theta_2$ | 0,843 | 0,595 | 0,069 | 0,787 | 2,465 | 3,221 | 0,848 | 0,950 | 0,690 |
| $\theta_3$ | 0,841 | 0,674 | 0,061 | 0,794 | 2,307 | 2,870 | 0,882 | 0,936 | 0,700 |
| $\theta_4$ | 0,763 | 0,705 | 0,063 | 0,741 | 2,425 | 3,221 | 0,839 | 0,905 | 0,636 |
| $\theta_5$ | 0,757 | 0,482 | 0,044 | 0,630 | 2,279 | 2,363 | 0,859 | 0,840 | 0,634 |
| $\theta_6$ | 0,763 | 0,705 | 0,063 | 0,741 | 2,425 | 3,221 | 0,839 | 0,905 | 0,636 |
| $\theta_7$ | 0,711 | 0,843 | 0,085 | 0,696 | 2,619 | 4,133 | 0,801 | 0,885 | 0,595 |
| $\theta_8$ | 0,723 | 0,738 | 0,079 | 0,651 | 2,263 | 3,379 | 0,822 | 0,857 | 0,596 |
| $\theta_9$ | 0,837 | 0,595 | 0,064 | 0,735 | 1,624 | 2,295 | 0,841 | 0,940 | 0,645 |
| $\theta_{10}$ | 0,808 | 0,799 | 0,081 | 0,775 | 2,463 | 3,382 | 0,842 | 0,924 | 0,676 |

Table 5.3 calculated thresholds corresponding to each image and each metric.

Tables 5.2 and 5.3 allow deciding if a method is satisfactory or not. Ten tables, given in Table 5.4, will be generated corresponding to the ten images. In these tables, a method is considered satisfactory in terms of a metric if its value is greater than the corresponding threshold and "1" is assigned to this method, otherwise "0" will be assigned to it.

| | Method | spectral | | | | | | spatial | | |
|---|---|---|---|---|---|---|---|---|---|---|
| | | CC | Var | SD | $Q_4$ | ERGAS | SAM | sCC_O | sCC_Z | TE |
| Image 1 | FIHS | 0 | 0 | 0 | 0 | 0 | 0 | 0 | 0 | 1 |
| | GIHS | 0 | 0 | 0 | 0 | 0 | 0 | 0 | 1 | 0 |
| | SAIHS | 0 | 0 | 0 | 0 | 0 | 0 | 0 | 1 | 0 |
| | PCA | 1 | 0 | 1 | 1 | 1 | 1 | 1 | 0 | 0 |
| | Wavelet | 1 | 1 | 0 | 1 | 0 | 0 | 0 | 0 | 0 |
| | NSCT | 1 | 1 | 0 | 1 | 0 | 0 | 0 | 0 | 1 |
| Image 2 | FIHS | 0 | 0 | 0 | 0 | 0 | 0 | 0 | 1 | 1 |
| | GIHS | 1 | 0 | 0 | 0 | 0 | 0 | 0 | 1 | 1 |
| | SAIHS | 0 | 0 | 0 | 0 | 0 | 0 | 0 | 1 | 0 |
| | PCA | 1 | 1 | 1 | 1 | 1 | 1 | 0 | 0 | 0 |
| | Wavelet | 1 | 1 | 1 | 1 | 1 | 1 | 1 | 1 | 1 |
| | NSCT | 1 | 1 | 1 | 1 | 1 | 1 | 1 | 1 | 1 |
| Image 3 | FIHS | 0 | 0 | 0 | 0 | 0 | 0 | 0 | 1 | 1 |
| | GIHS | 0 | 0 | 0 | 0 | 0 | 0 | 0 | 1 | 0 |
| | SAIHS | 0 | 1 | 0 | 0 | 0 | 0 | 0 | 1 | 0 |
| | PCA | 1 | 0 | 0 | 1 | 1 | 1 | 0 | 0 | 0 |
| | Wavelet | 1 | 1 | 1 | 1 | 1 | 1 | 1 | 0 | 1 |
| | NSCT | 1 | 1 | 1 | 1 | 1 | 1 | 1 | 0 | 1 |
| Image 4 | FIHS | 0 | 0 | 0 | 0 | 0 | 0 | 1 | 1 | 1 |
| | GIHS | 1 | 0 | 0 | 0 | 0 | 0 | 1 | 1 | 1 |
| | SAIHS | 0 | 1 | 0 | 0 | 0 | 0 | 0 | 1 | 0 |
| | PCA | 1 | 0 | 0 | 1 | 0 | 0 | 0 | 0 | 0 |
| | Wavelet | 1 | 0 | 1 | 1 | 1 | 1 | 1 | 1 | 1 |
| | NSCT | 1 | 0 | 1 | 1 | 1 | 1 | 1 | 1 | 1 |

Table 5.4 methods thresholding.

| | Method | spectral | | | | | | spatial | | |
|---|---|---|---|---|---|---|---|---|---|---|
| | | CC | Var | SD | $Q_4$ | ERGAS | SAM | sCC_O | sCC_Z | TE |
| Image 5 | FIHS | 0 | 0 | 0 | 0 | 0 | 1 | 1 | 1 | 1 |
| | GIHS | 1 | 0 | 0 | 1 | 1 | 1 | 1 | 1 | 1 |
| | SAIHS | 1 | 0 | 0 | 1 | 1 | 1 | 1 | 1 | 1 |
| | PCA | 0 | 0 | 0 | 0 | 0 | 0 | 0 | 0 | 0 |
| | Wavelet | 1 | 1 | 1 | 1 | 1 | 1 | 1 | 1 | 1 |
| | NSCT | 1 | 1 | 1 | 1 | 1 | 1 | 1 | 1 | 1 |
| Image 6 | FIHS | 0 | 0 | 0 | 0 | 0 | 0 | 0 | 1 | 1 |
| | GIHS | 0 | 0 | 1 | 0 | 0 | 0 | 0 | 1 | 1 |
| | SAIHS | 0 | 0 | 1 | 0 | 0 | 0 | 0 | 1 | 0 |
| | PCA | 1 | 1 | 1 | 1 | 1 | 1 | 1 | 0 | 0 |
| | Wavelet | 1 | 1 | 1 | 1 | 1 | 1 | 1 | 1 | 1 |
| | NSCT | 1 | 1 | 1 | 1 | 1 | 1 | 1 | 1 | 1 |
| Image 7 | FIHS | 0 | 0 | 0 | 0 | 0 | 0 | 1 | 1 | 1 |
| | GIHS | 1 | 0 | 1 | 0 | 0 | 0 | 1 | 1 | 1 |
| | SAIHS | 0 | 1 | 1 | 0 | 0 | 0 | 0 | 1 | 0 |
| | PCA | 1 | 1 | 1 | 1 | 0 | 1 | 0 | 0 | 0 |
| | Wavelet | 1 | 1 | 1 | 1 | 1 | 1 | 1 | 1 | 1 |
| | NSCT | 1 | 1 | 1 | 1 | 1 | 1 | 1 | 1 | 1 |
| Image 8 | FIHS | 0 | 0 | 0 | 0 | 0 | 0 | 1 | 1 | 1 |
| | GIHS | 1 | 1 | 1 | 0 | 1 | 0 | 1 | 1 | 1 |
| | SAIHS | 1 | 1 | 1 | 0 | 1 | 0 | 0 | 1 | 1 |
| | PCA | 1 | 0 | 1 | 1 | 0 | 0 | 0 | 0 | 0 |
| | Wavelet | 1 | 1 | 1 | 1 | 1 | 1 | 1 | 1 | 1 |
| | NSCT | 1 | 1 | 1 | 1 | 1 | 1 | 1 | 1 | 1 |
| Image 9 | FIHS | 0 | 0 | 0 | 0 | 0 | 0 | 1 | 1 | 1 |
| | GIHS | 0 | 1 | 1 | 0 | 1 | 0 | 0 | 1 | 1 |
| | SAIHS | 0 | 1 | 1 | 0 | 0 | 0 | 0 | 1 | 1 |
| | PCA | 1 | 1 | 1 | 1 | 1 | 1 | 1 | 0 | 0 |
| | Wavelet | 1 | 1 | 1 | 1 | 1 | 1 | 1 | 0 | 1 |
| | NSCT | 1 | 1 | 1 | 1 | 1 | 1 | 1 | 0 | 1 |
| Image 10 | FIHS | 0 | 0 | 0 | 0 | 0 | 0 | 1 | 1 | 1 |
| | GIHS | 1 | 0 | 1 | 0 | 0 | 0 | 1 | 1 | 1 |
| | SAIHS | 0 | 0 | 1 | 0 | 1 | 0 | 0 | 1 | 0 |
| | PCA | 1 | 1 | 1 | 1 | 0 | 0 | 0 | 0 | 0 |
| | Wavelet | 1 | 1 | 1 | 1 | 1 | 1 | 1 | 1 | 1 |
| | NSCT | 1 | 1 | 1 | 1 | 1 | 1 | 1 | 1 | 1 |

Table 5.4 (continued): methods thresholding.

The summation of the ten spectral and ten spatial tables is shown in Table 5.5.

| | | spectral | | | | | | spatial | | |
|---|---|---|---|---|---|---|---|---|---|---|
| | | CC | Var | SD | Q4 | ERGAS | SAM | sCC_O | sCC_Z | TE |
| All images | FIHS | 0 | 0 | 0 | 0 | 0 | 1 | 6 | 9 | 10 |
| | GIHS | 6 | 2 | 5 | 1 | 3 | 1 | 5 | 10 | 8 |
| | SAIHS | 2 | 5 | 5 | 1 | 3 | 1 | 1 | 10 | 3 |
| | PCA | 9 | 5 | 7 | 9 | 5 | 6 | 3 | 0 | 0 |
| | Wavelet | 10 | 9 | 9 | 10 | 9 | 9 | 9 | 7 | 9 |
| | NSCT | 10 | 9 | 9 | 10 | 9 | 9 | 9 | 7 | 10 |

Table 5.5 Summation of decisions.

A summation is now conducted separately for the spectral and spatial indexes to compute $QI_{spec}$ and $QI_{spat}$, resulting in Table 5.6. In addition, the normalization of these indexes can give measures for spectral and spatial qualities separately.

| | | | Normalisation | |
|---|---|---|---|---|
| | $QI_{spec}$ | $QI_{spat}$ | $QI_{spec}$ | $QI_{spat}$ |
| FIHS | 1 | 25 | 0,017 | 0,833 |
| GIHS | 18 | 23 | 0,300 | 0,767 |
| SAIHS | 17 | 14 | 0,283 | 0,467 |
| PCA | 41 | 3 | 0,683 | 0,100 |
| Wavelet | 56 | 25 | 0,933 | 0,833 |
| NSCT | 56 | 26 | 0,933 | 0,867 |

Table 5.6 computation of $QI_{spec}$ and $QI_{spat}$.

At this stage, the global measure of the quality index ($QI_{glob}$), resulting from the combination of the spectral ($QI_{spec}$) and the spatial ($QI_{spat}$) columns, can be done. For the studied case, the formula used is as:

$$QI_{glob} = 0.5\frac{QI_{spec}}{10\times 6} + 0.5\frac{QI_{spat}}{10\times 3}$$

The parameters a and b are each fixed to 0.5 allowing an equal contribution of the spectral and the spatial quality. The obtained results as well as the ranking of the evaluated methods are given in Table 5.7.

| | $QI_{glob}$ | Rank |
|---|---|---|
| FIHS | 0,425 | 4 |
| GIHS | 0,533 | 3 |
| SAIHS | 0,375 | 6 |
| PCA | 0,392 | 5 |
| Wavelet | 0,883 | 2 |
| NSCT | 0,900 | 1 |

Table 5.7 computation of $QI_{glob}$ and rank.

From Table 5.2 and for the first image, it is clear that considering only spectral indexes, will lead to conclude that the PCA based method is the best. However, the authors in [77] have demonstrated that NSCT is more efficient than PCA. The use of spatial indexes seems to be mandatory, however,

when looking at Table 5.2, it appears that, in term of sCC, PCA is good; in term of ZCC, SAIHS is good; and finally, in term of TE, FIHS is the best. In most of the literature, there is a consensus that the IHS-based fusion method is the best in preserving spatial information [189]. This is consistent with the TE and ZCC metrics. However and up to now, as can be seen in Table 5.2, no ranking of different methods can be envisaged yet when considering all metrics.

The visual analysis of an obtained result, corresponding to the first image and shown in Figure 5.4, states that the wavelet and NSCT are the best methods.

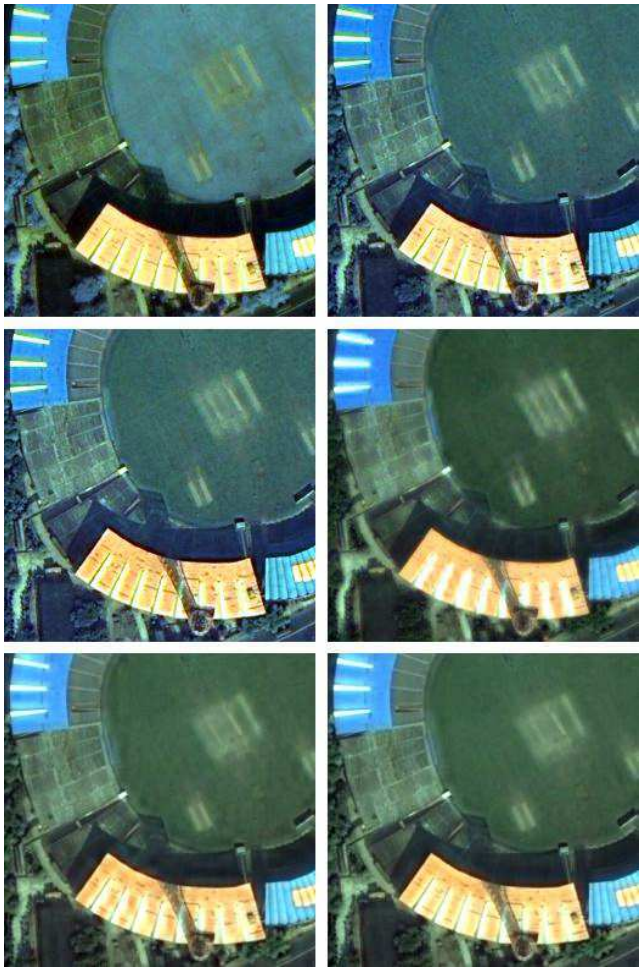

Figure 5.4 Pansharpened images: top left: FIHS, top right: GIHS, middle left: SAIHS, middle right: PCA, bottom left: wavelet, bottom right: NSCT.

In this case, where visual results do not correspond to metrics, it is necessary to have a protocol making the classification of methods more reliable and a lot easier. Applying the proposed protocol produces spectral $QI_{spec}$ and spatial $QI_{spat}$ measures in table 5.6, and the global measure $QI_{glob}$ is then computed assuming that the spatial indexes are as important as the spectral ones. Then, it is obvious that the NSCT based fusion method is the best. In accordance with visual analysis, wavelet is ranked in the second position, better than PCA which is in the fourth place. Thus, this proposed classification is reliable, in accordance with the visual evaluation, automatic and easy-to-use.

According to the obtained results, the spatial correlation coefficient (ZCC) is more reliable in assessing spatial quality compared to the sCC metric. This remark agrees with the comment of [73] and [163], where the authors recommend the use of ZCC instead of sCC.

Moreover, it is to note that there is a necessity of developing a more reliable and efficient metric for assessing the spatial quality.

## 5.4 Conclusion

The comparison of various pansharpening methods is not an easy task if the aspect of spatial characteristics is not considered. Moreover, the use of multiple indexes in the evaluation process enforces the final results. The proposed protocol can make the comparison of quality metrics a lot easier. Hence, more indexes can be integrated into this protocol to assess different methods making comparison a lot more accurate. The experiments conducted in this study show that using the proposed protocol can facilitate the visual evaluation of the results, by making assessing methods automatic and more reliable.

# Conclusion

Pansharpening is currently considered as being a very important research area in the remote sensing domain. The wide use of the pansharpened images for several applications, has led to a phenomenal development of the related algorithms. Moreover, the availability of newer satellites and images require new techniques for pansharpening or adoption of the existing ones. All necessary steps including pre-processing and interpolation must be re-considered. On the other hand, the quality assessment of the obtained results still needs more and more effort for developing efficient tools for a correct and accurate evaluation.

The objectives of this research work try to cover these considerations about pansharpening techniques and quality assessment of pansharpened images. The conducted works are focused on the high resolution images, as those obtained from Ikonos, QuickBird and Worldview satellites and they focus on vegetation extraction.

In this thesis, after a general introduction to remote sensing, a detailed categorisation of the existing pansharpening methods is presented. Moreover, some of the pre-processing algorithms, as interpolation, are also given. Then, several indexes used to measure the quality of the pansharpened images are presented. These tools are necessary for the validation of the proposed algorithms.

The impact of the interpolation in the pansharpened resulting images is considered. It is found that the pansharpened images will be improved if the used interpolation method can preserve the edges. The ICBI interpolation approach was studied and the obtained results clearly show that the ICBI-based fused images give very good results, both visually and quantitatively. Moreover, the edges of the Pan image are totally preserved in the ICBI-based fused images and this is an interesting aspect since it may be important, especially when the user does not have the Pan image. It is to note that

ICBI is not the only interpolation method which can improve the pansharpened images. In the future, experiments may be conducted, using other interpolation methods, to study their efficiency and impact on pansharpened images.

When we have presented our main contributions in pansharpening techniques: three algorithms were proposed. The first two ones are both based on the IHS transform. Pansharpening is done in two steps: fusion and vegetation enhancement. In the first algorithm, vegetation is detected by the NDVI index and the enhancement is done before the fusion process. In contrast, for the second algorithm, the enhancement is done after the fusion process. When developing this second algorithm, a new vegetation index was proposed, defined and used to delineate vegetation. We call this index high resolution NDVI (HRNDVI). It can be used for high resolution satellites, where MS and Pan images are available. The new proposed pansharpening algorithms were tested on high spatial resolution images issued from Ikonos or QuickBird. These algorithms were compared to existing methods to show their effectiveness. Evaluation was driven quantitatively and qualitatively.

Moreover, HRNDVI was used to extract vegetation from high resolution satellite images. The provided results are excellent, this index allows extraction of vegetation even in the urban case where the vegetation is scattered. Hence, the extracted images are more accurate especially in the urban area. It can provide a high resolution vegetation mapping. The resulting proposed vegetation extraction method, based on HRNDVI, yields accurate vegetation extraction and high resolution characteristics of the corresponding mapping.

The third pansharpening algorithm is based on the nonsubsampled contourlet transform multiresolution frames. The NSCT transform was used in a classical form as well as in its hybrid form, using PCA. The improvement of the NSCT-based image pansharpening is assured by using a low number of decomposition levels for MS images and a high number of decomposition levels for the Pan image. This strategy gives satisfying visual and quantitative results. The spectral quality of MS images is better preserved when a lower number of decomposition levels is used, in contrast, this number must be higher to preserve the spatial quality of the Pan image. The performance of the proposed strategy is tested on QuickBird and WorldView-2 data and the obtained results confirm the added-value of using an adequate number of decomposition levels. This algorithm based on NSCT, was submitted to the 2012 IEEE GRSS Data Fusion Contest: Multimodal/multi-temporal fusion. It was selected by the committee to be among the 10 best submitted papers, where more than 1150 researchers from 78 different countries were registered for the contest.

All the pansharpening proposed algorithms were quantitatively evaluated. The main problem of the quality assessment is the non availability of the reference image. Some authors tried to define a new concept based on quality with no reference, concept which was not, until now, very used in the

pansharpening community. The most used concept is still based on the proprieties defined by Wald. Even if the reference image is available, the quality assessment is not an easy task. The existing metrics need to be completed with other metrics for estimating the spatial quality. In fact, the work conducted in the last Chapter shows that: the majority of the recommended and used metrics for pansharpening promotes the spectral quality more than the spatial one. Consequently, we propose a new protocol to correctly evaluate both spatial and spectral qualities. This protocol can integrate many metrics. The aspect of spatial and spectral qualities can be adjusted, according to the considered application. Moreover, a global measure of pansharpening quality is provided. This protocol allows comparing and ranking several methods. Experimental results demonstrate the efficiency of this protocol.

This protocol must not be substituted to any subjective evaluation, we must considerate it as a tool to help for the numerous comparative tests inherent to the evaluation of an algorithm.

This research work contributes to reach various different enhancements at different levels of the pansharpening process, but the pansharpening domain may still need more new algorithms and tools for its quality assessment.

Our experiments covered different steps and different approaches of pansharpening, and from our experiences in this domain we may try to extract and summarize some more precise recommendations for “the best pansharpening”. One first point is to take into consideration some pre-processing algorithms, as interpolation. Moreover, the research must focus on the use of multiresolution analysis for the core of the pansharpening algorithms. The processing will be heavier but the time complexity should be reduced, using parallel architectures or GPUs, or simply integrating new future processors.

# Appendix A: Interpolation impacts on pansharpened images

## A.1 Introduction

In high resolution imagery as Ikonos, QuickBird or WorldView-2, both MS and Pan images are provided with different spatial and spectral resolutions. In a pansharpening process, before fusing, the MS images are resampled to the same pixel size as the Pan image and this upsampling impacts subsequent processing. In this appendix, we demonstrate that the interpolation method, used to resample the MS images, is very important in preserving the edges in the pansharpened images. Most of the proposed methods make use of edge information which is provided by the pansharpened images or directly by Pan images if available. This information may be used for cartography, traffic management, map updating in Geographical Information Systems (GIS), environmental inspection, transportation and urban planning, etc [190], [191].

In this work, we analyze the impact of interpolation on the quality of the fused images. In pansharpening, the commonly used linear interpolation methods, such as bilinear and bicubic, have advantages in simplicity and fast implementation. However, they suffer from some inherent defects, including block effects, blurred details and ringing artifacts around edges.

In order to better preserve edges we use the fast artifacts-free image interpolation technique proposed in [170] and called ICBI (Iterative Curvature Based Interpolation). This interpolation method is based on the combination of two different procedures. First, an adaptive algorithm is applied interpolating locally pixel values along the direction where the image second order derivative is lower. Then the interpolated values are modified using an iterative refinement

minimizing differences in the image second order derivatives, maximizing second order derivative values and smoothing isolevel curves. The first algorithm itself provides edge-preserved images that are measurably better than those obtained with similarly fast methods presented in the literature. The full method provides interpolated images with a "natural" appearance that do not present the artifacts affecting linear and nonlinear methods. The results of ICBI method obtained on a wide series of natural images are attractive. Hence, we have decided to use this method in the fusion process to preserve edges in the pan-sharpened images. It is to note that other interpolation methods were tested on satellite images, but they are not as efficient as the ICBI method.

The ICBI method is compared to Bicubic method in pansharpening context, using conventional IHS fusion method. The quality of the obtained results is assessed visually and quantitatively. Moreover, we propose to compare edge information obtained from Canny's edge detector [192] applied to the Pan image and the fused results. This new index, which we call Edge Error, enables to measure edge preservation in two pansharpened images.

## A.2 Evaluation of interpolation effects

For the evaluation of the interpolation effects, we have selected the following list of indexes from those presented in chapter 3. For each spectral band, we compute: the bias in relative value, the difference in variance in relative value (VAR), the standard-deviation of the differences on a pixel basis in relative value (SD), the correlation coefficient (CC) and the correlation between high frequencies (sCC). For the whole image, we compute the average spectral angle mapper (SAM) and the relative dimensionless global error in synthesis (ERGAS).

In addition, we use the proposed "Edge Error" metric, where we compare the edge information obtained from applying Canny's edge detector [192] to the Pan image and the fused results corresponding to the bicubic and ICBI interpolations. For the edge map from each fused image, we compute the number of pixels not belonging to the edge map of the Pan image. Then we divide this number by the total number of the edge pixels in the Pan image to obtain what we call the edge error. It is clear that the edge error measures the missed and the added (fantom edges) edges compared to the reference Pan edge image. If the fused edge image preserves exactly the same Pan edge then the edge error equals zero.

## A.3 Experimental results

An image of Mt. Wellington, Tasmania, Australia, taken by the Ikonos satellite sensor on January 2005 is used for this experiment. The size of the original Pan image is approximately 12000×13000 pixels from which we extract portions for our experiments. Before image fusion, the MS images are resampled to the same pixel size as the Pan image using the two interpolation methods.

In Table A.1, we present the comparison results for two test images with size 1024x1024 for the fused images, corresponding to Figure A.1 and Figure A.2.

| | | Set 1 | | Set 2 | |
|---|---|---|---|---|---|
| | | Bicubic | ICBI | Bicubic | ICBI |
| BIAS | R | 0.0330 | 0.0133 | 0.2034 | 0.2287 |
| | G | 0.0007 | 0.0550 | 0.2458 | 0.2787 |
| | B | 0.0102 | 0.0409 | 0.2768 | 0.3081 |
| VAR | R | 0.3882 | 0.3272 | 0.1155 | 0.0471 |
| | G | 0.3591 | 0.2946 | 0.1975 | 0.1258 |
| | B | 0.4376 | 0.3561 | 0.0273 | 0.0216 |
| SD | R | 0.2609 | 0.2651 | 0.2810 | 0.2848 |
| | G | 0.2762 | 0.2804 | 0.2996 | 0.3044 |
| | B | 0.3167 | 0.3148 | 0.3465 | 0.3535 |
| CC | R | 0.7274 | 0.7375 | 0.7793 | 0.7841 |
| | G | 0.6994 | 0.7106 | 0.7631 | 0.7711 |
| | B | 0.6639 | 0.6834 | 0.6885 | 0.6923 |
| sCC | R | 0.9938 | 0.9962 | 0.9953 | 0.9963 |
| | G | 0.9938 | 0.9950 | 0.9966 | 0.9975 |
| | B | 0.9939 | 0.9957 | 0.9960 | 0.9963 |
| SAM | | 7.6420 | 6.2503 | 6.0748 | 5.5250 |
| ERGAS | | 10.8373 | 10.6809 | 12.5027 | 12.8319 |
| Edge error | | 0.0615 | 0.0000 | 0.0746 | 0.0000 |

Table A.1 A Comparison of Image Fusion using the Bicubic and ICBI interpolations for two Ikonos Test regions

In each figure, the original low spatial resolution RGB image and the high spatial resolution Pan image are shown in (a) and (b) respectively. While the fused images obtained using bicubic and ICBI interpolation methods are given in (d) and (e), respectively.

In this work, the idea used to visually compare the efficiency of the interpolation methods consist in:

- Using Canny operator to detect the edge maps of the Pan image and the fused images, obtained using the two interpolation methods.
- Generating an RGB edges image, using the resulting edge maps, where

  The black color represents the edges detected in the three images.

  The purple color is used for the edges detected in Pan and ICBI-based fused images.

  The green color represents the edges detected in Bicubic-based fused image only.

In both figures (A.1) and (A.2), the constructed image is illustrated in (e) and a zoomed part of it in (f).

Clearly for the Bicubic-based fused image, compared to the Pan image, the purple color corresponds to non detected edges, while the green color corresponds to added or fantom edges.

As can be seen on these figures (Figure A.1(f) and Figure A.2(f)), the ICBI-based results preserve the original Pan edge by producing a zero edge error. In addition this method provides better values in terms of most of the pansharpening evaluation indexes.

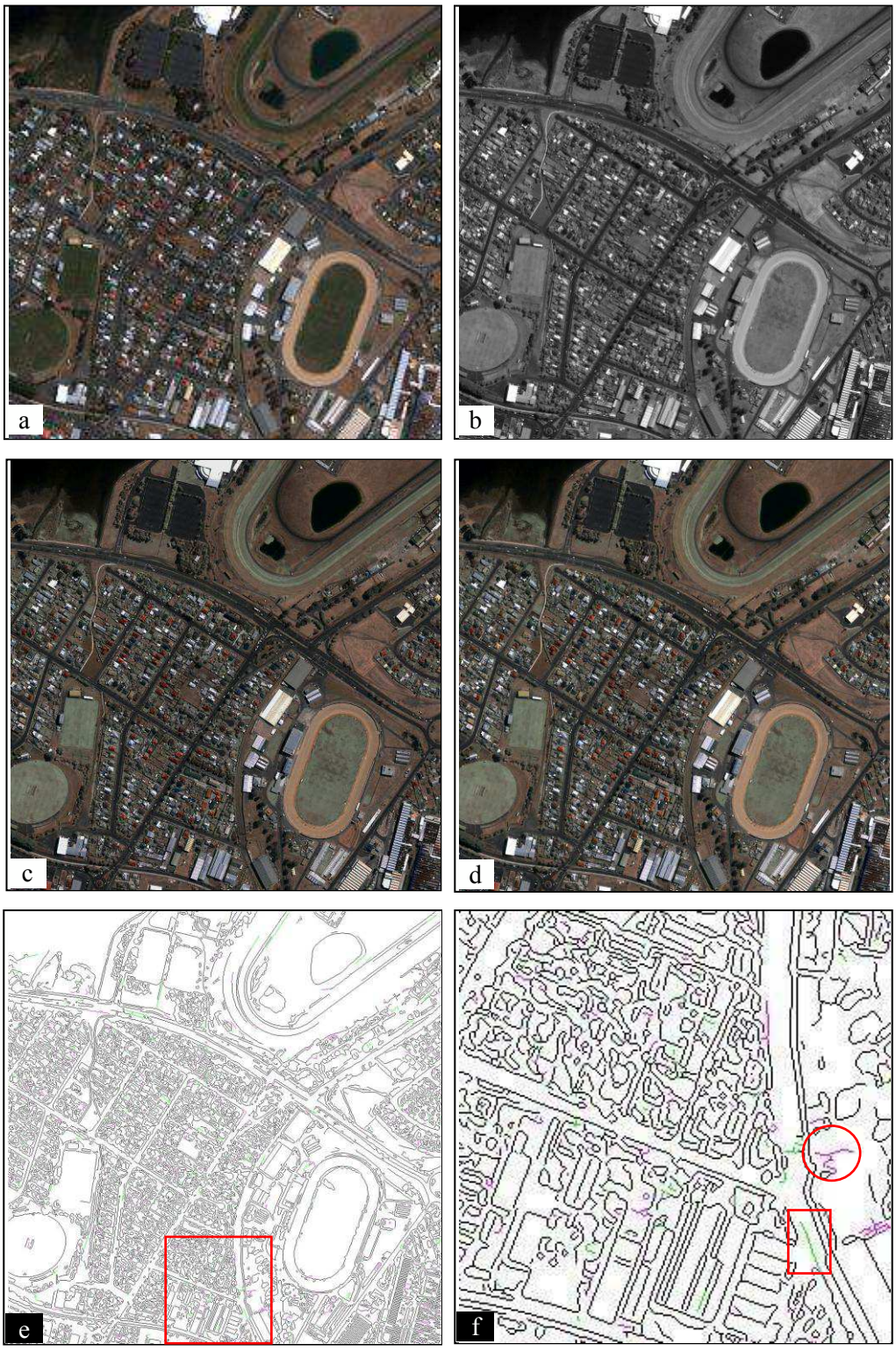


Figure A.1 Set 1, (a) low-resolution RGB image. (b) Corresponding Pan image. (c) Fused result using Bicubic interpolation. (d) Fused result using ICBI interpolation. (e) Edge information visualized as RGB image, where channels R, G and B correspond to edges extracted from images shown in (b), (c) and (d) respectively. (f) An area of (e).

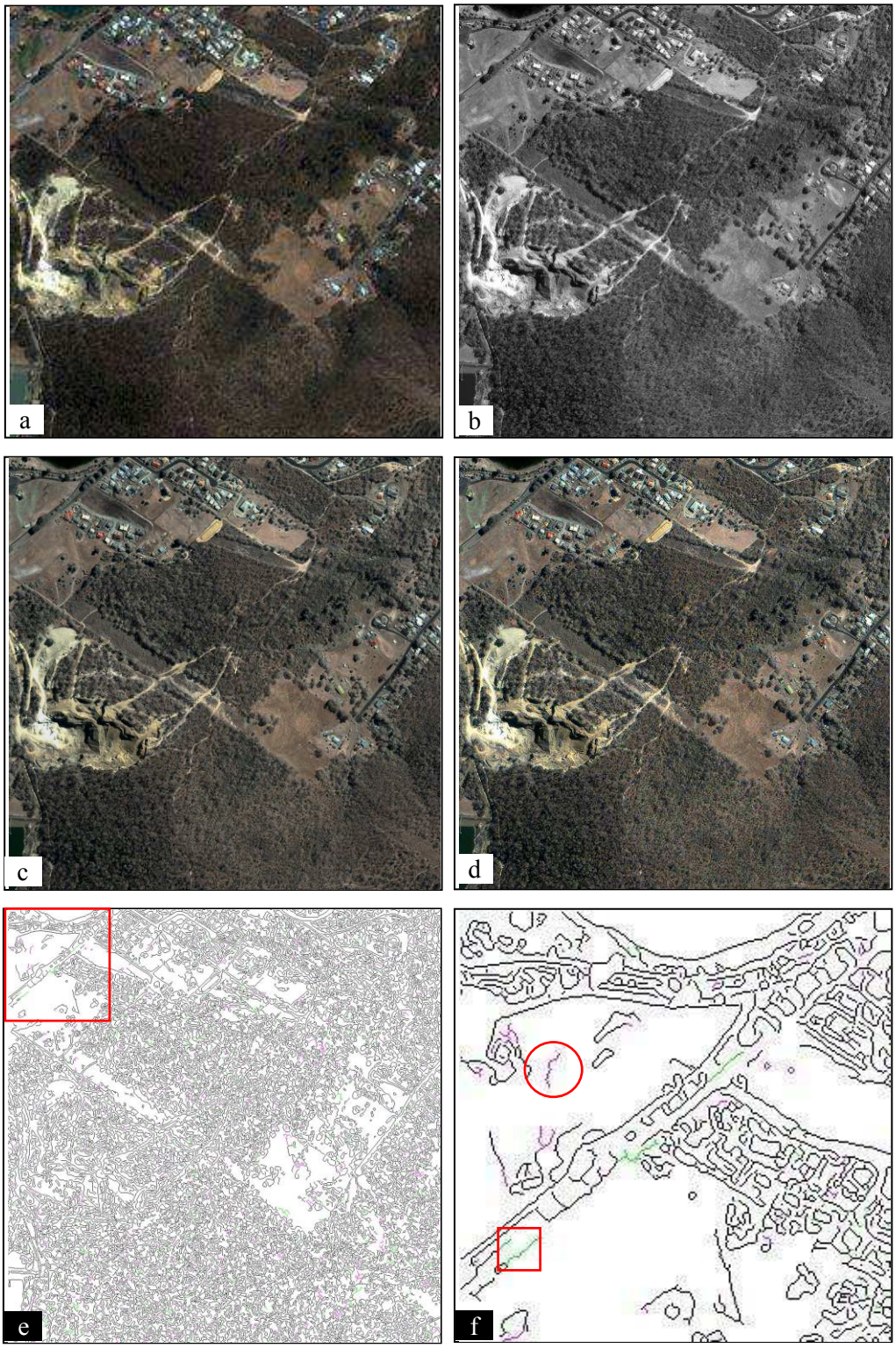


Figure A.2 Set 2, (a) low-resolution RGB image. (b) Corresponding Pan image. (c) Fused result using Bicubic interpolation. (d) Fused result using ICBI interpolation. (e) Edge information visualized as RGB image, where channels R, G and B correspond to edges extracted from images shown in (b), (c) and (d) respectively. (f) An area of (e).

The results presented in Figure A.1 and Figure A.2 show vegetation color degradation in the fused images; this is due to the use of the IHS fusion scheme on Ikonos images [171]. These degradations are harmful in applications of vegetation extraction [172], visualization or enhancement [171]. In this work, we are more interested to preserve edge information in the pansharpened images provided from the Pan images. Hence we compare the same method with two different interpolation techniques. The fused results using the bicubic and the ICBI interpolation methods are shown in (c) and (d), respectively, for the two images of Figure A.1 and Figure A.2. Figure A.1(e) and Figure A.2(e) illustrate the edges of the Pan image (in R), of the fused image using the bicubic interpolation (in G) and of the fused image using the ICBI interpolation in (B).

When a pixel belongs to Pan edges and to edges from both fused images, it is displayed in black color. The purple color (circles) shows edge pixels detected in the Pan and ICBI-based fused images. The green color (rectangles) illustrates edge pixels detected in the bicubic-based fused image only.

Figure A.1(f) and Figure A.2(f) are 256x256 pixels parts from the whole 1024x1024 pixel images in Figure A.1(e) and Figure A.2(e), respectively. We can see that the bicubic-based fused results miss some edges which may be important in many applications like road extraction. Moreover added edges (or fantom edges) are observed. These false edges can easily distort the results, especially when the edges are the only tool to make a decision.

## A.4 Conclusion

In this section, we have used the IHS fusion method to produce the pansharpened Ikonos images. We have considered two interpolation methods, the bicubic method as a standard technique and a more sophisticated one that is the ICBI approach. The obtained results clearly show that the ICBI-based fused images give very good results, both visually and quantitatively. Moreover, the edges are totally preserved in the ICBI-based fused images and this is an interesting aspect since it may be important, especially when the user does not have the Pan image.

In future works, one can integrate more interpolation methods in more advanced fusion techniques in order to choose the best interpolation method which deals with pansharpening.

# Bibliography


**[1]** Schowengerdt, R., Remote Sensing: Models and Methods for Image Processing, 3rd ed., Academic Press, Elsevier, NY, 2007.

**[2]** Wald, L. Some terms of reference in data fusion. IEEE Transaction on Geoscience and Remote Sensing, vol. 37, no. 3, pp. 1190–1193. (May 1999 ).

**[3]** I. Amro, J. Mateos, M. Vega, R. Molina and A. K Katsaggelos. "A survey of classical methods and new trends in pansharpening of multispectral images". EURASIP Journal on Advances in Signal Processing 2011 2011:79.

**[4]** "Spectral Responses for DigitalGlobe Earth Imaging Instruments", available at http://www.digitalglobe.com/resources/Technical Information, accessed 04/25/2012

**[5]** D. Brunner, G. Lemoine, and L. Bruzzone, "Earthquake damage assessment of buildings using VHR optical and SAR imagery," IEEE Transactions on Geoscience and Remote Sensing, vol. 48, no. 5, pp. 2403-2420, 2010.

**[6]** D. Brunner, G. Lemoine, and L. Bruzzone, "Change detection for earthquake damage assessment in built-up areas using very high resolution optical and SAR imagery", Geoscience and Remote Sensing Symposium (IGARSS), 2010 IEEE International, 25-30 July 2010 pp. 3210-3213

**[7]** Shirvany, R.; Chabert, M.; Tourneret, J.-Y. "Ship and Oil-Spill Detection Using the Degree of Polarization in Linear and Hybrid/Compact Dual-Pol SAR" IEEE Early Access Articles, IEEE Journal of Selected Topics in Applied Earth Observations and Remote Sensing, 2012, Pages (1-8).

**[8]** Vasuki, P. and Mohamed Mansoor Roomi, S. "Man-made object classification in SAR images using Gabor wavelet and neural network classifier", Devices, Circuits and Systems (ICDCS), 2012 International Conference on, 15-16 March 2012, pp. 537 - 539

**[9]** Thomasson A., Mondelain D., Ménard T., Nominé M., Godet Y., Wolf J., "Air pollution mapping using all solid-state LIDAR systems", C.R. Academy of Science 7(IV): 923-929, 2001

**[10]** As-syakur, A.R.; Osawa, T.; Adnyana, I.W.S. Medium Spatial Resolution Satellite Imagery to Estimate Gross Primary Production in an Urban Area. Remote Sens. 2010, 2, 1496-1507.

**[11]** Weng, Q., & Hu, X. (2008). Medium spatial resolution satellite imagery for estimating and mapping urban impervious surfaces using LSMA and ANN. IEEE Transactions on Geoscience and Remote Sensing, 46(8), 2397−2406.

**[12]** Peteri, R.; Ranchin, T. "Potentialités des nouveaux capteurs à très haute résolution spatiale pour l'extraction des réseaux de rues urbains". Revue internationale de Géomatique. 14, pp. 485-504, 2004.

**[13]** A. R. Vasques, L. L. Volpe and M. A. Lombardo, " Multitemporal analysis to identify brownfields redevelopment dynamic by high resolution satellite imagery in Sao Paulo – brazil", Proceedings of the 4th WSEAS International Conference on REMOTE SENSING (REMOTE'08) pp 130-135, venice italy November 21-23, 2008.

**[14]** C. Bacour, F. M. Breon, F. Maignan, "Normalization of the directional effects in NOAA - AVHRR reflectance measurements for an improved monitoring of vegetation cycles." Remote Sensing of Environment, 2006, 102, n°3-4, 402-413.

**[15]** R. L. Pearson and L. D. Miller. Remote mapping of standing crop biomass for estimation of the productivity of the shortgrass prairie, pawnee national grasslands, colorado. In Proceedings of the 8th International Symposium on Remote Sensing of the Environment II, pages 1355–1379, 1972.

**[16]** J. W. Rouse. Monitoring the vernal advancement and retrogradation of natural vegetation. Type ii report, NASA/GSFCT, Greenbelt, MD, USA, 1973.

**[17]** Bannari A., Asalhi H. and Teillet P.M., (2002), "Transformed difference vegetation index (TDVI) for vegetation cover mapping", International Geoscience and Remote Sensing Symposium, Toronto, Ontario, Canada, Proceedings on CD-Rom, paper I2A35-1508.

**[18]** A. J. Richardson and C. L. Wiegand. Distinguishing vegetation from soil background information. Photogrammetric Engineering and Remote Sensing, 43(12):1541–1552, 1977.

**[19]** A. R. Huete. A soil-adjusted vegetation index (SAVI). Remote Sensing of Environment, 25:295–309, 1988.

**[20]** J. Clevers. The derivation of a simplified reflectance model for the estimation of leaf area index. Remote Sensing of Environment, 25:53–69, 1988.

**[21]** J. Qi, A. . Chehbouni, A. Huete, Y. Kerr, and S. Sorooshian. A modified soil adjusted vegetation index. Remote Sensing of Environment, 47:1–25, 1994.

**[22]** R. E. Crippen. Calculating the vegetation index faster. Remote Sensing of Environment, 34(1):71–73, 1990.

**[23]** E. Baret, G. Guyot, and D. J. Major. TSAVI: A vegetation index which minimizes soil brightness effects on LAI and APAR estimation. In Proceedings of the 12th Canadian Symposium on Remote Sensing, Vancouver, Canada, pages 1355–1358, 1989.

**[24]** Y. J. Kaufman and D. Tanré. Atmospherically Resistant Vegetation Index (ARVI) for EOS-MODIS. Transactions on Geoscience and Remote Sensing, 40(2):261–270, Mar. 1992.

**[25]** A. R. Huete, C. Justice, and H. Liu. Development of vegetation and soil indices for MODIS-EOS. Remote Sensing of Environment, 49:224–234, 1994.

**[26]** B. Pinty and M. M. Verstraete. GEMI: a non-linear index to monitor global vegetation from satellites. Vegetatio, 101:15–20, 1992.

**[27]** http://www.spotimage.fr

**[28]** http://geo.arc.nasa.gov/sge/landsat/

**[29]** http://www.geoeye.com/CorpSite/products-andservices/imagery-sources/

**[30]** http://www.orbital.com/SatellitesSpace/ImagingDefense/

**[31]** http://www.digitalglobe.com

**[32]** M. Yazdi and A. Golibagh Mahyari (2011). Pansharpening Methods Based on ARSIS Concept, Image Fusion, Osamu Ukimura (Ed.), ISBN: 978-953-307-²679-9, InTech, Available from: http://www.intechopen.com/books/image-fusion/pansharpening-methods-based-on-arsis-concept

**[33]** Canada Centre for Remote Sensing, "Fundamentals of Remote Sensing", available at http://www.nrcan.gc.ca/

**[34]** F. Meskine, M. Chikr El Mezouar, and N. Taleb, "Nonsubsampled countourlet transform combined with genetic algorithms for registration of satellite imaging", In Proceedings of the 2009 IEEE International Conference on Signals, Circuits and Systems, Djerba, Tunisia, Nov. 2009.

**[35]** FH Wong, R Orth, Registration of SEASAT/LANDSAT composite images to UTM coordinates. Proceedings of the Sixth Canadian Syinposium on Remote Sensing, 161–164 (1980)

**[36]** Y. Bentoutou, N. Taleb, M. Chikr el mezouar, M.Taleb, L. Jetto, ''An invariant approach for image registration in digital subtraction angiography'', Pattern Recognition, Vol. 35 n°12, pp. 2853-2865, Dec. 2002.

**[37]** B Zitova, J Flusser, Image registration methods: A survey. Image and Vision Computing. 21, 977–1000 (2003). doi:10.1016/S0262-8856(03)00137-9

**[38]** Y. Bentoutou, N. Taleb, K. Kpalma, J. Ronsin, ''An automatic image registration for applications in remote sensing'', IEEE Transactions on Geoscience and Remote Sensing, Vol. 43 n°9, pp. 2127-2137, 2005.

**[39]** G. Hong and Y. Zhang, "The image registration technique for high resolution remote sensing image in hilly area", IEEE/ISPRS 3rd International Symposium Remote Sensing and Data Fusion Over Urban Areas (URBAN 2005), Tempe/Arizona/USA, March 14-16, 2005.

**[40]** Y Yang, X Gao, Remote sensing image registration via active contour model. Int J Electron Commun. 63, 227–234 (2009). doi:10.1016/j.aeue.2008.01.003

**[41]** F. Meskine, M. Chikr El Mezouar, and N. Taleb, "A Rigid Image Registration Based on the Nonsubsampled Contourlet Transform and Genetic Algorithms", Sensors 2010, 10, 8553-8571.

**[42]** RC Gonzalez, RE Woods, Digital image processing, 3rd edn. (Prentice Hall, 2008)

**[43]** Li, J. and Heap, A.D., 2008. A Review of Spatial Interpolation Methods for Environmental Scientists. Geoscience Australia, Record 2008/23, 137 pp.

**[44]** S Takehana, M Kashimura, S Ozawa, Predictive interpolation of remote sensing images using vector quantization. Communications, Computers and Signal Processing, 1993, IEEE Pacific Rim Conference on. 1, 51–54 (1993)

**[45]** KK Teoh, H Ibrahim, SK Bejo, Investigation on several basic interpolation methods for the use in remote sensing application, in Proceedings of the 2008 IEEE Conference on Innovative Technologies (2008)

**[46]** M. Chikr El Mezouar, N. Taleb, K. Kpalma, and J. Ronsin, "A New Evaluation Protocol for Image Pan-sharpening Methods", In Proceedings of the the 1st International Conference on Computing and Information Technology (ICCIT 2012) Al-Madinah Al-Munawwarah, Saudi Arabia, 12-14 March 2012.

**[47]** JA Richards, X Jia, Remote Sensing Digital Image Analysis: An Introduction, 4th edn. (Secaucus, NJ, USA: Springer-Verlag New York, Inc, 2005)

**[48]** W Dou, Y Chen, An improved IHS image fusion method with high spectral fidelity. The Int Archiv of the Photogramm, Rem Sensing and Spat Inform Sciences. XXXVII, 1253–1256 (2008). part.B7

**[49]** Dong J., Dafang Z., Yaohuan H. and Jinying F. (2011). Survey of Multispectral Image Fusion Techniques in Remote Sensing Applications, Image Fusion and Its Applications, Yufeng Zheng, Alcorn State University, USA (Ed.), ISBN: 978-953-307-182-4, InTech, Available from: http://www.intechopen.com/books/image-fusion-and-its-applications/survey-of-multispectral-image-fusion-techniques-in-remote-sensing-applications

**[50]** C Pohl, JLV Genderen, Multi-sensor image fusion in remote sensing: Concepts, methods, and applications. Int J Remote Sens. 19(5), 823–854 (1998). doi:10.1080/014311698215748

**[51]** R Welch, M Ehlers, Merging multiresolution SPOT HRV and landsat TM data. Photogramm Eng Remote Sens. 53(3), 301–303 (1987)

**[52]** PS Chavez, JA Bowell Jr, Comparison of the spectral information content of Landsat Thematic Mapper and SPOT for three different sites in the Phoenix, Arizona region. Photogramm Eng Remote Sens. 54(12), 1699–1708 (1988)

**[53]** B Garguet-Duport, J Girel, JM Chassery, G Pautou, The use of multiresolution analysis and wavelets transform for merging SPOT panchromatic and multispectral image data. Photogramm Eng Remote Sens. 62(9), 1057–1066 (1996)

**[54]** J Zhou, DL Civco, JA Silander, A wavelet transform method to merge Landsat TM and SPOT panchromatic data. Int J Remote Sens. 19(4), 743–757 (1998). doi:10.1080/014311698215973

**[55]** T Ranchin, L Wald, Fusion of high spatial and spectral resolution images: The ARSIS concept and its implementation. Photogramm Eng Remote Sens. 66, 49–61 (2000)

**[56]** DA Yocky, Image merging and data fusion by means of the discrete twodimensional wavelet transform. Optical Society of America. 12(9), 1834–1841 (September 1995). doi:10.1364/JOSAA.12.001834

**[57]** B Aiazzi, L Alparone, S Baronti, A Garzelli, Context-driven fusion of high spatial and spectral resolution images based on oversampled multiresolution analysis. IEEE Trans Geosc Remote Sens. 40(10), 2300–2312 (2002). doi:10.1109/TGRS.2002.803623

**[58]** A Garzelli, F Nencini, Interband structure modeling for pan-sharpening of very high-resolution multispectral images. Information Fusion 6, 213–224 (2005). doi:10.1016/j.inffus.2004.06.008

**[59]** J Nuñez, X Otazu, O Fors, A Prades, V Pala, R Arbiol, Multiresolution-based image fusion with additive wavelet decomposition. IEEE Trans Geosci Remote Sens. 37(3), 1204–1211 (1999). doi:10.1109/36.763274

**[60]** Y Chibani, A Houacine, The joint use of IHS transform and redundant wavelet decomposition for fusing multispectral and panchromatic image. Int J Remote Sensing 23(18), 3821–3833 (2002). doi:10.1080/ 01431160110107626

**[61]** AL da Cunha, J Zhou, MN Do, The nonsubsampled contourlet transform: Theory, design, and applications. IEEE Trans. Image Process. 15(10), 3089–3101 (2006)

**[62]** M Gonzalo, C Lillo-Saavedra, Multispectral images fusion by a joint multidirectional and multiresolution representation. Int J Remote Sens. 28(18), 4065–4079 (2007). doi:10.1080/01431160601105884

**[63]** I Amro, J Mateos, Multispectral image pansharpening based on the contourlet transform, in Journal of Physics Conference Series. 206(1), 1–3 (2010)

**[64]** S. Stubberud, P. Shea and D. Klamer, " Data Fusion: A Conceptual Approach to Level 2 Fusion (Situational Assessment)", Signal Processing, Sensor Fusion, and Target Recognition XII, Ivan Kadar, Editor, Proceedings of SPIE Vol. 5096 (2003)

**[65]** Bretschneider T., Kao O., Image fusion in remote sensing, Proceedings of the 1st Online Symposium of Electronic Engineers.

**[66]** T Ranchin, B Aiazzi, L Alparone, S Baronti, L Wald, Image fusion: The ARSIS concept and some successful implementation schemes. ISPRS Journal of Photogrammetry & Remote Sensing 58, 4–18 (2003). doi:10.1016/S0924-2716(03)00013-3

**[67]** TM Tu, SC Su, HC Shyu, PS Huang, A new look at IHS-like image fusion methods. Inf Fusion 2(3), 177–186 (2001). doi:10.1016/S1566-2535(01)00036-7

**[68]** Z Wang, D Ziou, C Armenakis, D Li, Q Li, A comparative analysis of image fusion methods. IEEE Trans Geosci Remote Sens. 43(6), 1391–1402 (2005)

**[69]** B Aiazzi, S Baronti, F Lotti, M Selva, A comparison between global and context-adaptive pansharpening of multispectral images. IEEE Geoscience and Remote Sensing Letters 6(2), 302–306 (2009)

**[70]** W Dou, Y Chen, X Li, DZ Sui, A general framework for component substitution image fusion: An implementation using the fast image fusion method. Computers & Geosciences 33, 219–228 (2007). doi:10.1016/j. cageo.2006.06.008

**[71]** A. Garzelli, F. Nencini, L. Alparone, B. Aiazzi, and S. Baronti, "Pansharpening of multispectral image: A critical review and comparison," in Proc. IGARSS, 2004, vol. 1, pp. 81–84.

**[72]** TM Tu, PS Huang, CL Hung, CP Chang, A fast intensity-hue-saturation fusion technique with spectral adjustment for IKONOS imagery. IEEE Geoscience And Remote Sensing Letters. 1(4), 309–312 (2004). doi:10.1109/ LGRS.2004.834804

**[73]** C Thomas, T Ranchin, L Wald, J Chanussot, Synthesis of multispectral images to high spatial resolution: A critical review of fusion methods based on remote sensing physics. IEEE Trans Geosci Remote Sens. 46, 1301–1312 (2008)

**[74]** L Alparone, B Aiazzi, SBA Garzelli, F Nencini, A critical review of fusion methods for true colour display of very high resolution images of urban areas. 1st EARSeL Workshop of the SIG Urban Remote Sensing, Humboldt-Universität zu Berlin (2006)

**[75]** B Aiazzi, S Baronti, M Selva, L Alparone, Enhanced Gram-Schmidt spectral sharpening based on multivariate regression of MS and pan data. IEEE International Conference on Geoscience and Remote Sensing Symposium, IGARSS 2006, 3806–3809 (2006)

**[76]** B. Aiazzi, S. Baronti, and M. Selva, "Improving component substitution pan-sharpening through multivariate regression of MS +Pan Data," IEEE Trans. Geosci. Remote Sens., vol. 45, pp. 3230 – 3239, Oct. 2007.

**[77]** VP Shah, NH Younan, RL King, An efficient pan-sharpening method via a combined adaptive PCA approach and contourlets. IEEE Trans Geosc Remote Sens. 46(5), 1323–1335 (2008)

**[78]** T. -M. Tu, H. -T. Lu, Y. -C. Chang, J. -C. Chang, and C. -P. Chang, "A New Vegetation Enhancement/Extraction Technique for IKONOS and QuickBird Imagery," IEEE Geosci. Remote Sens. Lett., vol. 6, pp. 349 – 353, Apr. 2009. (31)

**[79]** S Rahmani, M Strait, D Merkurjev, M Moeller, T Wittman, An adaptive IHS pan-sharpening method. IEEE Geoscience And Remote Sensing Letters 7(3), 746–750 (2010)

**[80]** J.R. Harris, R. Murray, and T. Hirose (1990). "IHS transform for the integration of radar imagery with other remotely sensed data." Photogrammetric Engineering and Remote Sensing, Vol. 56, No. 12, pp. 1631-1641.

**[81]** R Haydn, GW Dalke, J Henkel, Application of the IHS color transform to the processing of multisensor data and image enhancement. lnternational Symposium on Remote Sensing of Arid and Semi-Arid Lands, 599–616 (1982)

**[82]** F. A. Al-Wassai, N.V. Kalyankar, A. A. Al-Zuky "The IHS Transformations Based Image Fusion", Journal of Global Research in Computer Science, Vol. 2, No. 5, May 2011, pp. 70-77.

**[83]** P Chavez, S Sides, J Anderson, Comparison of three different methods to merge multiresolution and multispectral data: Landsat TM and SPOT panchromatic. Photogramm Eng Remote Sens. 57(3), 295–303 (1991)

**[84]** *Dennis N. Grasso* "Applications of the IHS Color Transformation for 1:24,000-Scale Geologic Mapping: A Low Cost SPOT Alternative", Photogrammetric Engineering and Remote Sensing, 59 (1), pp. 73–83, 1993.

**[85]** M. Chikr El-Mezouar, N. Taleb, K. Kpalma, and J. Ronsin, "A new Intensity-Hue-Saturation fusion technique imagery with color distortion reduction for IKONOS," ICGST Int. GVIP J., Vol. 09, no. 4, pp. 53-60, Dec. 2009. (24)

**[86]** J. A. Malpica, "Hue adjustment to IHS pan-sharpened IKONOS imagery for vegetation enhancement," IEEE Geosci. Remote Sens. Lett., vol. 4, pp. 27 – 31, Jan. 2007.

**[87]** PS Chavez, AY Kwarteng, Extracting spectral contrast in Landsat thematic mapper image data using selective principal component analysis. Photogramm Eng Remote Sens. 55(3), 339–348 (1989)

**[88]** S. Teggi, R. Cecchi, F. Serafini, "TM and IRS-1C-PAN data fusion using multiresolution decomposition methods based on the à trous algorithm", International Journal of Remote Sensing, vol. 24, no. 6, pp. 1287–1301, 2003

**[89]** M González-Audícana, J Saleta, R García Catalán, R García, Fusion of multispectral and panchromatic images using improved IHS and PCA mergers based on wavelet decomposition. IEEE Trans Geosc Remote Sens. 42(6), 1291–1298 (2004)

**[90]** K. A. Kalpoma, and J. –i. Kudoh, "Image fusion processing for IKONOS 1-m color imagery," IEEE Trans. Geosci. Remote Sens., vol. 45, pp. 3075 – 3086, Oct. 2007. (25)

**[91]** AR Gillespie, AB Kahle, RE Walker, Color enhancement of highly correlated images. II. Channel Ratio and "Chromaticity" Transformation Techniques. Remote Sensing Of Environment. 22, 343–365 (1987). doi:10.1016/0034-4257 (87)90088-5

**[92]** V Vijayaraj, CG O'Hara, NH Younan, Quality analysis of pansharpened images. Proc IEEE Int Geosc Remote Sens Symp IGARSS '04. 1, 20–24 (2004)

**[93]** G Cliche, F Bonn, P Teillet, Integration of the SPOT panchromatic channel into its multispectral mode for image sharpness enhancement. Photogrammetric Engineering & Remote Sensing 51(3), 311–316 (1985)

**[94]** WJ Carper, TM Lillesand, RW Kiefer, The use of Intensity-Hue-Saturation transform for merging SPOT panchromatic and multispectral image data. Photogramm Eng Remote Sens. 56(4), 459–467 (1990)

**[95]** JG Liu, Smoothing filter-based intensity modulation: A spectral preserve image fusion technique for improving spatial details. Int J Remote Sensing. 21, 3461–3472 (2000). doi:10.1080/014311600750037499

**[96]** L Alparone, L Facheris, S Baronti, A Garzelli, F Nencini, Fusion of multispectral and SAR images by intensity modulation, in Proceedings of the 7th International Conference on Information Fusion, pp. 637–643 (2004)

**[97]** C Ballester, V Caselles, L Igual, J Verdera, A variational model for P+XS image fusion. International Journal of Computer Vision 69, 43–58 (2006). doi:10.1007/s11263-006-6852-x

**[98]** RA Schowengerdt, Reconstruction of multispatial, multispectral image data using spatial frequency contents. Photogrammetric Engineering & Remote Sensing 46(10), 1325–1334 (1980)

**[99]** PS Chavez Jr, Digital merging of Landsat TM and digitized NHAP data for 1:24,000 scale image mapping. Photogramm Eng Remote Sens. 52(10), 1637–1646 (1986)

**[100]** VJD Tsai, Frequency-based fusion of multiresolution images, in 2003 IEEE International Geoscience and Remote Sensing Symposium IGARSS 2003. 6, 3665–3667 (2003)

**[101]** MM Khan, L Alparone, J Chanussot, Pansharpening quality assessment using the modulation transfer functions of instruments. IEEE Trans Geosc Remote Sens. 47(11), 3880–3891 (2009)

**[102]** L Wald, T Ranchin, M Mangolini, Fusion of satellite images of different spatial resolutions: Assessing the quality of resulting images. Photogramm Eng Remote Sens. 63, 691–699 (1997)

**[103]** JC Price, Combining panchromatic and multispectral imagery from dual resolution satellite instruments. Remote Sensing Of Environment 21, 119–128 (1987). doi:10.1016/0034-4257(87)90049-6

**[104]** JC Price, Combining multispectral data of differing spatial resolution. IEEE Trans Geosc Remote Sens. 37(3), 1199–1203 (May 1999). doi:10.1109/ 36.763272

**[105]** J Park, M Kang, Spatially adaptive multi-resolution multispectral image fusion. Int J Remote Sensing 25(23), 5491–5508 (2004). doi:10.1080/ 01431160412331270830

**[106]** NDA Mascarenhas, GJF Banon, ALB Candeias, Multispectral image data fusion under a Bayesian approach. Int J Remote Sensing 17, 1457–1471 (1996). doi:10.1080/01431169608948717

**[107]** O Punska, Bayesian approaches to multi-sensor data fusion, (Master's thesis, University of Cambridge, 1999)

**[108]** D Fasbender, J Radoux, P Bogaert, Bayesian data fusion for adaptable image pansharpening. IEEE Transactions On Geoscience And Remote Sensing 46, 1847–1857 (2008)

**[109]** RC Hardie, MT Eismann, GL Wilson, MAP estimation for hyperspectral image resolution enhancement using an auxiliary sensor. IEEE Trans Image Process. 13(9), 1174–1184 (2004). doi:10.1109/TIP.2004.829779

**[110]** R Molina, M Vega, J Mateos, AK Katsaggelos, Variational posterior distribution approximation in Bayesian super resolution reconstruction of multispectral images. Applied And Computational Harmonic Analysis 12, 1–27 (2007)

**[111]** M Vega, J Mateos, R Molina, A Katsaggelos, Super-resolution of multispectral images. The Computer Journal 1, 1–15 (2008)

**[112]** M Mateos, J Vega, R Molina, A Katsaggelos, Super resolution of multispectral images using TV image models, in 2th Int Conf on Knowledge-Based and Intelligent Information & Eng Sys, pp. 408–415 (2008)

**[113]** HG Kitaw, Image pan-sharpening with Markov random field and simulated annealing. PhD dissertation, International Institute for Geo-information Science and Earth Observation, NL (2007)

**[114]** MT Eismann, RC Hardie, Application of the stochastic mixing model to hyperspectral resolution enhancement. IEEE Transactions On Geoscience And Remote Sensing. 42(9), 1924–1933 (2004)

**[115]** MT Eismann, RC Hardie, Hyperspectral resolution enhancement using highresolution multispectral imagery with arbitrary response functions. IEEE Transactions On Geoscience And Remote Sensing 43(3), 455–465 (2005)

**[116]** GZ Rong, W Bin, ZL Ming, Remote sensing image fusion based on Bayesian linear estimation. Science in China Series F: Information Sciences. 50(2), 227–240 (2007). doi:10.1007/s11432-007-0008-7

**[117]** W Niu, J Zhu, W Gu, J Chu, Four statistical approaches for multisensor data fusion under non-Gaussian noise, in IITA International Conference on Control, Automation and Systems Engineering (2009)

**[118]** L Brandenburg, H Meadows, Shaping filter representation of nonstationary colored noise. IEEE Transactions on Information Theory 17, 26–31 (1971). doi:10.1109/TIT.1971.1054585

**[119]** PJ Burt, EH Adelson, The Laplacian pyramid as a compact image code. IEEE Transactions On Communications. COM-3l(4), 532–540 (1983)

**[120]** SG Mallat, A theory for multiresolution signal decomposition: The wavelet representation. IEEE Transactions On Pattern Analysis And Machine Intelligence 11(7), 674–693 (1989). doi:10.1109/34.192463

**[121]** J.L. Starck, E.J. Candès, D.L. Donoho, The curvelet transform for image denoising, IEEE Transactions on Image Processing 11 (6) (2002) 670–684.

**[122]** M.N. Do, M. Vetterli, The finite ridgelet transform for image representation, IEEE Transactions on Image Processing 12 (1) (2003) 16–28.

**[123]** J Zhang, Multi-source remote sensing data fusion: Status and trends. International Journal of Image and Data Fusion 1(1), 5–24 (2010). doi:10.1080/19479830903561035

**[124]** L Alparone, S Baronti, A Garzelli, Assessment of image fusion algorithms based on noncritically-decimated pyramids and wavelets, in Proc IEEE 2001 International Geoscience and Remote Sensing Symposium IGARSS '01. 2, 852–854 (2001)

**[125]** MG Kim, I Dinstein, L Shaw, A prototype filter design approach to pyramid generation. IEEE Trans on Pattern Anal and Machine Intell. 15(12), 1233–1240 (1993). doi:10.1109/34.250842

**[126]** B Aiazzi, L Alparone, S Baronti, A Garzelli, Spectral information extraction by means of MS+PAN fusion. Proceedings of ESA-EUSC 2004 - Theory and Applications of Knowledge-Driven Image Information Mining with Focus on Earth Observation, 20.1 (2004)

**[127]** D.A. Yocky, Multiresolution wavelet decomposition image merger of Landsat Thematic Mapper and SPOT panchromatic data. Photogrammetric Engineering and Remote Sensing, Vol. 62, No. 9, pp. 1067-1074 (1996).

**[128]** M González-Audícana, X Otazu, Comparison between Mallat's and the a'trous discrete wavelet transform based algorithms for the fusion of multispectral and panchromatic images. Int J Remote Sens. 26(3), 595–614 (2005). doi:10.1080/01431160512331314056

**[129]** K. Amolins, Y. Zhang, P. Dare, Wavelet based image fusion techniques-An introduction, review and comparison, ISPRS Journal of Photogrammetry & Remote Sensing 62 (2007) pp. 249-263 (12)

**[130]** L. Wald, "Quality of high resolution synthesized images: Is there a simple criterion?" in Proc. Int. Conf. Fusion of Earth Data, Jan. 2000, pp. 99 – 105. (43)

**[131]** Y. Zhang, G. Hong, An IHS and wavelet integrated approach to improve pan-sharpening visual quality of natural colour IKONOS and QuickBird images, Information Fusion Vol. 6, 2005, pp 225-234 (21)

**[132]** M. Choi, R. Y. Kim, and M. G. Kim, "The curvelet transform for image fusion," International Society for Photogrammetry and Remote Sensing, ISPRS 2004, Vol. 35, Part B8, 59-64, Istanbul, 2004.

**[133]** L. Alparone, S. Baronti, A. Garzelli, F. Nencini, The curvelet transform for fusion of very-high resolution multi-spectral and panchromatic images, in: Proceedings of the 25th EARSeL Symposium, Porto, Portugal, Millpress Science Publishers, The Netherlands, 2006.

**[134]** A. Garzelli, F. Nencini, L. Alparone, S. Baronti, Multiresolution Fusion of Multispectral and Panchromatic Images through the Curvelet Transform, Geoscience and Remote Sensing Symposium, IGARSS apos;05. Proceedings. 2005 IEEE International Volume 4, Issue, 25-29 July 2005 Page(s): 2838 – 2841 (14)

**[135]** M. N. Do and M. Vetterli, "The Contourlet Transform: An Efficient Directional Multiresolution Image Representation", IEEE Transactions On Image Processing, vol. 14, no. 12, pp. 2091-2106, Dec. 2005.

**[136]** AM ALEjaily, IAE Rube, MA Mangoud, Fusion of remote sensing images using contourlet transform. Springer Science, 213–218 (2008)

**[137]** Y. Choi, S. Latifi, Contourlet Based Multi-Sensor Image Fusion, in Proceedings of the 2012 International Conference on Information and Knowledge Engineering IKE'12, Las Vegas, Nevada, USA july 16-19 2012.

**[138]** Q. Miao and B.Wang, "The contourlet transform for image fusion," Proc. SPIE, vol. 4, p. 624 20Z.1, 2006.

**[139]** Y. Zheng, C. Zhu, J. Song, and X. Zhao, "Fusion of multi-band SAR images based on contourlet transform," in Proc. IEEE Int. Conf. Inf. Acquisition, 2006, pp. 420–424.

**[140]** Q. Miao and B.Wang "A Novel Image Fusion Method Using Contourlet Transform", International conference on communications, circuits, and systems, Guilin, pp: 548-552, June 2006.

**[141]** H. Chu, C. Survey Inst., C. De-gui Teng ; M.-q. Wang, Fusion of remotely sensed images based on subsampled contourlet transform and spectral response, in Proceedings of Urban Remote Sensing Event, 2009 Joint 20-22 May 2009, Shanghai.

**[142]** M Song, X Chen, P Guo, A fusion method for multispectral and panchromatic images based on HSI and contourlet transformation, in Proc 10th Workshop on Image Analysis for Multimedia Interactive Services WIAMIS '09, pp. 77–80 (2009)

**[143]** I Amro, J Mateos, M Vega, General contourlet pansharpening method using Bayesian inference, in 2010 European Signal Processing Conference (EUSIPCO-2010), pp. 294–298 (2010)

**[144]** X Otazu, M González-Audícana, O Fors, J Núñez, Introduction of sensor spectral response into image fusion methods: Application to wavelet-based methods. IEEE Trans Geosci Remote Sens. 43(10), 2376–2385 (2005)

**[145]** M. Choi, A New Intensity-Hue-Saturation Fusion Approach to Image Fusion With a Tradeoff Parameter, IEEE transactions on geosciences and remote sensing, VOL. 44, No. 6, JUNE 2006 (13)

**[146]** L. Alparone, L. Wald, J. Chanussot, C. Thomas, P. Gamba, and L. M. Bruce, "Comparison of pan-sharpening algorithms: outcome of the 2006 GRS-S data-fusion contest," IEEE Trans. Geosci. Remote Sens., vol. 45, pp. 3012 – 3021, Oct. 2007. (39)

**[147]** Y Jinghui, Z Jixian, L Haitao, S Yushan, P Pengxian, Pixel level fusion methods for remote sensing images: A current review in ISPRS TC VII Symposium 100 Years ISPRS, ed. by W Wagner, B Szkelys, 680–686 (2010)

**[148]** Z Wang, AC Bovik, HR Sheikh, EP Simoncelli, Image quality assessment: From error visibility to structural similarity. IEEE Trans Image Process. 13, 600–612 (2004). doi:10.1109/TIP.2003.819861

**[149]** Q Du, NH Younan, R King, VP Shah, On the performance evaluation of pansharpening techniques. IEEE Trans Geosc Remote Sens L. 4(4), 518–522 (2007)

**[150]** V Vijayaraj, NH Younan, CG O'Hara, Quantitative analysis of pansharpened images. Optical Engineering 45(4), 046202 (2006). doi:10.1117/1.2195987

**[151]** C. Thomas and L. Wald 2005. Assessment of the quality of fused products. In Proceedings of the 24th EARSeL Symposium "New Strategies for European Remote Sensing", 25-27 May 2004, Dubrovnik, Croatia

**[152]** F. Samadzadegan and F. DadrasJavan, "Evaluating the potential of image quality metrics for quality assessment of high resolution pan-sharpen satellite imagery in urban area", Volume XXXVIII - Part 1, ISPRS Commission I Mid-Term Symposium 'Image Data Acquisition - Sensors & Platforms', June 15-18, 2010 Calgary, Alberta, Canada

**[153]** Y. Zhang, "Methods for image fusion quality assessment-a review, comparison and analysis", the international archives of photogrammety, remote sensing and spatial information sciences, Vol XXXVII, Part B7. Beijing 2008, pp. 1101-1109.

**[154]** V Meenakshisundaram, Quality assessment of IKONOS and Quickbird fused images for urban mapping, (Master's thesis, University of Calgary, 2005)

**[155]** L Alparone, B Aiazzi, S Baronti, A Garzelli, F Nencini, M Selva, Multispectral and panchromatic data fusion assessment without reference. Photogrammetric Engineering & Remote Sensing 74, 193–200 (2008)

**[156]** Z. Wang and A. C. Bovik, A Universal Image Quality Index, IEEE Signal Processing Letters, Vol. 9, No. 3, 2002, pp. 81-84 (20)

**[157]** L Alparone, B Aiazzi, S Baronti, A Garzelli, F Nencini, A new method for MS + Pan image fusion assessment without reference, in Proc IEEE Int Conf Geoscience and Remote Sensing Symp IGARSS 2006, pp. 3802–3805 (2006)

**[158]** L. Alparone, S. Baronti, A. Garzelli, and F. Nencini, "A global quality measurement of pan-sharpened multispectral imagery," IEEE Trans. Geosci. Remote Sens., vol. 1, pp. 313 – 317, Oct. 2004.

**[159]** R. H. Yuhas, A. F. H. Goetz, and J.W. Boardman, "Discrimination among semi-arid landscape endmembers using the spectral angle mapper (SAM) algorithm," in Proc. Summaries 3rd Annu. JPL Airborne Geosci. Workshop, 1992, pp. 147 – 149. (41)

**[160]** F. Nencini, A. Garzelli, S. Baronti, L. Alparone, Remote sensing image fusion using the curvelet transform, Information Fusion Vol. 8, 2007, pp 143-156 (15)

**[161]** V Vijayaraj, A quantitative analysis of pansharpened images. Master's thesis, Mississippi State Univ (2004)

**[162]** Y. Zheng, E. A. Essock, B. C. Hansen, and A. M. Haun, "A new metric based on extended spatial frequency and its application to DWT based fusion algorithms," Inf. Fusion, vol. 8, pp. 177 – 192, Apr. 2007. (42)

**[163]** C. Thomas and L. Wald, "Comparing distances for quality assessment of fused products," in Proc. 26th EARSeL Annu. Symp. New Develop. Challenges Remote Sens., Warsaw, Poland, May 29–31, 2006. Z. Bochenek, Ed., Rotterdam, The Netherlands: Balkema, 2007, pp. 101 – 111.

**[164]** PS Pradhan, RL King, NH Younan, DW Holcomb, Estimation of the number of decomposition levels for a wavelet-based multiresolution multisensor image fusion. IEEE Trans Geosc Remote Sens. 44(12), 3674–3686 (2006)

**[165]** M Lillo-Saavedra, C Gonzalo, A Arquero, E Martinez, Fusion of multispectral and panchromatic satellite sensor imagery based on tailored filtering in the fourier domain. Int J Remote Sens. 26, 1263–1268 (2005). doi:10.1080/01431160412331330239

**[166]** J. Lee, and C. Lee, "A fast and efficient panchromatic sharpening," IEEE Trans. Geosci. Remote Sens., vol. 48, pp. 155 – 163, Jan. 2010.

**[167]** Y. Zhang, "A new automatic approach for effectively fusing Landsat 7 as well as IKONOS images," in Proc. IEEE/IGARSS, Toronto, ON, Canada, Jun. 2002, pp. 2429 – 2431. (32)

**[168]** H. Chu, and W. Zhu, "Fusion of IKONOS satellite imagery using IHS transform and local variation" IEEE Geosci. Remote Sens. Lett., vol. 5, pp. 653 – 657, Oct. 2008. (33)

**[169]** M. Chikr El Mezouar, N. Taleb, K. Kpalma, and J. Ronsin, "Edge Preservation in Ikonos Multispectral and Panchromatic Imagery Pan-sharpening", In Proceedings of the the 1st International Conference on Computing and Information Technology (ICCIT 2012) Al-Madinah Al-Munawwarah, Saudi Arabia, 12-14 March 2012.

**[170]** A. Giachetti and N. Asuni, "Fast artifacts-free image interpolation," in Proc. of the British Machine Vision Conf, Sept. 2008, pages 123--132. (4)

**[171]** M. Chikr El-Mezouar, N. Taleb, K. Kpalma, and J. Ronsin, "An IHS-Based Fusion for Color Distortion Reduction and Vegetation Enhancement in IKONOS Imagery," IEEE Trans. Geosci. Remote Sens., vol. 49, pp. 1590 – 1602, May 2011.(1)

**[172]** M. Chikr El-Mezouar, N. Taleb, K. Kpalma and J. Ronsin, "Vegetation extraction from IKONOS imagery using high spatial resolution index", J. Appl. Remote Sens. 5, 053543 (Aug 11, 2011)

**[173]** M. Chikr El Mezouar, N. Taleb, K. Kpalma, and J. Ronsin, "An improved Intensity-Hue-Saturation for a high-resolution image fusion technique minimizing color distortion", International Journal of Information and Communication Technology (IJICT), Vol. 4, No. 3-4, pp. 95-101 2011 / ISSN: 0973-5836 / Serials Publications, India.

**[174]** Y. Zhang, "Problems in the fusion of commercial high-resolution satelitte images as well as landsat 7 images and initial solutions," IAPRS, vol. 34, Part 4 "GeoSpatial Theory, Processing and Applications", Ottawa, July 2002. (11)

**[175]** Z. Teague, "Ikonos pan-sharpened products evaluation," in Proc. High Spatial Resolution Commercial Imagery Workshop, Mar. 20, 2001. [Online]. Available: http://ldcm.gsfc.nasa.gov/library/HSRCIW01/PanSharp_Products Eval _ Teague.pdf . (35)

**[176]** Y. Xie, Z. Sha, and M. Yu, "Remote sensing imagery in vegetation mapping: A review," J. Plant Ecology, vol. 1, no. 1, pp. 9 – 23, Mar. 2008. (36)

**[177]** T.-M. Tu, W.-C. Cheng, C.-P. Chang, P. S. Huang, and J.-C. Chang, "Best tradeoff for high-resolution image fusion to preserve spatial details and minimize color distortion," IEEE Geosci. Remote Sens. Lett., vol. 4, pp. 302 – 306, Apr. 2007. (34)

**[178]** A. Huete, C. Justice, and W. van Leeuwen (1999, Apr. 30), MODIS vegetation index (MOD 13): algorithm theoretical basis document. (3rd ed.) [Online]. Available: http://modis.gsfc.nasa.gov/data/atbd/land_atbd.php

**[179]** J. Rogan, and D.M. Chen, "Remote sensing technology for mapping and monitoring land-cover and land-use change," Progress in Planning 61, 301-325 (2004). (45)

**[180]** J. Nichol, and C. M. Lee, "Urban vegetation monitoring in Hong Kong using high resolution multispectral images," International Journal of Remote Sensing 26, 903-918 (2005). (46)

**[181]** A. Verheyden, F. Dahdouh-Guebas, K. Thomas, W. De Genst, S. Hettiarachchi and N. Koedam, "High-resolution vegetation data for mangrove research as obtained from aerial photography," Environment, Development and Sustainability 4, 113-133 (2002). (47)

**[182]** J. Hu, W. Chen, X. Li, and X. He, "Roof confusion removal for accurate vegetation extraction in the urban environment" International Workshop on Earth Observation and Remote Sensing Applications EORSA, 1-7, IEEE, Beijing China, (2008). (48)

**[183]** S. J. Goetz, R. K. Wright, A. J. Smith, E Zinecker, and E. Schaub, "IKONOS imagery for resource management: Tree cover, impervious surfaces, and riparian buffer analyses in the mid-Atlantic region," Remote Sensing of Environment 88, 195-208 (2003). (50)

**[184]** J. A. Greenberg, S. Z. Dobrowski, C. M. Ramirez, J. L. Tuil, and S. L. Ustin, "A Bottom-up Approach to Vegetation Mapping of the Lake Tahoe Basin Using Hyperspatial Image Analysis," Photogrammetric Engineering & Remote Sensing 72, 581-589 (2006). (51)

**[185]** W. C. Cheng, J.C. Chang, C. P. Chang, Y. Su, and T. M. Tu, "A Fixed-Threshold Approach to Generate High-Resolution Vegetation Maps for IKONOS Imagery," Sensors 8, 4308-4317 (2008).

**[186]** J. H. Horne, "A tasseled cap transformation for IKONOS-2 images," in ASPRS 2003 Annual Conference Proceedings, pp. 60–70, Anchorage, Alaska (2003). (53)

**[187]** C Thomas, L Wald, A MTF-based distance for the assessment of geometrical quality of fused products, in 2006 9th International Conference on Information Fusion, pp. 1–7 (2006)

**[188]** C. Padwick, M. Deskevich, F. Pacifici, and S. Smallwood, "WorldView-2 Pan-Sharpening," presented at ASPRS 2010 Annual Conf., San Diego, CA, Apr. 26-30, 2010. (59)

**[189]** T-M. Tu, Y-H. Lee, C-P. Chang, and P. S. Huang, "Adjustable intensity-hue-saturation and Brovey transformation fusion technique for IKONOS/QuickBird imagery," Optical Engineering, vol. 44 (11), pp. 116201-1–116201-10, 2005.

**[190]** R. Wang and Y. Zhang, "Extraction of urban road network using Quickbird Pansharped Multispectral and Panchromatic Imagery by Performing Edge-Aided Post-Classification" . ISPRS Joint Workshop on Spatial Temporal and Multi-Dimensional Data Modeling and Analysis, October, 2-3, 2003, Quebec, Canada.(2)

**[191]** Y. Luo, Y. Xue and S. Zhong, "Road extraction from IKONOS image using grid computing platform," in Proc. IEEE IGARSS '05, vol. 6, pp. 3895 – 3898, 2005.

**[192]** J.F. Canny, "A computational approach to edge detection," IEEE Trans Pattern Analysis and Machine Intelligence, 8(6): pp. 679-698, Nov 1986. (8)

# List of publications

## Journal Papers


[1] **M. Chikr El Mezouar**, N. Taleb, K. Kpalma, and J. Ronsin, "Vegetation extraction from IKONOS imagery using high spatial resolution index", Journal of applied Remote Sensing, Vol. 5, pp.: 053543-01 053543-14, DOI: 10.1117/1.3624518 (Aug 11, **2011**).

[2] **M. Chikr El Mezouar**, N. Taleb, K. Kpalma, and J. Ronsin, "An IHS-based fusion for color distortion reduction and vegetation enhancement in IKONOS imagery", IEEE Transactions on Geoscience and Remote Sensing, Vol. 49 (5), pp.: 1590 – 1602, DOI: 10.1109/TGRS.2010.2087029 (May **2011**).

[3] **M. Chikr El Mezouar**, N. Taleb, K. Kpalma, and J. Ronsin, "An improved Intensity-Hue-Saturation for a high-resolution image fusion technique minimizing color distortion", International Journal of Information and Communication Technology (IJICT), Vol. 4, No. 3-4, pp. 95-101 **2011** / ISSN: 0973-5836 / Serials Publications, India.

[4] F. Meskine, **M. Chikr El Mezouar**, and N. Taleb, "A rigid image registration based on the nonsubsampled contourlet transform and genetic algorithms", Sensors **2010**, 10, 8553-8571.

[5] **M. Chikr El Mezouar**, N. Taleb, K. Kpalma and J. Ronsin. "A new Intensity-Hue-Saturation fusion technique with color distortion reduction for IKONOS imagery", ICGST International Journal on Graphics, Vision and Image Processing, GVIP journal, Vol. 09, issue VI, pp. 53-60, December **2009**.

## Conference paper

[1] K. Kpalma, C. Bai, **M. Chikr El Mezouar**, K. Belloulata, N. Taleb, L. Belhallouche and D. Boukerroui, "A New Histogram-based Descriptor for Images Retrieval from databases", In Proceedings of the 2nd International Workshop on Next Generation Medical Decision Support Systems 2012 (MedDecSup'2012), 10-11 July 2012, Sofia, Bulgaria.

[2] **M. Chikr El Mezouar**, N. Taleb, K. Kpalma, and J. Ronsin, "A New Evaluation Protocol for Image Pan-sharpening Methods", In Proceedings of the the 1st International Conference on Computing and Information Technology (ICCIT 2012) Al-Madinah Al-Munawwarah, Saudi Arabia, 12-14 March **2012**.

[3] **M. Chikr El Mezouar**, N. Taleb, K. Kpalma, and J. Ronsin, "Edge Preservation in Ikonos Multispectral and Panchromatic Imagery Pan-sharpening", In Proceedings of the the 1st International Conference on Computing and Information Technology (ICCIT 2012) Al-Madinah Al-Munawwarah, Saudi Arabia, 12-14 March **2012**.

[4] A. Horch, N. Taleb, **M. Chikr El-Mezouar**, "NSCT et seuillage adaptatif pour le débrouitage d'image", In Proceedings of the 2nd International Conference ISPA, Biskra, Algeria, Dec. **2010**.

[5] **M. Chikr El Mezouar**, N. Taleb, K. Kpalma, and J. Ronsin, "A high-resolution index for vegetation extraction in IKONOS images", In Proceedings of the SPIE Remote Sensing 2010, Toulouse, France, Sep. **2010**.

[6] F. Meskine, **M. Chikr El Mezouar**, and N. Taleb, "Nonsubsampled countourlet transform combined with genetic algorithms for registration of satellite imaging", In Proceedings of the 2009 IEEE International Conference on Signals, Circuits and Systems, Djerba, Tunisia, Nov. **2009**.

[7] **M. Chikr El Mezouar**, N. Taleb, K. Kpalma and J. Ronsin, "A new Intensity-Hue-Saturation fusion technique with color distortion reduction for IKONOS imagery", In Proceedings of the 5th International Conference Sciences of Electronic, Technologies of Information and Telecommunications, Hammamet, TUNISIA, March, **2009**.

## Other

[1] **M. Chikr El Mezouar**, N. Taleb, K. Kpalma and J. Ronsin. "An efficient NSCT based Pan-sharpening method applied to high resolution images", **selected to be among the 10 best papers** submitted to the 2012 IEEE GRSS Data Fusion Contest, organized by the Data Fusion Technical Committee (DFTC) of the Geoscience and Remote Sensing Society (GRSS) of the International Institute of Electrical and Electronic Engineers (IEEE). The final results are published on the page web:
**http://www.grss-ieee.org/community/technical-committees/data-fusion/data-fusion-contest/**

# List of figures

# List of tables

ملخص

ان الأقمار الصناعية المراقبة للأرض تقدم بيانات متعددة الأطياف وحساسة للألوان ذات مقاسات مختلفة. اندماج صورة (PAN) بانكروماتي وجود ارتفاع قرارات الطيفية المكانية ولكن مع انخفاض متعددة الأطياف (MS) وصور وجود منخفض قرارات الطيفية المكانية ولكنها مرتفعة هي القضية الرئيسية في تطبيقات الاستشعار عن بعد والتي تتطلب الكثير من كلا ارتفاع القرارات المكانية والطيفية عالية. قد تنصهر تقديم صورة تعزيز ميزة، وزيادة دقة تصنيف. وتعرف هذه التقنيات ومعالجة الصور وعموم شحذ أو تقنيات الاندماج القرار.

في هذه الأطروحة يتم اقتراح ثلاثة خوارزميات لاندماج الصور. في فئة استبدال عنصر، والمساهمات الرئيسية لدينا، ويتكون في استخدام IHS وتعزيز منطقة الضوء الأخضر في الأماكن المزروعة. واقترح اثنان الخوارزميات. في الخوارزمية الأولى التي يتم فيها الكشف عن النباتات بإستعمال NDVI ويتم ذلك في زيادة قبل عملية الاندماج. في المقابل، لخوارزمية 2 تتم زيادة بعد عملية الاندماج، ويحدد الغطاء النباتي باستخدام المؤشر الجديد (HRNDVI) المقترحة للصور عالية الدقة. ويستخدم HRNDVI في استخراج النباتات حتى في حالة الحضرية المعقدة، حيث تتوزع على الغطاء النباتي. يتم تضمين الخوارزمية 3 عملية الاندماج في فئة متعددة المقاسات على أساس تحويل NSCT. وأكد للتحسن باستخدام عدد قليل من مستويات التحلل للصور المتعدد وعدد كبير من مستويات التحلل للصورة عموم. هذه الاستراتيجية تسمح للحصول على نتائج مرضية كما و بصريا.

كلمات مفتاحيه: الاستشعار عن بعد، ادماج الصور، كشف الغطاء النباتي.

## Résumé :

Les satellites d'observation de la Terre fournissent des données multispectrales et panchromatiques ayant différentes résolutions spatiales, spectrales, temporelles, et radiométriques. La fusion d'une image panchromatique (PAN) ayant une résolution spatiale élevée, mais une faible résolution spectrale avec une image multispectrales (MS) ayant une faible résolution spatiale, mais une haute résolution spectrale est utile dans de nombreuses applications de la télédétection qui nécessitent à la fois de hautes résolutions spatiale et spectrale. L'image fusionnée peut fournir un rehaussement, et augmenter la précision de classification. Ces techniques de traitement d'image sont connus sous le nom fusion ou pansharpening.

Dans cette thèse trois algorithmes sont proposés pour le pansharpening. Dans la catégorie de substitution de composants, nos principales contributions, consiste à utiliser la transformée IHS et l'amplification de la bande verte dans la zone de végétation. Deux algorithmes sont proposés. Dans le premier algorithme, la végétation est détectée par l'indice NDVI et l'amplification est effectuée avant le processus de fusion. En revanche, pour le second algorithme l'amplification se fait après le processus de fusion et la végétation est délimitée à l'aide d'un nouvel indice (HRNDVI) proposé pour les images haute résolution. L'HRNDVI est utilisé dans l'extraction de la végétation, même dans le cas complexe urbain où la végétation est dispersée. Le troisième algorithme de pansharpening est inclus dans la catégorie multirésolution basée sur la transformée NSCT. L'amélioration est assurée par l'utilisation d'un nombre de niveaux de décomposition pour les images MS inférieur à celui de l'image Pan. Cette stratégie permet d'obtenir des résultats visuels et quantitatifs satisfaisants.

**Mots clés :**
Télédétection satellitaire, fusion, NDVI, NSCT.

## Abstract

Earth observation satellites provide multispectral and panchromatic data having different spatial, spectral, temporal, and radiometric resolutions. The fusion of a panchromatic (PAN) image having high spatial but low spectral resolutions with multispectral (MS) images having low spatial but high spectral resolutions is a key issue in many remote sensing applications that require both high spatial and high spectral resolutions. The fused image may provide feature enhancement, and classification accuracy increase. These image processing techniques are known as pan-sharpening or resolution fusion techniques.

In this thesis three algorithms are proposed for pansharpening. In component substitution category, our main contributions, consists in using IHS and boosting the Green band in the vegetated area. Two algorithms were proposed. In the first algorithm the vegetation is detected by the NDVI and the boosting is done before the fusion process. In contrast, for the second algorithm the boosting is done after the fusion process and the vegetation is delineated using a new index (HRNDVI) proposed for high resolution images. HRNDVI is used in vegetation extraction even in the complex urban case where the vegetation is scattered. The third pansharpening algorithm is included in the multiresolution category based on NSCT transform. The improvement is assured by using a low number of decomposition levels for MS images and a high number of decomposition levels for the Pan image. This strategy allows getting satisfying visual and quantitative results.

**Keywords :**
Remote sensing, Pansharpening, NDVI, NSCT.